ADVANCED STEEL CONSTRUCTION

An International Journal

Volume 8 Number 1

March 2012

CONTENTS

Technical Papers

Cover:
THE COAL STORAGE DOMES AT THE ENEL TORREVALDALIGA NORTH THERMOELECTRIC POWER PLANT, ITALY
Credits:
Photo ©: Alfredo D'Amato - Agenzia 7 Minutes
Structural system: MERO Italiana, Verona
Dome Design: Ing. Gilbert Pirozzi, Mero, Verona
Construction Management and Technical Support: ENEL Energy and Innovation Office,
Ing. Giovanni Belloni, Ing. Marco Ulisse, Ing. Ubaldo Savina, Ing. Sergio Castronuovo.
Scientific Consultant: Prof. Federico M. Mazzolani, University of Naples

ADVANCED STEEL CONSTRUCTION

an International Journal

ISSN 1816-112X

Volume 8 Number 1

March 2012

Editors-in-Chief

S.L. Chan, *The Hong Kong Polytechnic University, Hong Kong*

W.F. Chen, *University of Hawaii at Manoa, USA*

R. Zandonini, *Trento University, Italy*

STUDY ON DYNAMIC DAMAGE CAUSES OF SINGLE LAYER LATTICED SHELLS BASED ON REFINED MEMBER CALCULATION MODEL

Yang Ding [1], Lin Qi [2,*] and Zhongxian Li [3]

[1] *Professor, Department of Civil Engineering, Tianjin University, Tianjin, China*
[2] *Ph. d candidate, Department of Civil Engineering, Tianjin University, Tianjin, China*
[3] *Professor, Department of Civil Engineering, Tianjin University, Tianjin, China*
*(Corresponding author: E-mail: qilin1208@163.com)

ABSTRACT: Based on mechanical characteristics of the members of single layer latticed shells, two buckling types of structural compression members are presented. The pre-buckling and post-buckling mechanical behaviors of the structural member are simulated by different models, and the refined member calculation model is established. In this model the second order effect of the member is considered, and the possible buckle-straighten processes of the members and the form-disappear processes of the plastic hinges of the structure under earthquakes can be simulated. Numerical structure models of commonly used single layer latticed shells are created to analyze the causes of structural dynamic damages under earthquakes. The calculation results indicate that dynamic damage causes of single layer latticed shells vary with different structural types: dynamic damages of single layer spherical latticed shells are caused by buckling members which weaken the structural bearing capacity; dynamic damages of single layer cylindrical latticed shells are caused by concentrative plastic hinges in the end sections of some members which make portions of the structure turn to mechanisms; dynamic damages of single layer elliptic paraboloid latticed shells are caused by combined actions of the two causes mentioned above.

Keywords: Single layer latticed shell, Refined member calculation model, Member buckling, Plastic hinge, Second order effect, Dynamic damage cause

1.   INTRODUCTION

The calculation method for single layer latticed shells is becoming a major research subject recently. Kani and Heidari [1] made an attempt to automatically calculate the bifurcation of the buckling path of shallow latticed domes using two-stage analysis of the space structure without introducing any geometrical imperfections. Yamada et al. [2] studied the effects of geometric imperfections on the nonlinear buckling behavior of rigidly jointed single-layer latticed domes under vertical loading. Hearn and Adams [3] established a method which used static joint equilibrium equations to determine a minimum set of adjustments to latticed geometry needed to achieve equilibrium reference states for shape selection for latticed structures with members that carry axial force only. Morris [4] presented a nonlinear elastic-plastic method for three dimensional beam elements which was applied to investigate the imperfection-sensitivity of latticed domes made up of tubular members. Kani and McConnel [5] made a numerical and experimental study on the collapse and post collapse behavior of shallow latticed domes. Although there are many scholars making investigations of single layer latticed shells, causes of dynamic damages of the structure under earthquakes are rarely carried on. Mechanical characteristics of single layer latticed shells vary with different structure types, so the causes of structural dynamic damages are not the same. The single layer latticed shell is a typical spatial structure composed of a great many members by certain geometrical law. Subject to dynamic loads, the single layer latticed shell undergoes loading-unloading process repeatedly, which leads to the possible buckle-straighten processes of the structural members and the form-disappear processes of the plastic hinges. The mechanical behaviors of the members and the structural bearing capacity are changing continuously. The refined member calculation model which can simulate the continuous mechanical behavior changes of the member should be established, so the accurate damage processes of single layer latticed shells can be modeled.

There are two main problems if members of single layer latticed shells are modeled by general beam element of the general finite element analysis program: (1) The accuracy of the elastic-plastic element stiffness matrixes. By general finite element analysis program, the material constitutive relationships of the Gauss integral sections of the general beam element are used to calculate the element stiffness matrix. The elastic element stiffness matrix can be calculated correctly by this arithmetic if the member stays elastic. It is the end section of the member, which is not the Gauss integral section that firstly turns into plastic state commonly. Thus when the end section turns into plastic state, the element stiffness matrix calculated by general finite element analysis program is still elastic. Because of different loading history, material elastic-plastic constitutive relationships of different sections of the member are not the same, so it is not rational to calculate elastic-plastic element stiffness matrix based on the material constitutive relationship of the Gauss integral sections. (2) The simulation of the buckling members. If one structural member is modeled by a single general beam element of general finite element analysis program, buckling of the members cannot be simulated, and the decrease of the member bearing capacity is caused by material yielding rather than member buckling. In this case the member can bear the load far over the buckling critical load and the member bearing capacity is seriously overestimated. Buckling of the member can be simulated if one member is divided into more than one general beam element of general finite element analysis program. However, the post-buckling behaviors of the member and the plastic hinges forming in the end section and the central section cannot be simulated. How many general beam elements of general finite element analysis program one structural member should be divided into is also difficult to be appropriately determined.

To study the dynamic damage causes of single layer latticed shells under earthquakes, calculation model of the structure that tallies with the actual situation should be created. In this paper, two buckling types of the compression members of single layer latticed shells are presented. The pre-buckling and post-buckling mechanical behaviors of the structural member are simulated by different models, and the refined member calculation model is established. By this model the second order effect of the member is considered, and the possible buckle-straighten processes of the member and the form-disappear processes of the plastic hinge and the consequent complex change processes of structural bearing capacity under earthquakes can be simulated clearly. Based on the refined member calculation model, structural models are created to study the causes of dynamic damages of typical single layer latticed shells under earthquakes.

2.   BUCKLING TYPES OF THE MEMBER

There are two possible buckling types of the compression members of single layer latticed shells: (1) Buckling type I. The plastic hinge forms in the end section of the member, and slenderness ratio of the member gets bigger. This may cause the buckling of the member. The members of single layer latticed shells bear concentrated forces at the nodes only, so it is the end section of the member where the stress is biggest. The buckling critical condition may not be satisfied when the plastic zone forms in the end section of the member. The plastic zone develops along with the increment of the load. When the plastic hinge forms in the end of the member and makes the slenderness ratio turn larger, the buckling critical condition gets easier to be med. Even a small increment of the external load may make the member buckling. The plastic zone or plastic hinge then forms in the central section of the buckled member as a combined action of both the axial compression force and the additional bending moment. (2) Buckling type II. The member bears compression axial force plenty big and the buckling critical condition is met without the plastic hinge forming in the end section. The plastic zone or plastic hinge then forms in the central section of the buckled member as a combined action of both the compression axial force and the additional bending moment.

3.   PLASTIC HINGE IN THE END SECTION OF THE MEMBER

Influences to mechanical behavior of the structural member caused by plastic hinge forming in the end section can be illuminated by the cyclic loading experiment on cantilever member (Fan [6]). Hysteresis loop of the experiment is illustrated in Figure 1, and full-range behavior of the cantilever member subjected to once cycling loading is illustrated in Figure 2. The curve in Figure 2 can be divided into 10 segments: (1) *O-A* is the elastic loading segment; (2) outboard fibers in the end section of the member yield at point *A*, and the total cross end section yields at point *B* when plastic hinge forms; (3) material of the end section of the member enters its strengthening stage in segment *B-C*, and the stress of the end section reaches ultimate strength at point *C*; (4) in segment *C-D* the load that the member can bear decreases a little bit and the deformation becomes larger continuously; (5) *D-E* is the unloading segment, and the plastic hinge in the end section of the member disappears; (6) *E-F* is elastic loading segment; (7) outboard fibers in the end section of the member yields at point *F*, and the total cross end section yields at point *G* when plastic hinge forms once again; (8) material of the end section of the member enters its strengthening stage in segment *G-H*, and the stress of the end section reaches ultimate strength at point *H*; (9) in segment *H-I* the load that the member can bear decreases a little bit and the deformation becomes larger continuously; (10) *I-J* is the unloading segment, and the plastic hinge in the end section of the member disappears. The residual deformation remains when the unloading process is completed at point *J*.

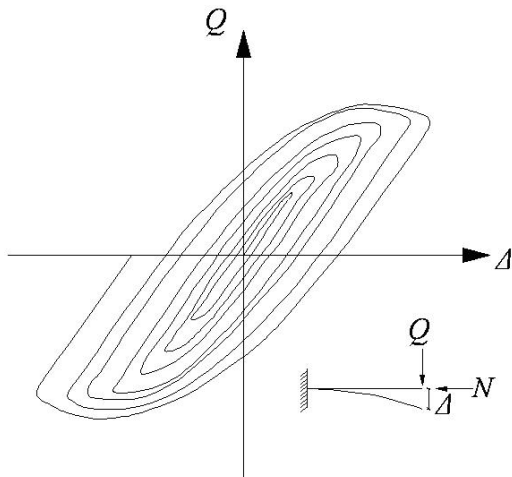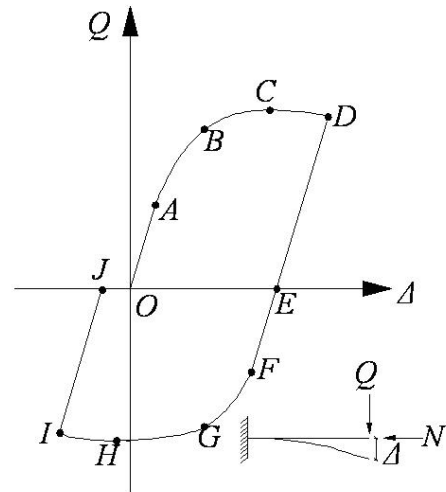
Figure 1. Hysteresis Loop of Cantilever   Figure 2. Full-range Behavior of Cantilever

4.   BUCKLING OF THE MEMBER

4.1   Influences to Mechanical Behavior of the Member Caused by Buckling

Influences to mechanical behavior of the structural member caused by buckling can be illuminated by cyclic loading experiment on circular tube (Chen and Sugimoto [7]). Hysteresis loop of the experiment is illustrated in Figure 3, and full-range behavior of the circular tube subjected to once cycling loading is illustrated in Figure 4. The curve in Figure 4 can be divided into 9 segments: (1) *O-A* is elastic loading segment; (2) the experimental specimen is circular tube with initial bending imperfection, thus the load-displacement curve in segment *A-B* exhibits distinct nonlinearity. Buckling criteria is met at point *B*; (3) the bearing capacity of the member decreases in segment *B-C*, and the plastic hinge forms in the central section of the member as a combine action of both

the axial compression force and the additional bending moment; (4) *C-D* is the unloading segment; (5) *D-E* is the elastic tension segment; (6) as the tension force increases, the plastic zone forms in the central section in segment *E-F*; (7) the member is nearly straightened in segment *F-G*, and the plastic hinge forms in the central section of the member once again as a combine action of both the axial compression force and the additional bending moment; (8) the member is completely straightened in segment *G-H*; (9) *H-I* is the elastic unloading segment, and the residual deformation remains when unloading process is completed. When unloading occurs at point *G*, *G-I* is the elastic unloading segment. It can be seen that mechanical behaviors of the member change a lot after the member buckles.
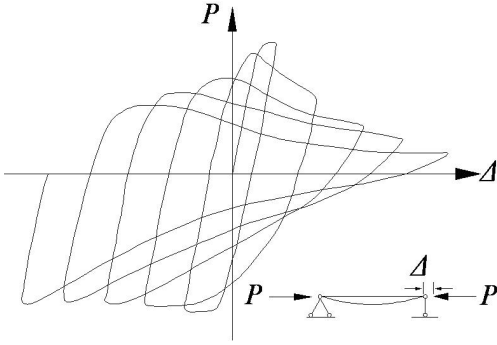
Figure 3. Hysteresis Loop of Circular Tube   Figure 4. Full-range Behavior of Circular Tube
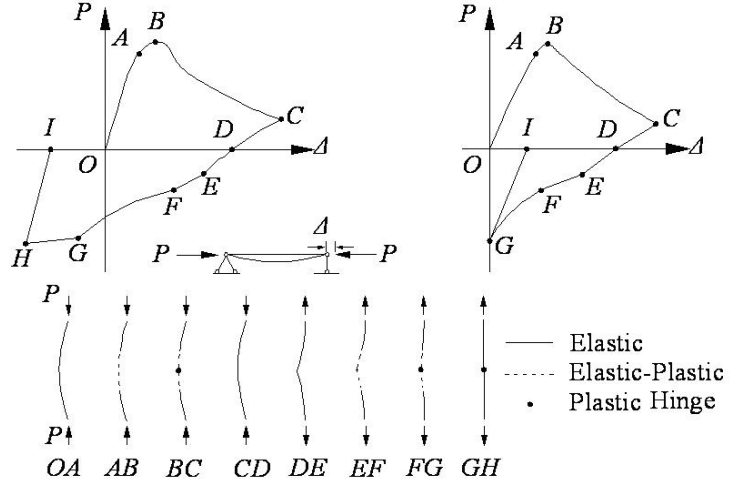
4.2   Buckling Criteria for Circular Tube

Members of single layer latticed shells, which bear spatial forces, are mainly circular tubes. According to a large number of experiments, the buckling criteria equation for circular tube bearing spatial forces is proposed by ISO (ISO [8]):

$$I\left(f_c, f_{b1}, f_{b2}\right) = \frac{f_c}{F_c} + \frac{1}{F_b}\sqrt{\left(\frac{c_{m1}f_{b1}}{1-\dfrac{f_c}{F_{e1}}}\right)^2 + \left(\frac{c_{m2}f_{b2}}{1-\dfrac{f_c}{F_{e2}}}\right)^2} \tag{1}$$

Where $f_c = P/A$ is the axial compression stress, P and A are axial compression force and cross-sectional area respectively; f_{b1} and f_{b2} are the maximum bending stresses about the cross-section local 1 and 2 axes, and $f_{b1} = M_1/W_e$, $f_{b2} = M_2/W_e$, where W_e is the section modulus of elasticity; c_{m1} and c_{m2} are reduction factors corresponding to the cross-section directions 1 and 2 respectively, and $c_{m1} = c_{m2} = 0.85$; F_{e1} and F_{e2} are Euler buckling stresses corresponding to the local 1 or 2 direction, and $F_{e1} = F_{yc}/\lambda_1^2$, $F_{e2} = F_{yc}/\lambda_2^2$, $\lambda_1 = k_1L_1/\pi i\sqrt{F_{yc}/E}$, $\lambda_2 = k_2L_2/\pi i\sqrt{F_{yc}/E}$, where L_1 and L_2 are the unbraced lengths for the local 1 and 2 directions, k_1 and k_2 are the effective length factors in the local 1 and 2 directions, i is the radius of gyration; F_c and F_b are the characteristic axial compressive stress and the characteristic bending stress respectively, where

$$F_c = \begin{cases} \left(1.0 - 0.28\lambda^2\right)F_{yc} & \lambda \leq 1.34 \\ \dfrac{0.89282978}{\lambda^2}F_{yc} & \lambda > 1.34 \end{cases} \tag{2}$$

$$F_b = \begin{cases} \dfrac{W_p}{W_e}\sigma_s & \dfrac{\sigma_s D}{Et} \leq 0.051 \\ \left(1.133386 - 2.58\dfrac{\sigma_s D}{Et}\right)\dfrac{W_p}{W_e}\sigma_s & 0.0517 < \dfrac{\sigma_s D}{Et} \leq 0.103 \\ \left(0.945198 - 0.76\dfrac{\sigma_s D}{Et}\right)\dfrac{W_p}{W_e}\sigma_s & 0.1034 < \dfrac{\sigma_s D}{Et} \leq \dfrac{120\sigma_s}{E} \end{cases} \tag{3}$$

Where F_{yc} is the characteristic local buckling stress.

$$F_{yc} = \begin{cases} \sigma_s & \dfrac{5\sigma_s D}{3Et} \leq 0.170 \\ \left(1.04654873 - 0.27381606\dfrac{5\sigma_s D}{3Et}\right)\sigma_s & 0.170 < \dfrac{5\sigma_s D}{3Et} \leq 1.911 \\ \dfrac{0.6Et}{D} & \dfrac{5\sigma_s D}{3Et} > 1.911 \end{cases} \tag{4}$$

Where σ_s is the yield stress; D is the outside diameter and t is the thickness of tube wall; $\lambda = \max\left(\lambda_1, \lambda_2\right)$; $W_p = [D^3 - \left(D - 2t\right)^3]/6$.

The member gets buckled when $I\left(f_c, f_{b1}, f_{b2}\right) \geq 1.0$. To prevent misjudgment in cases where negligible axial force exists with large bending moments, an additional inequality is used. This additional check, called the strength equation, takes the following form:

$$S\left(f_c, f_{b1}, f_{b2}\right) = \frac{f_c}{F_{yc}} + \frac{1}{F_b}\sqrt{f_{b1}^2 + f_{b2}^2} \tag{5}$$

Thus the buckling criteria for circular tube bearing spatial forces is

$$\begin{cases} I\left(f_c, f_{b1}, f_{b2}\right) \geq 1.0 \\ S\left(f_c, f_{b1}, f_{b2}\right) \leq 1.0 \end{cases} \tag{6}$$

It is the buckling critical state of the circular tube when $I\left(f_c, f_{b1}, f_{b2}\right) = 1.0$ and $S\left(f_c, f_{b1}, f_{b2}\right) \leq 1.0$. The buckling critical axial force is

$$P_{cr} = f_c A \tag{7}$$

5.   MEMBER CALCULATION MODEL

5.1   Calculation Model of the Pre-buckling Member

Displacement interpolation equations of the member considering second order effect are derived based on the deformed configuration. Deformed configuration of the member bearing axial tension force, shear force and bending moment is illustrated in Figure 5.
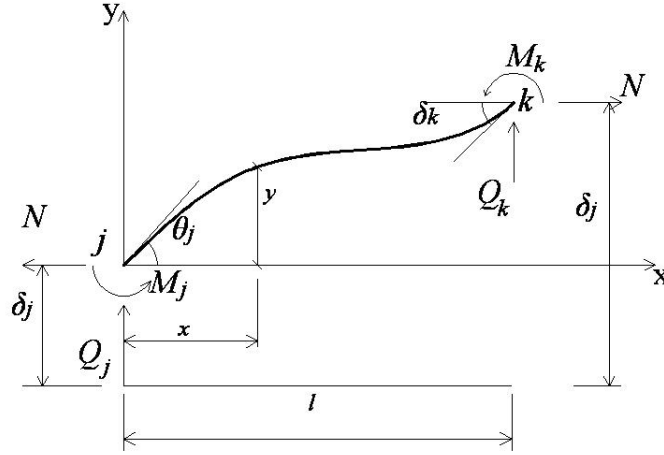

Figure 5. Deformed Configuration of the Member

Translational displacements caused by bending moment and shear force are y_M and y_Q respectively. $y_M'' = -M/EI$ and $y_Q' = -\mu Q/(GA)$, so second derivative of the total lateral displacement of arbitrary section of the member is given by the following equation:

$$y'' = y_M'' + y_Q'' = -\frac{M}{EI} - \frac{\mu}{GA} \cdot \frac{dQ}{dx} = -\frac{M}{EI} = \frac{Q_j}{EI} x - \frac{M_j - N}{EI}$$ (8)

Where μ is shear-shape coefficient; E and G are elasticity modulus and shear modulus of the material; I is sectional inertia moment.

Differential equation of the total lateral displacement of arbitrary section of the member bearing compression axial force has the same expression as Eq. 8 except for the sign before variable N which turns to be positive. Introducing boundary condition: $y = 0$ when $x = 0$ and $y = \delta_k - \delta_j$ when $x = l$, lateral displacement interpolation equations expressed by stability functions for both tension and compression members can be derived from the differential equations. Maclaurin series expansion is used to replace the stability functions and the uniform lateral displacement interpolation equations for both tension and compression members are given by the following equation:

$$y = N_1 \delta_j + N_2 \theta_j + N_3 \delta_k + N_4 \delta_k$$ (9)

Differential equation of the rotation displacement of arbitrary section of the member is given by the following equation:

$$\theta(x) = \frac{dy}{dx} - \frac{\mu Q}{GA} \tag{10}$$

Similarly, Maclaurin series expansion is used to replace the stability functions in the solution of Eq. 10 and the uniform rotation displacement interpolation equations for both tension and compression members are given by the following equation:

$$\theta(x) = N_5 \delta_j + N_6 \theta_j + N_7 \delta_k + N_8 \delta_k \tag{11}$$

Parameters in Eq. 10 and Eq. 11 are defined as follows:

$$N_1 = -\frac{1}{\varphi}\chi_o \cdot \psi_o + \frac{1}{\varphi}\rho\xi\left[1+\chi_j\right]\left[1+\psi_j\right] - \frac{\eta}{\varphi}\rho\xi\left[1+\chi_j\right] \tag{12a}$$

$$N_2 = -\frac{l\psi_o}{\eta\varphi}\left[\left(1+\chi_j\right) - \eta\left(1+\chi_o\right)\right] - \frac{x}{\eta\varphi}\left[\chi_{op} - \rho_0\eta\left(1+\chi_j\right)\right]\cdot\left(1+\psi_j\right) - \frac{x}{\varphi}\chi_o \tag{12b}$$

$$N_3 = \frac{1}{\varphi}\chi_o\psi_o - \frac{1}{\varphi}\rho\xi\left(1+\chi_j\right)\cdot\left(1+\psi_j\right) + \frac{\eta\rho\xi}{\varphi}\left(1+\chi_j\right) \tag{12c}$$

$$N_4 = \frac{l\psi_o}{\eta\varphi}\left[\eta - \left(1+\chi_j\right)\right] + \frac{x}{\eta\varphi}\chi_o\left(1+\psi_j\right) - \frac{x}{\varphi}\chi_o \tag{12d}$$

$$N_5 = -\frac{\rho\xi}{l\varphi}\chi_o\left(1+\psi_j\right) + \frac{\rho}{l\varphi}\left(1+\chi_j\right)\cdot\left(1+\psi_o\right) - \frac{\rho\eta^2}{l\varphi}\left(1+\chi_j\right) \tag{12e}$$

$$N_6 = -\frac{\rho\xi}{\eta\varphi}\left[\left(1+\chi_j\right) - \eta\left(1+\chi_o\right)\right]\cdot\left(1+\psi_j\right) + \frac{1}{\eta\varphi}\left[\frac{\eta\rho_0}{l^2}\left(1+\chi_j\right) - \chi_o\right]\cdot\left(1+\psi_o\right) - \frac{\eta}{\varphi}\chi_o \tag{12f}$$

$$N_7 = \frac{\rho\xi}{l\varphi}\chi_o\left(1+\psi_j\right) - \frac{\rho}{l\varphi}\left(1+\chi_j\right)\cdot\left(1+\psi_o\right) + \frac{\rho\eta^2}{l\varphi}\left(1+\chi_j\right) \tag{12g}$$

$$N_8 = -\frac{\rho\xi}{\eta\varphi}\left(1-\eta+\chi_j\right)\cdot\left(1+\psi_j\right) + \frac{1}{\eta\varphi}\chi_o\left(1+\psi_o\right) - \frac{\eta}{\varphi}\chi_o \tag{12h}$$

where $\eta = 1 + \mu N/GA$; $\rho = |N|l^2/\eta EI$; $\rho_0 = Nl^2/\eta EI$; $\chi_o = \sum\limits_{n=1}^{\infty}\rho^n/(2n)!$; $\chi_j = \sum\limits_{n=1}^{\infty}\rho^n/(2n+1)!$;

$\psi_o = \sum\limits_{n=1}^{\infty}(\rho\xi^2)^n/(2n)!$; $\psi_j = \sum\limits_{n=1}^{\infty}(\rho\xi^2)^n/(2n+1)!$; $\varphi = 2 - 2(1+\chi_o) + \rho\eta(1+\chi_j)$; $\xi = x/l$.

Axial interpolation equations of the member are defined by linear equations. Extend the displacement interpolation equations of the planar member to three-dimensional space, and displacement interpolation equation matrix of the spatial member is given by the following equation:

$$u_0 = Nu = \begin{bmatrix} 1-x/l & 0 & 0 & 0 & 0 & 0 & x/l & 0 & 0 & 0 & 0 & 0 \\ 0 & N_1 & 0 & 0 & 0 & N_2 & 0 & N_3 & 0 & 0 & 0 & N_4 \\ 0 & 0 & N_1 & 0 & -N_2 & 0 & 0 & 0 & N_3 & 0 & -N_4 & 0 \\ 0 & 0 & 0 & 1-x/l & 0 & 0 & 0 & 0 & 0 & x/l & 0 & 0 \\ 0 & 0 & -N_5 & 0 & N_6 & 0 & 0 & 0 & -N_7 & 0 & N_8 & 0 \\ 0 & N_5 & 0 & 0 & 0 & N_6 & 0 & N_7 & 0 & 0 & 0 & N_8 \end{bmatrix} u = \begin{bmatrix} N_{ux} \\ N_{uy} \\ N_{uz} \\ N_{\theta x} \\ N_{\theta y} \\ N_{\theta z} \end{bmatrix} u$$

$$(13)$$

Where u_0 is the centroid displacement of arbitrary section of the member, and $u_0 = \{u_{x0} \ u_{y0} \ u_{z0} \ \theta_{x0} \ \theta_{y0} \ \theta_{z0}\}$; u is the centroid displacement of the end section of the member, and $u = \{u_{xj} \ u_{yj} \ u_{zj} \ \theta_{xj} \ \theta_{yj} \ \theta_{zj} \ u_{xk} \ u_{yk} \ u_{zk} \ \theta_{xk} \ \theta_{yk} \ \theta_{zk}\}$.

Divide the displacement increment of the end of the member into elastic component and plastic component:

$$\Delta u = \Delta u^e + \Delta u^p \tag{14}$$

Where Δu, Δu^e and Δu^p are the increments of total displacement, elastic displacement and plastic displacement respectively.

Equilibrium equation of end section j is:

$$F_{ij} = \sum_{k=1}^{2} \sum_{s=1}^{6} K_{ij\,sk}^{e} \left(u_{sk} - u_{sk}^{p} \right) \tag{15}$$

Where F_{ij} is the component of section force in end section j; $K_{ij\,sk}^{e}$ is the element of the element elastic stiffness matrix; u_{sk}, u_{sk}^{p} are the component of the total displacement and the component of plastic displacement of end section k respectively.

The plastic displacement, which is an accumulation of increments of the plastic displacement, is given by the following equation:

$$\Delta u_k^p = \Delta \lambda_k \frac{\partial \Phi_k}{\partial S_k} \tag{16}$$

Where Δu_k^p is the vector of plastic displacement increment of the end section k; $\Delta \lambda_k$ is the proportion coefficient; $S_k = F_k - \alpha_k$, α_k is the vector of back stress of end section k; Φ_k is the yield surface equation of end section k which is given by the following equation:

$$\Phi_k = \left(\frac{N_{xk} - \alpha_{Nxk}}{N_{xu}} \right)^2 + \left(\frac{M_{xk} - \alpha_{Mxk}}{M_{xu}} \right)^2 + \left(\frac{M_{yk} - \alpha_{Myk}}{M_{yu}} \right)^2 + \left(\frac{M_{zk} - \alpha_{Mzk}}{M_{zu}} \right)^2 - 1 \tag{17}$$

Where N_{xu}, M_{xu}, M_{yu} and M_{zu} represent the cross-sectional bearing capacities of the member at yield: the axial force and three moments, respectively; N_{xk} is the axial force of the end section k; M_{yk} and M_{zk} are bending moments of the end section k about the local 1- and 2-directions of the cross section of the member respectively; M_{xk} is torsion of the end section k; α_{Nxk}, α_{Mxk}, α_{Myk} and α_{Mzk} are back stress components respectively.

The cross end section k yields and the plastic hinge forms when $\Phi_k \geq 0$.

5.2   Calculation Model of the Post-buckling Member

Marshall model (Marshall, Gates, and Anagnostopoulos [9]), which is the mathematical description of the curve illustrated in Figure 4, is used to simulate the post-buckling member. The essence of Marshall model is the envelope of hysteresis loop of the inelastic circular tube (Figure 6). The envelope can be divided into 7 segments: (1) *A-F* is the linear tension segment; (2) *F-F′* is the tension yielding segment; (3) *A-B* is the linear compression segment; (4) *B-C* is the first post buckling segment; (5) *C-D* is the second post buckling segment; (6) *D-E* is the first tension straightening segment; (7) *E-F* is the second tension straightening segment. When reverse loading occurs at points on the boundary of the enclosed part of the envelope (such as point *B′*, *C′* or *D′*), the member exhibits damaged elastic behavior which is determined by drawing a line from the point on the envelope to the tension yield point (force value P_y). As long as the force and axial strain remain inside the enclosed part of the envelope, the force response is linear elastic with a modulus equal to the damaged elastic modulus. The axial force in the element is required to stay inside or on the envelope. When tension yielding occurs, the enclosed part of the envelope translates along the strain axis by an amount equal to the plastic strain. Coefficients in Figure 6 are defined as follows: $\gamma = 0.02$; $\beta = 0.02$; $\zeta = \min(1.0, \ 5.8(t/D)^{0.7}/0.95)$; $\kappa = 0.28$; $\alpha = 0.03 + 0.004L/D$, where L is the length of the member; ultimate elastic axial force of the member is given by the following equation:

$$P_y = 0.95\sigma_s A \tag{18}$$
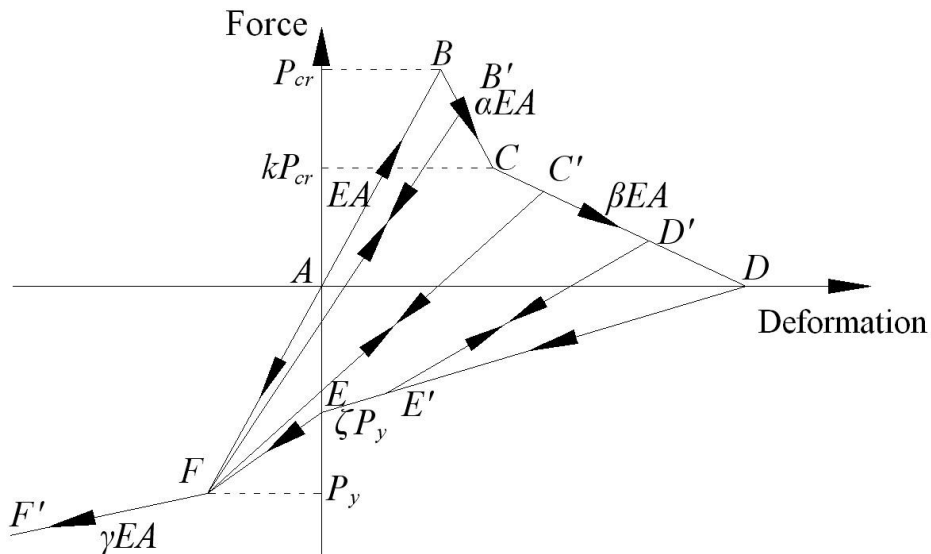
Figure 6. Marshall Model

The structural member is firstly simulated by pre-buckling calculation model until Eq. 6 is met, and then Marshall model is used. If $\Phi \geq 0$ when Eq. 6 is med, the member performs buckling type I; otherwise it performs buckling type II. Plastic hinge of the end section of the member is simulated by pre-buckling calculation model, and that of the central section is simulated by Marshall model.

6.   CAUSES OF STRUCTURAL DYNAMIC DAMAGES

Based on the refined member calculation model, numerical structure models of commonly used single layer latticed shells are created to analyze the causes of dynamic damages of the structures under earthquakes.

6.1   Single Layer Spherical Latticed Shells

Take a Kiewitt single layer spherical latticed shell with the span of 40m and the rise-span ratio of 1/3 as an example. The structure consists of circular tubes of Φ114×3.0, Φ127×3.5 and Φ140×4.5 of steel Q235 (yield strength of 235 MPa), and bears surface load of 2.00kN/m² and seismic excitation of El Centro wave with peak acceleration of 620gal and duration of 12s.

Calculation results indicate that all of the 8 members in the structure central ring (Figure 7) buckle in 0.92s~0.93s and perform buckling type II. Structure internal forces redistribute due to reductions of bearing capacities of the buckling members. Then the number of buckling member increases rapidly and the structural bearing capacity is weakened as a result. At 1.94s the structural bearing capacity cannot keep balance with the seismic action, and the structure damages consequently. The structural strain energy increases suddenly with the strengthening of seismic action in 0.90s~0.92s (Figure 8). The zoomed drawing shows that there are two slight fluctuations in the curve. They correspond to the member buckling processes which make the strain energy release. The strain energy releases greatly in 0.94s~0.95s, corresponding to the structural damage process.
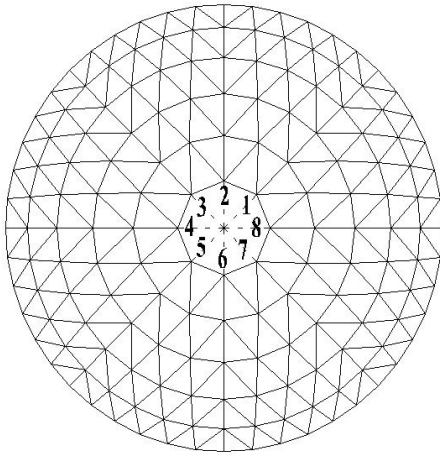
Figure 7. Buckling Members at 0.93s   Figure 8. Time History of Structural Strain Energy
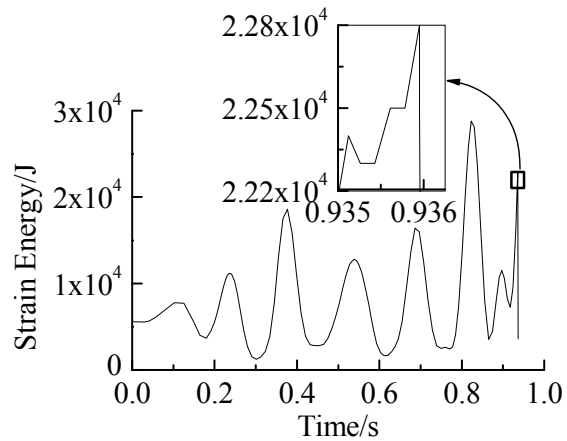
The peak acceleration of the seismic action is decreased to 350gal for a further investigation. Numerical results indicate that some structural members undergo buckle-straighten processes repeatedly and perform buckling type II all alike. The number of the buckling member changes continuously with the dynamic change of structural bearing capacity. The structure can hold yet with 32 buckling members at 1.69s (Figure 9) when the seismic action is not very strong. Thereafter some of the buckling members are straightened again. At 1.78s the structure cannot hold

the stronger seismic action and damages with 9 buckling members which are illustrated in Figure 10.
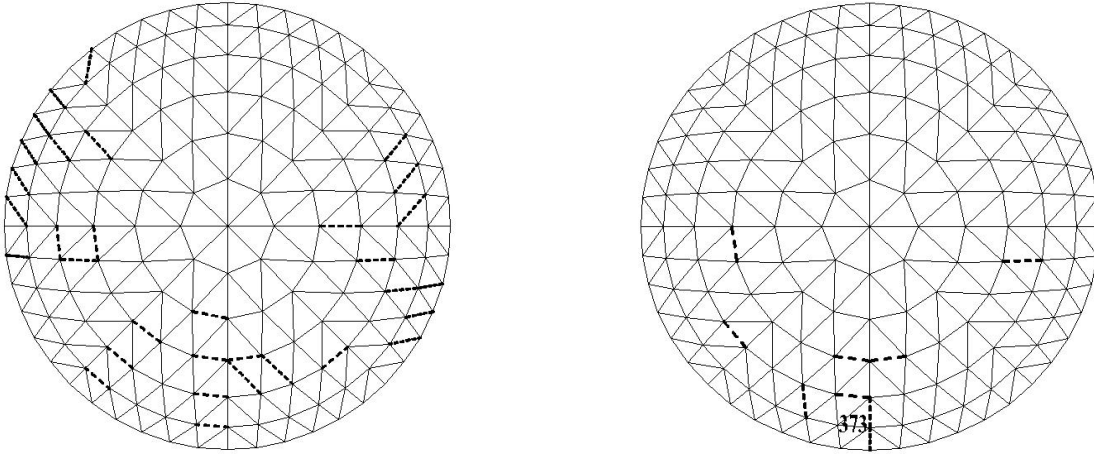
Figure 9. Buckling Members at 1.69s   Figure 10. Buckling Members when Structure Damages

Comparing Figure 9 with Figure 10, it can be seen that the structural damage is determined by the dynamic balance between the structural bearing capacity and the seismic action rather than the number of buckling members.

Axial fore time history of member 373 (marked in Figure 10) is illustrated in Figure 11. The member buckles when axial force reaches its limit buckling axial force of 164kN. After the member buckles, the axial force turns small rapidly. It can be seen that the member buckles twice.
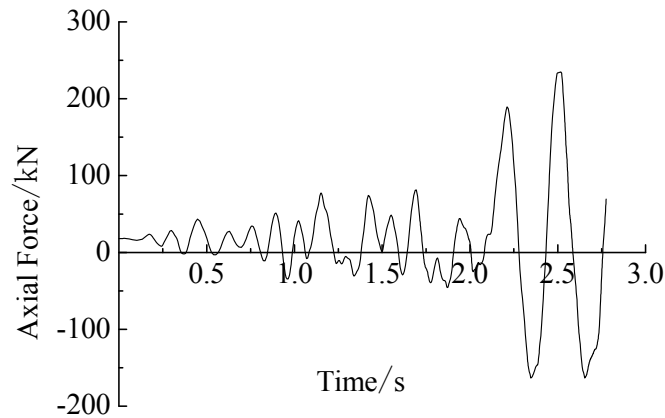
Figure 11. Time History of Axial Force of Member 373

The structural members are simulated by the general beam element of general finite element analysis program, and the axial fore time history of member 373 is illustrated in Figure 12. It can be seen that the maximum axial fore in member 373 reaches 246.14kN which has far surpassed the limit buckling axial force value, so the bearing capacities of the members are overestimated. The structural dynamic bearing capacity can keep balance with the seismic action in the entire 12s, and the error conclusion that the structure does not damage may be made consequently.
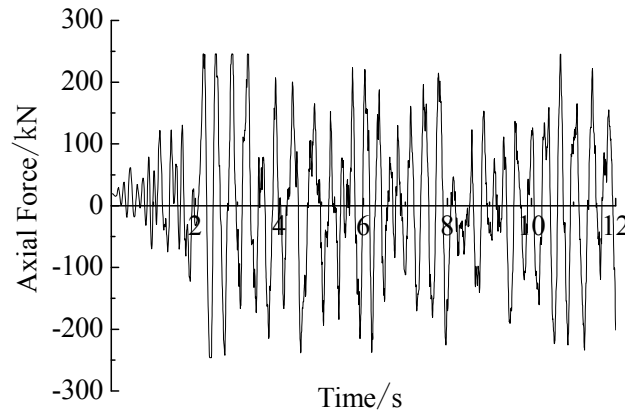
Figure 12. Axial Fore Time Histories of Member 373 Calculated by FEM Program

Numerical models of five kinds of commonly used single layer spherical latticed shells with the uniform span of 40m and different rise-span ratios of 1/4, 1/5, 1/6 and 1/7 are created respectively for the parameter analysis. Seismic excitation of El Centro wave with peak acceleration of 900gal and duration of 12s is applied. Numbers of buckling members and plastic hinges in the end sections of the members when structures damage are presented in Table 1.

Table 1. Numbers of Buckling Members and Plastic Hinges when
Single Layer Spherical Latticed Shells Damage

Rise-span ratio	Buckling members/ Plastic hinges	Types of single layer spherical latticed shell				
		Lamella grid	Schwedler	Ribbed type	Three-way grid	Kiewitt
1/4	Buckling members	25	27	25	29	32
	Plastic hinges	0	0	0	0	0
1/5	Buckling members	21	22	24	28	29
	Plastic hinges	0	0	0	0	0
1/6	Buckling members	18	18	20	22	22
	Plastic hinges	0	0	0	0	0
1/7	Buckling members	17	16	17	18	20
	Plastic hinges	1	2	0	0	0

Table 1 shows that the members of single layer spherical latticed shells under earthquake perform buckling type Ⅱ mainly. Structures of bigger rise-span ratios have more buckling members when they damage. Plastic hinges of the end sections of the members are quite rare in the structures. Except for the two structures of lamella grid and Schwedler with the rise-span ratio of 1/7, there are no plastic hinges in the end sections of the members in other single layer spherical latticed shells when they damage. Therefore dynamic damages of single layer spherical latticed shells are caused by buckling members which weaken the structural bearing capacity.

6.2   Single Layer Cylindrical Latticed Shells

Take a three-way grid single layer cylindrical latticed shell with the span of 15m, the length of 21m and the rise-span ratio of 1/2 as an example. The structure consists of circular tubes of Φ114×3.0, Φ127×3.5 and Φ140×4.5 of steel Q235, and bears surface load of 1.00kN/m^2 and seismic excitation of El Centro wave with peak acceleration of 620gal and duration of 12s.

Numerical results indicate that it is the end section of the member of single layer cylindrical latticed shell yields firstly. Along with the increment of the load, plastic hinges form in the end sections of some members which cannot bear bigger bending moments and shear forces while the deformations become larger rapidly. This causes the redistribution of the structural internal forces, and more plastic hinges form in the end sections of the conjoint members. The concentrative plastic hinges in the end sections of conjoint members may make parts of the structure turn to mechanism. At 6.04s 43 plastic hinges form in the end sections of the members as illustrated in Figure 13 (black dots represent plastic hinges, and hollow rings represent plastic zones where plastic hinges have not formed yet.). If seismic action weakens afterward, the plastic hinges could disappear and residual deformations remain. The number of plastic hinges and positions where they form change continuously and it makes the consequent change of the structural bearing capacity. At 6.13s the structure cannot hold the stronger seismic action and damages with 26 plastic hinges in the end sections of the members which are illustrated in Figure 14.
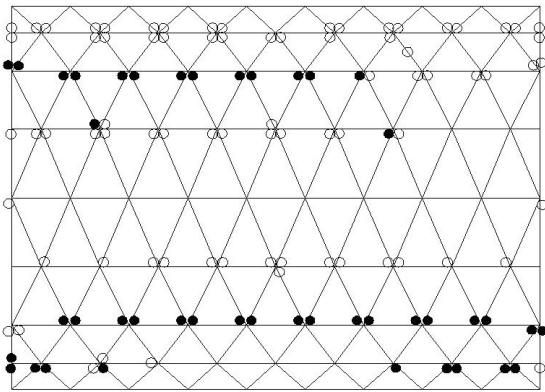
Figure 13. Plastic Hinges at 6.04s   Figure 14. Plastic Hinges when Structure Damages
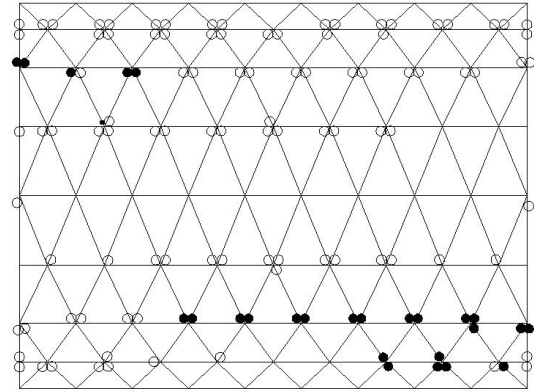
Comparing Figure 13 with Figure 14, it can be seen that the structural damage is determined by the dynamic balance between the structural bearing capacity and the seismic action rather than the number of plastic hinges.

Numerical models of four kinds of commonly used single layer cylindrical latticed shells with the uniform span of 15m, the uniform length of 21m, and different rise-span ratios of 1/2, 1/3, 1/4 and 1/5 are created respectively for the parameter analysis. Seismic excitation of El Centro wave with peak acceleration of 900gal and duration of 12s is applied. Numbers of buckling members and plastic hinges of the end sections of the members when structures damage are presented in Table 2.

Table 2. Numbers of Buckling Members and Plastic Hinges when
Single Layer Cylindrical Latticed Shells Damage

Rise-span ratio	Buckling members/ Plastic hinges	Types of single layer cylindrical latticed shell			
		Orthogonal grid with one bracing	Orthogonal grid with two bracings	Lamella grid	Three-way grid
1/2	Buckling members	1	0	0	1
	Plastic hinges	34	25	16	24
1/3	Buckling members	0	0	0	0
	Plastic hinges	37	26	21	29
1/4	Buckling members	0	0	0	0
	Plastic hinges	42	30	22	30
1/5	Buckling members	0	0	0	0
	Plastic hinges	43	35	27	43

Table 2 shows that the members of single layer cylindrical latticed shells under earthquake perform buckling type I mainly. Structures of smaller rise-span ratios have more plastic hinges in the end sections of the members when they damage. Buckling members are quite rare in the structures. Except for the two structures of orthogonal grid with one bracing and three-way grid with the rise-span ratio of 1/2, there are no buckling members in other types of the single layer cylindrical latticed shells when they damage. Therefore dynamic damages of single layer cylindrical latticed shells are caused by concentrative plastic hinges in the end sections of some members which make parts of the structure turn to mechanisms.

6.3   Single Layer Elliptic Paraboloid Latticed Shells

Take an orthogonal grid with one bracing single layer elliptic paraboloid latticed shell with the span of 30m, the length of 48m and the rise-span ratio of 1/3 as an example. The structure consists of circular tubes of $\Phi114\times4.0$, $\Phi121\times4.0$, $\Phi146\times6.0$ and $\Phi152\times6.0$ of steel Q235, and bears surface load of $1.00kN/m^2$ and seismic excitation of El Centro wave with peak acceleration of 620gal and duration of 12s.

Numerical results indicate that buckling members and plastic hinges in the end sections of the members appear together in large numbers and the members of the single layer elliptic paraboloid latticed shell subjected to seismic excitations perform both the buckling type I and buckling type II. Time histories of the numbers of buckling members and plastic hinges in the end sections are illustrated in Figure 15 and Figure 16 respectively. The recurrent buckle-straighten processes of the members weaken the structural bearing capacity, and the recurrent form-disappear processes of the plastic hinges of the end sections make parts of the structure turn to mechanisms. The structure damages as a combined action of the two causes mentioned above. Buckling members and plastic hinges in the end sections when the structure damages are illustrated in Figure 17.
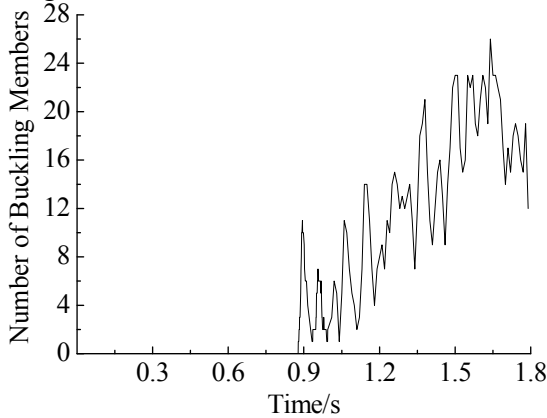
Figure 15. Number Change of Buckling Members   Figure 16. Number Change of Plastic Hinges
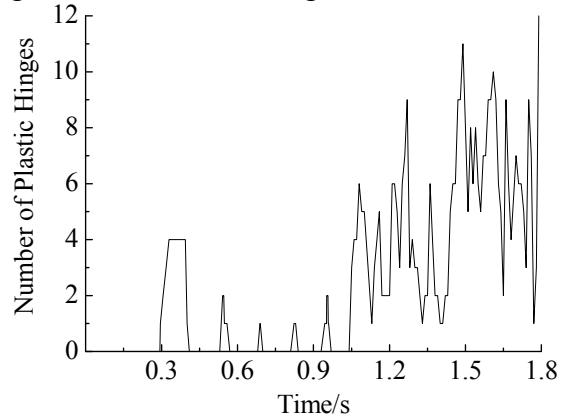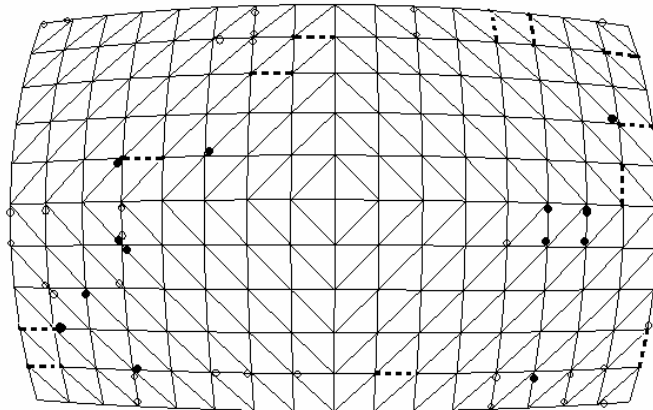
Figure 17. Buckling Members and Plastic Hinges when Structure Damages

Numerical models of two kinds of commonly used single layer elliptic paraboloid latticed shells with the uniform span of 30m, the uniform length of 48m, and different rise-span ratios of 1/3, 1/4, 1/5 and 1/6 are created respectively for the parameter analysis. Seismic excitation of El Centro wave with peak acceleration of 900gal and duration of 12s is applied. Numbers of buckling members and plastic hinges in the end sections of the members when structures damage are presented in Table 3.

Table 3. Numbers of Buckling Members and Plastic Hinges when
Single Layer Elliptic Paraboloid Latticed Shells Damage

Rise-span ratio	Buckling members/ Plastic hinges	Types of single layer elliptic paraboloid latticed shell	
		Orthogonal grid with one bracing	Three-way grid
1/3	Buckling members	28	26
	Plastic hinges	15	25
1/4	Buckling members	25	26
	Plastic hinges	16	29
1/5	Buckling members	22	22
	Plastic hinges	20	30
1/6	Buckling members	20	15
	Plastic hinges	23	33

Table 3 shows that the members of the single layer elliptic paraboloid latticed shell under earthquake perform both the buckling type I and buckling type Ⅱ. Structures of bigger rise-span ratios have more buckling members and fewer plastic hinges in the end sections of the members when they damage. Dynamic damages of single layer elliptic paraboloid latticed shells are caused by buckling members which weaken the structural bearing capacity and concentrative plastic hinges in the end sections of some members which make parts of the structure turn to mechanisms together.

7.   CONCLUSIONS

The dynamic damages causes of single layer latticed shells subjected to seismic excitations based on refined member calculation model are studied in this paper. Based on the analysis, some conclusions can be drawn as follows:

(1) If the members of single layer latticed shells are simulated by general beam element of general finite element analysis program, the elastic-plastic element stiffness matrix of the member is not accurate and the buckling of the member cannot be simulated as well. By this method, the structural bearing capacity will be overestimated.

(2) Two buckling types of the member of single layer latticed shells are presented. Buckling type I: the plastic hinge forms in the end section of the member, and the member slenderness ratio gets bigger. This may cause buckling of the member. Buckling type Ⅱ: the member bears compression axial force plenty big and the buckling critical condition is met without the plastic hinge forming in the end section.

(3) The pre-buckling and post-buckling mechanical behaviors of the structural member are simulated by different models, and the refined member calculation model is established. By this model the second order effect of the member is considered, and the possible buckle-straighten processes of the members and the form-disappear processes of the structure under earthquake can be simulated.

(4) The dynamic damages of the structures under earthquake are determined by the dynamic balance between the structural bearing capacity and the seismic action rather than the

number of buckling members or the plastic hinges.

(5) Dynamic damage causes of single layer latticed shells vary with different structural types: dynamic damages of single layer spherical latticed shells are caused by buckling members which weaken the structural bearing capacity; dynamic damages of single layer cylindrical latticed shells are caused by concentrative plastic hinges in the end sections of some members which make parts of the structure turn to mechanisms; dynamic damages of single layer elliptic paraboloid latticed shells are caused by combined actions of the two causes mentioned above.

ACKNOWLEDGEMENTS

REFERENCES

[1]   Kani, I.M. and Heidari, A., "Automatic Two-Stage Calculation of Bifurcation Path of Perfect Shallow Reticulated Domes", Journal of Structural Engineering, 2007, Vol. 133, No. 2, pp. 185-194.

[2]   Yamada, S., Takeuchi, A., Tada, Y., et al., "Imperfection-Sensitive Overall Buckling of Single- Layer Lattice Domes", Journal of Engineering Mechanics, 2001, Vol. 127, No. 4, pp. 382-386.

[3]   Hearn, G. and Adams, E., "Shape Selection for Lattice Structures", Journal of Structural Engineering, 2006, Vol. 132, No. 11, pp. 1713-1720.

[4]   Morris, N.F., "Effect of Imperfections on Lattice Shells", Journal of Structural Engineering, 2007, Vol. 117, No. 6, pp. 1796-1814.

[5]   Kani, I.M. and McConnel, R.E., "Collapse of Shallow Lattice Domes", Journal of Structural Engineering, 1987, Vol. 113, No. 8, pp. 1806-1819.

[6]   Fan, F., "Report for Refined Research Advances on Disastrous Damages of Long Span Spatial Structures Subjected to Severe Earthquakes", Seminar on Major Program of National Natural Science Foundation of China. Dalian, China, 2009.

[7]   Chen, W.F. and Sugimoto, H., "Stability and Strength of Fabricated Tubular Columns Used in Offshore Structures", Research Report of Purdue University, West Lafayette, U.S.A., 1984.

[8]   International Standards Organization, "Steel Structures: Materials and Design", Specification for the Design and Construction of Steel Structures (ISO 10721-1), 1997.

[9]   Marshall, P.W., Gates, W.E., and Anagnostopoulos, S., "Inelastic Dynamic Analysis of Tubular Offshore Structures", Proceedings of Ninth Annual Offshore Technology Conference, Houston, U.S.A., 1977, pp. 235-246.

ESTIMATION OF STRESS INTENSITY FACTORS IN TUBULAR K-JOINTS USING DIRECT AND INDIRECT METHODS

S.T. Lie[1,*], T. Li[2] and Y.B. Shao[3]

[1]*School of Civil and Environmental Engineering, Nanyang Technological University,
50 Nanyang Avenue, Singapore 639798*
[2]*Maritime Research Centre, Nanyang Technological University,
50 Nanyang Avenue, Singapore 639798*
[3]*School of Civil Engineering, Yantai University, Yantai City 264005, P. R. China*
*(Corresponding author: E-mail: cstlie@ntu.edu.sg)

ABSTRACT: The stress intensity factors at the deepest point and at the crack ends of a surface crack in a tubular K-joint are calculated by direct and indirect methods. In the direct method, the surface crack is modelled explicitly. An automatic mesh generator is developed to produce a well-graded mesh around the crack region. This is achieved by using five types of elements. Thereafter, the stress intensity factors of a surface crack located anywhere along the weld toe at the joint intersection are calculated using the *J*-integral method. The computed values had been verified by experimental test results. In the indirect method, the stress intensity factors are estimated by the T-butt solutions used in conjunction with the stress concentration factors (SCFs) and degree of bending (DOB) of the uncracked tubular K-joint. In this study, a total of 1024 models, covering a wide range of geometrical parameters and crack shapes, have been selected and analyzed. Both approaches are able to produce a safe estimation of stress intensity factors at the deepest point of the surface crack. However, the indirect method is found to be extremely conservative; it overestimates the stress intensity factor values by as much as 190.4% (β=0.5, γ=30, τ=0.5, a/T=0.1, c/a=5) at the deepest point, and 390.7% (β=0.4, γ=30, τ=0.5, a/T=0.5, c/a=8) at the crack ends of the surface crack respectively.

Keywords: Direct method, Indirect method, *J*-integral method, Mesh generator, Stress intensity factor, Surface crack, Tubular K-joint

1. INTRODUCTION

Tubular K-joints used in the offshore structures are always subjected to cyclic loads caused by seawater wave and wind, and hence fatigue failure is a very common phenomenon. It is crucial for structural engineers to be able to estimate the static ultimate strength and the residual life of these damaged joints when surface cracks are discovered during in services. The most effective method to analyze any cracked tubular joint is to use the fracture mechanics approach, based on accurate estimation of stress intensity factors at critical points along the crack front.

In the finite element analysis, the accuracy and convergence of the computed stress intensity factors depend very much on the type of elements, mesh quality, mesh refinement, integration schemes and weld shape modelling around the crack front. It has always been a daunting task to model a true accurate 3D surface crack located along the weld toe in any tubular joint. Some researchers (Cao et al. [1], Bowness and Lee [2]) used two types of elements to simulate the crack front where 3D prism singular and hexahedral elements were used to model the crack front and the field far away from it.

Because of these reasons and as far as the authors are aware, there is no such automatic mesh generator currently available for cracked CHS tubular joints. Therefore, a completely new automatic mesh generator has been developed and improved for this purpose in the past few years (Lie et al. [3], Lie et al. [4], Shao and Lie [5], Shao et al. [6]). This technique uses a sub-division technique whereby the entire K-joint shown on Figure 1 is divided into distinct zones. When a tubular K-joint is subjected to balanced axial loading, the crack generally occurs at the crown location and it is symmetrical about this point. In each zone, the mesh is generated and checked separately. After the

mesh of all the zones have been completed, they are merged together to form the complete model (Figure 1). In the cracked region, five types of elements, i.e. hexahedral, prism, quarter-point collapsed prism, tetrahedron and pyramid elements, are used to model the crack zone (Figure 2), and the other zones of a K-joint. To verify the convergence of these stress intensity factors, the mesh density is doubled as shown in Figure 3. The detailed modelling procedure can be found in (Lie et al. [3], Lie et al. [4], Shao and Lie [5]).
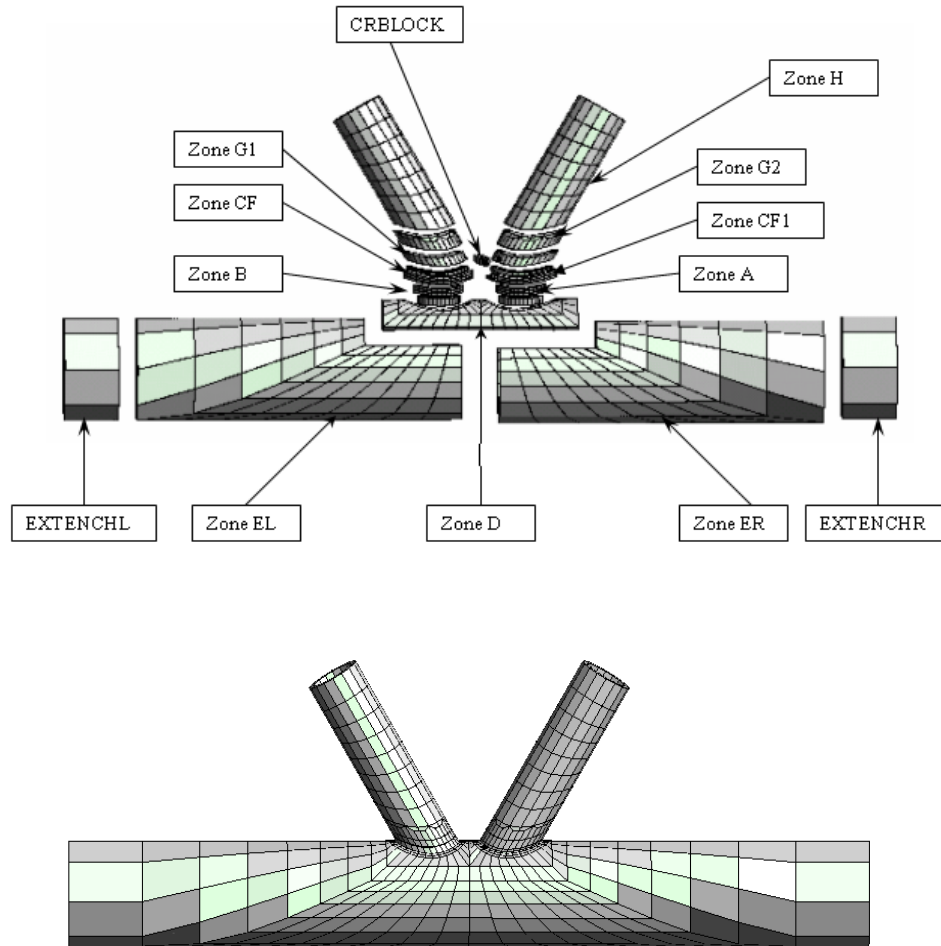
Figure 1. Sub-zone Technique used for a Tubular K-Joint

The generated finite element model of the K-joint has been proven to produce even very accurate Mode-II (K_{II}) and Mode-III (K_{III}) stress intensity factor values along the crack front (Figure 4). For the doubled mesh density, the Mode-I (K_I) stress intensity factors are recalculated and plotted along the crack front as shown in Figure 5. It can be seen that good agreement between the two sets of results demonstrates the convergence. These computed stress intensity factors had also been validated experimentally where a full-scale K-joint specimen shown in Figure 6 was fatigue tested to failure under axial tension and in-plane bending loads (Figures 7 and 8). The crack growth rate at the deepest point, da/dN, was recorded from the experimental measurements (please refer to Lie et al. [7]). The experimental stress intensity factors were then deduced from Paris' equation, and are plotted in Figure 9 together with K_I, K_{II}, K_{III} and K_e values. The detailed validation procedure can be found in (Lie et al. [7]). Hence, the present mesh generation technique is shown to be able to produce accurate stress intensity factors at the deepest point of a surface crack in any tubular K-joint.
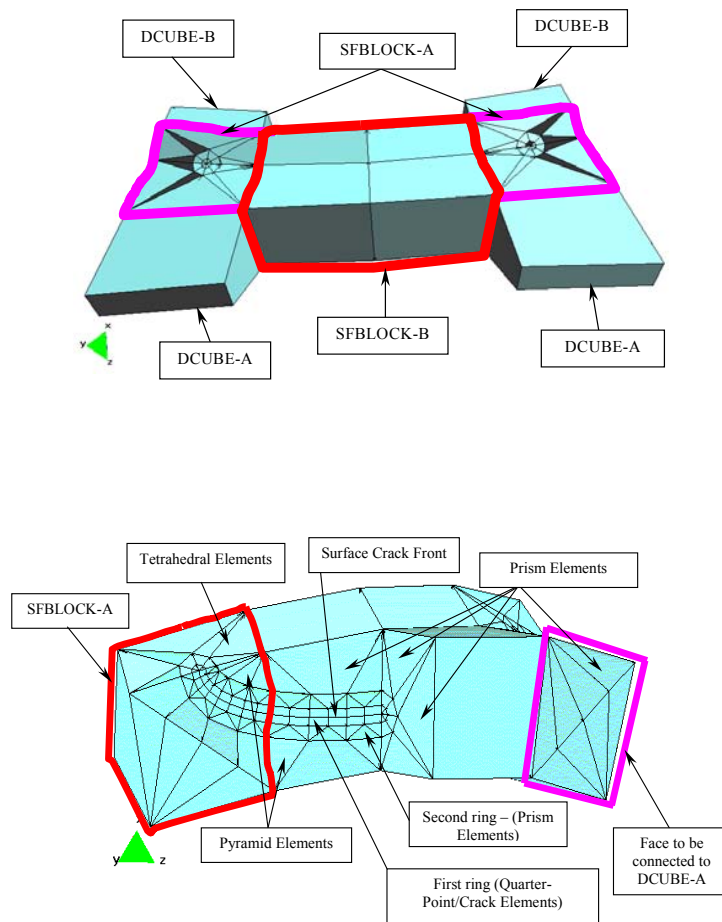
Figure 2. Detailed Mesh of the Surface Crack
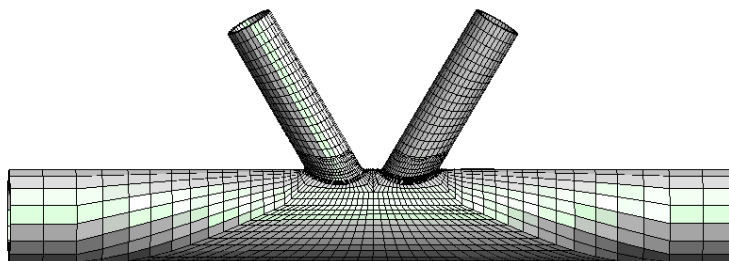
Figure 3. Doubled Mesh Density of the K-joint
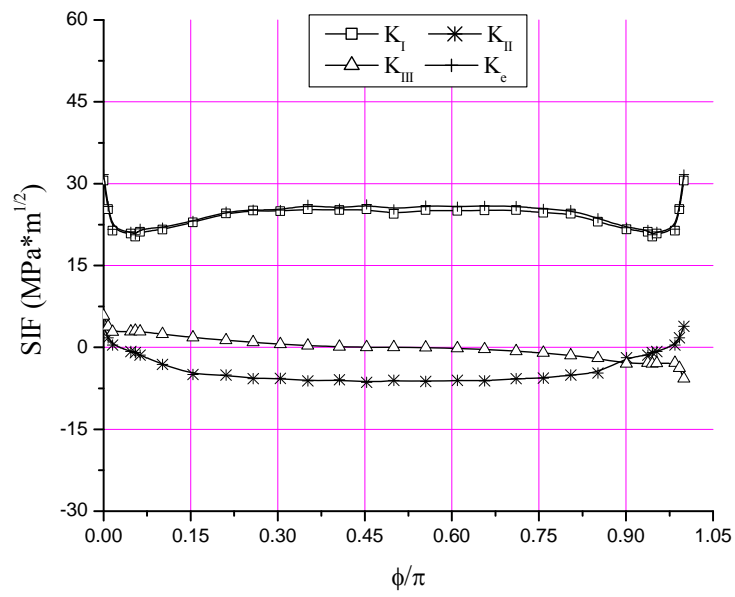
Figure 4. Typical K_I, K_{II}, K_{III} and K_e Stress Intensity Factor Values along the Crack Front
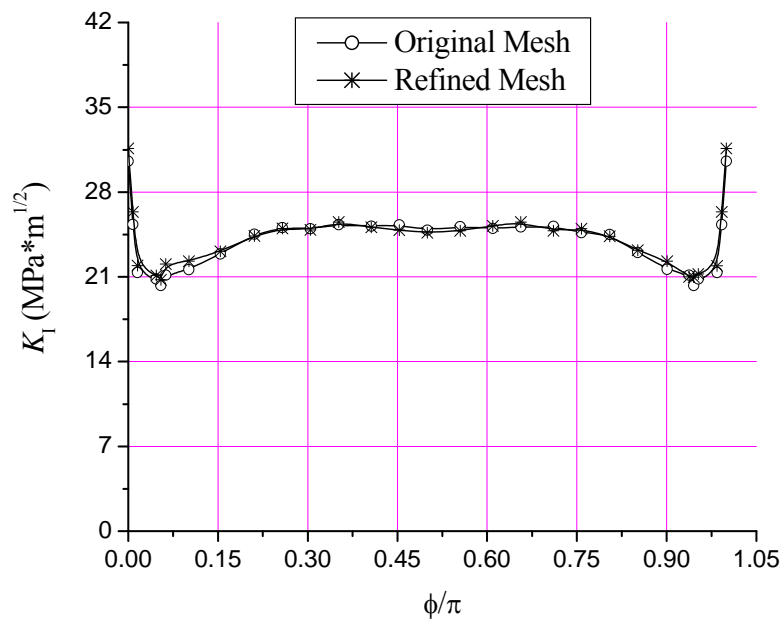
Figure 5. Convergence Test Results for the K-joint
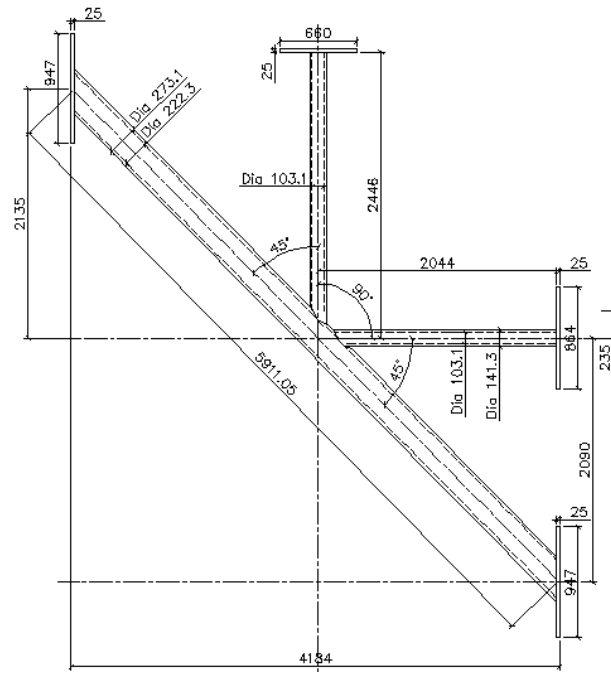
Figure 6. A Full-scale K-joint Specimen
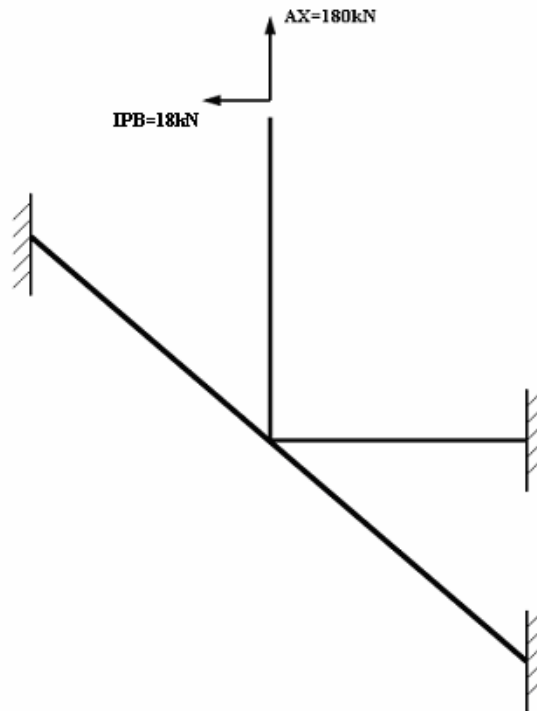
Figure 7. Load Cases and Boundary Conditions of the K-joint
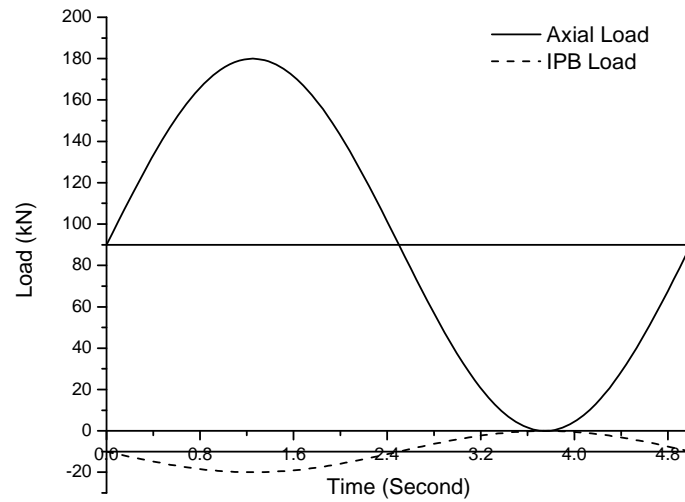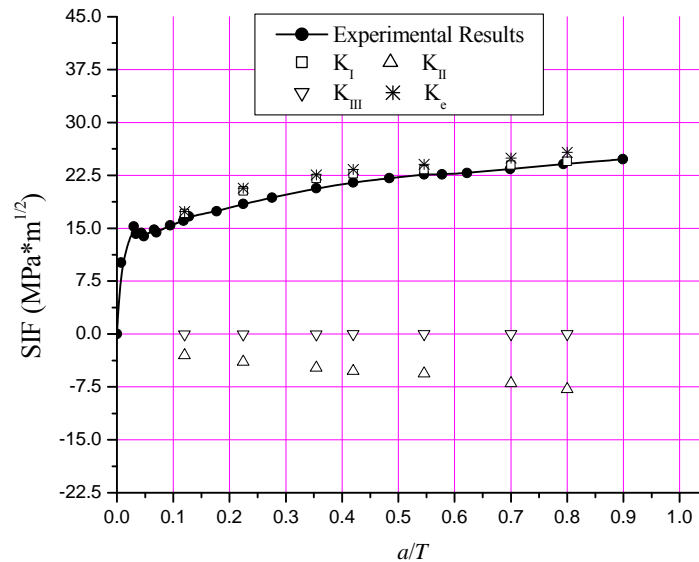
Figure 8. The Cyclic Loads applied in the Fatigue Test

Figure 9. Comparison of the Stress Intensity Factors between Numerical and Experimental Results

For the past decades, several alternative methods have been used to estimate the stress intensity factors of a semi-elliptical surface crack in tubular K-joints. Thorpe [8] proposed an equation to predict the stress intensity factors of tubular joints by averaging the surface stress at the crack position over the crack length and simplifying the through-wall stress distribution into membrane and bending components. Haswell and Hopkins [9] and Myers [10] evaluated this model and found that this model generally over-predicts the stress intensity factors for all crack depths. Haswell and Hopkins [9] concluded that it was due to not including the geometry dependent compliance effects in the model. To avoid this over-prediction, other researchers (Burderkin et al. [11], Bowness and Lee [12]) proposed another correction factor called M_k, the weld toe correction factor used to modify the flat plate model. Subsequently, Bowness and Lee [13] extended this method by including several correction factors, and later Lee and Bowness [14] proposed the model by representing it as a single parametric equation. This so-called indirect method is a very convenient method to use for estimating the stress intensity factor of a semi-elliptical surface crack in any tubular joint. This method has been

adopted in the BS7910-Amendment 1 [15] codes of practice several years ago.

In this study, a total of 1024 models of cracked tubular K-joints covering a wide range of geometrical parameters and crack shapes are analyzed again using both the direct and indirect methods. The influence the geometrical parameters on the stress intensity factors at the deepest point as well as at the crack ends are investigated, and the modification factor *Y* values which takes into account of joint geometry, crack size and loading cases, are then compared directly using both methods.

2.   TUBULAR K-JOINT CONFIGURATIONS

For brevity in design and analysis, the geometry of a typical tubular K-joint can be simplified by expressing it as dimensionless parameters. Figure 10 shows the definition of these notations of geometrical parameters which are commonly used in practice. Hence, the characteristics of a K-joint can be described by normalized parameters, such as α, β, γ and τ, and other parameters such as intersecting angle, θ, and eccentricity, *e*. Using this method, the joints having the same parameters of α, β, γ, τ, θ and *e* will be defined as the same model even though they have different diameters, thicknesses and lengths. Even if the joints have different scales, the numerical results will be the same for the same normalized parameters used in the analysis. This has been proved indispensable in generalizing results from one situation to another, and in scaling up the results of the scaled model tests (Marshall [16]).
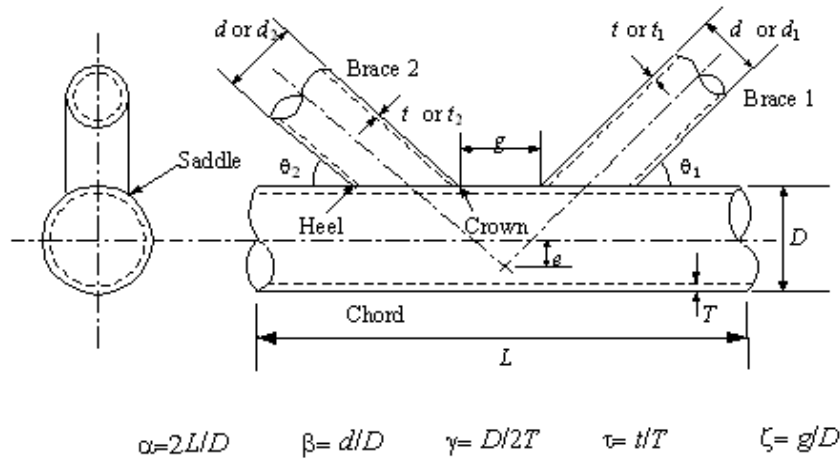
Figure 10. Notations of Geometrical Parameters in a Tubular K-joint

In practice, tubular K-joints are predominantly subjected to balanced axial loads as shown in Figure 11 where tension load is applied at the end of one brace member and compression load is applied at the end of the other brace member. When the intersecting angles, θ_1 and θ_2 between the chord and the two braces are equal, the tension and compression loads are equal in magnitude. For a tubular K-joint subjected to the balanced axial loads, the nominal stress is defined as

$$\sigma_n = \frac{4F}{(\pi[d^2 - (d-2t)^2])} \tag{1}$$

where *d* and *t* are the diameter and the thickness of the brace member respectively.
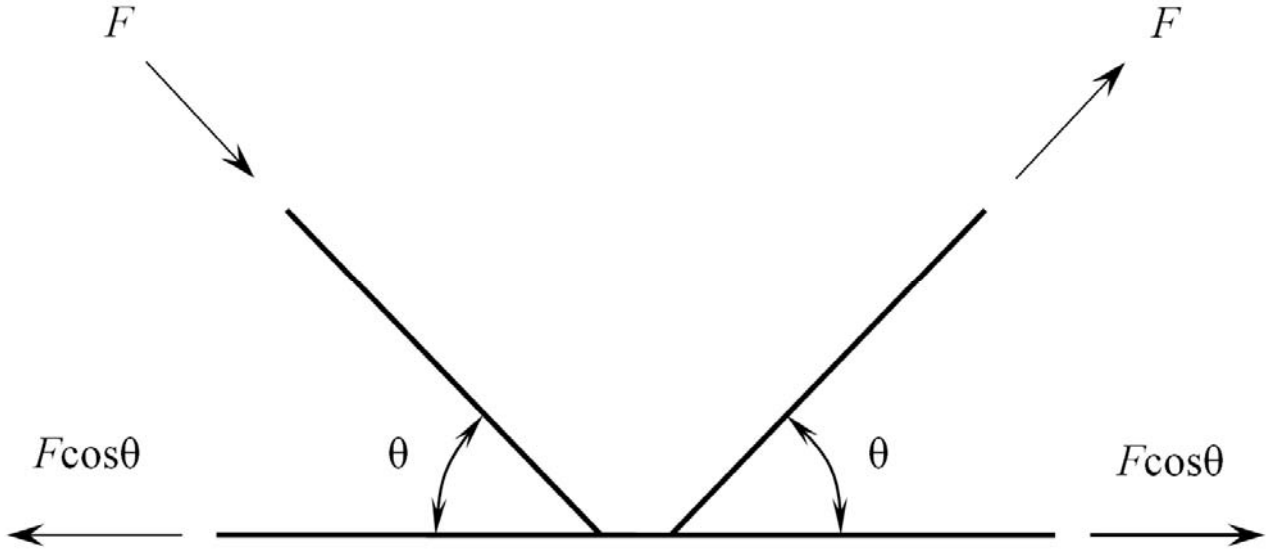
Figure 11. A Tubular K-joint subjected to Balanced Axial Loads

The general method to predict the stress intensity factor of a surface crack in any tubular joint is to provide a parametric equation. The most frequently used general parametric equation is given by

$$K = Y\sigma_{nom}\sqrt{\pi a} \tag{2}$$

where σ_{nom} is the nominal stress and a is the depth of a surface crack. Y is called a modification factor, the non-dimensional K, which takes into account for the influence of the specimen geometry, crack profile and loading conditions.

Generally, the modification factor Y is a function of joint geometry, crack size and structural restraints. Chong Rhee et al. [17] decomposed Y into three factors as follows:

$$Y = Y_g Y_s Y_i \tag{3}$$

where Y_g is the joint geometry factor which considers the effects of β, γ and τ, Y_s is the crack size factor which considers the effects of a/T where T is the chord thickness, and c/a where c is the half crack length, and Y_i is the joint and the crack coupling factor. Huang [18] added another factor Y_θ in his study, and this factor reflects the effect of the intersecting angle θ. The complete modification factor can then be expressed as

$$Y = Y_g Y_s Y_i Y_\theta \tag{4}$$

The influence of loading conditions on the stress intensity factors is taken care in the nominal stress, σ_{nom}.

Based on the effectiveness and accuracy of the generated models discussed earlier, a parametric study of 1024 numerical models is carried out in this study. In the study, the K-joints are subjected to balanced axial loads only, and the range of geometrical parameters used in the finite element analyses is tabulated in Table 1.

Table 1. Range of Geometrical Parameters of the K-joint Models

γ	τ	θ_1	θ_2	c/a	a/T	β
12, 18,	0.25, 0.5,	45°	45°	5, 6,	0.1, 0.3,	0.3, 0.4,
24, 30	0.75, 1.0	45°	45°	7, 8	0.5, 0.7	0.5, 0.6

3.   LEE AND BOWNESS (2001) EQUATION

In the standard crack handbooks, there are no explicit SIF solutions for any tubular joint including the K-joint. This is mainly due to the complexity of the geometry and loading conditions of any tubular joint containing a surface crack. Although many attempts have been made in the past decades to model fatigue performance of cracked tubular joints by using a variety of methods; there is still no accepted benchmark solution which can be used for comparison purposes. To date, a technique of using a flat plate model with relevant correction factors is still being used by many researchers. It is based on the SIF solutions of plain plate of Newman and Raju [19] with correction factors embedded into the equation (Bowness and Lee [13], Lee and Bowness [14]). These factors consider the effects of the geometry, the weld size and the load cases. This so-called indirect method is easy to apply because it is based on a flat plate solution, and there is no need to model the complex 3D surface crack in the tubular joints. However, one of the major drawbacks is that it can not accurately capture the load shedding present in the tubular joints. Furthermore, the fatigue crack propagation behaviour in a real tubular joint (Huang [18]) is known to be significantly different from that of a similar defect in a flat plate due to different structural restraint conditions.

3.1   Flat Plate Models

A flat plate model is based on the stress intensity factor of a surface crack in a finite plate subjected to tension and bending loads (Newman and Raju [19]). The empirical equation is given as follow:

$$K = \left(S_t + HS_b\right)\sqrt{\frac{\pi a}{Q}}\, F\left(\frac{a}{t}, \frac{a}{c}, \frac{c}{b}, \phi\right)$$

(5)

where K is Mode-I stress intensity factor, S_t is the tension stress in the plate, H is a correction factor, S_b is the bending stress on the plate surface, Q is the shape factor for semi-elliptical defect, F is the plain plate geometric factor, a is the crack depth, t is the plate thickness, c is the crack half width, b is the plate width, and ϕ is the elliptical integral. The expressions of H, Q and F can be found in paper by Newman and Raju [19].

Based on Eq. 5, Thorpe [8] proposed an equation to predict the stress intensity factors of tubular joints by averaging the surface stress at the crack position over the crack length and simplifying the through-wall stress distribution into membrane and bending components. This equation is given in the form of

$$K = \left(M_m \sigma_m + M_b \sigma_b \right) \sqrt{\frac{\pi a}{Q}} \tag{6}$$

where K is the Mode-I intensity factor, M_m and M_b are the plain plate shape factors for tension and bending respectively, σ_m and σ_b are the membrane and bending stresses respectively. Haswell and Hopkins [9] and Myers [10] evaluated this model and found that this model generally over-predicts the stress intensity factors for all crack depths. Haswell and Hopkins [9] concluded that it was due to not including the geometry dependent compliance effects in the model.

To avoid this over-prediction, some earlier researchers (Burdekin et al. [11]; Bowness and Lee [20]) proposed another correction factor which is called M_k, the weld toe correction factor. This factor is defined as

$$M_k = \frac{K_{\text{in plate with attachment}}}{K_{\text{in same plate but with no attachment}}} \tag{7}$$

The expression of M_k was given by Burdekin et al. [11] and Bowness and Lee [12].

After introducing the weld toe magnification factor M_k into the equation, the stress intensity factors of any tubular joint can be expressed in the following form as

$$K = \left(M_{km} M_m \sigma_m + M_{kb} M_b \sigma_b \right) \sqrt{\frac{\pi a}{Q}} \tag{8}$$

Subsequently, Lee and Bowness [14] approximated Eq. 8 as follow:

$$K \approx (M_{km} M_m \text{SCF} \times (1 - \text{DOB}) + M_{kb} M_b \text{SCF} \times \text{DOB}) \, \sigma_{nom} \sqrt{\pi a} \tag{9}$$

where a is the crack depth, M_k is the weld toe magnification factors, M is the plain plate shape factor, and the subscripts m and b denote membrane and bending load respectively. SCF is the stress concentration factor and DOB is the degree of bending at the would-be location of the crack, and σ_{nom} is the nominal stress in the reference brace of the joint.

As DOB, SCF and σ_{nom} are all obtained from uncracked tubular joints, and M_{kj}, M_j (j=m,b) can be calculated from parametric equations, it is clear that Eq. 9 is a very convenient method to use for estimating the stress intensity factors of any tubular K-joint because it avoids the complexity of generating the mesh of the surface crack. However, the actual surface crack along the weld in a tubular K-joint is shown to be a double-curved in shape (Bowness and Lee [20]), and the geometry of the intersecting curve has an influence on the stress intensity factor values. Another point is that the stress distribution along the weld toe is completely different from the stress distribution of a surface crack in a plain plate. As a result, the stress distribution will influence the stress intensity factors, and hence the crack propagation rate of the K-joint.

Up to now, Eq. 9 is still being used by researchers to estimate the stress intensity factors of a surface crack in any tubular joint. In practice, it is convenient to use, but its accuracy and reliability has not been validated experimentally for the tubular K-joint.

3.2   Calculation of SCF, DOB, M_k and M

Eq. 9 is based on the analysis of the SCF and DOB values in uncracked tubular joints. Extensive research works on SCFs for tubular joint under axial load, in-plane bending and out-of-plane bending has been carried out in the past decades. Numerous SCF equations were proposed by many researchers (Efthymiou and Durkin [21], Smedley and Fisher [22]). Zhao et al. [23] has published a design guide for estimating SCF values using equations and design charts. The design guide covers all typical joint configurations used in practice such as the T-joint, Y-joint and K-joint. Morgan and Lee [24] also proposed parametric equations to estimate the SCF values of the tubular K-joint.

All of the above equations can only predict the maximum SCF or SCFs at specific limited locations around the outer surface of the weld. For K-joints subjected to certain load cases, the SCF of the outer surface is usually different from the SCF of the inner surface of the chord. To solve this problem, Lee and Morgan [25] proposed a concept of degree of bending (DOB) which can be determined from the inner and outer surface stresses. Lee and Morgan [25] had also published their results based on the computation of SCFs for K-joints under axial load and in-plane bending. In order to simplify the determination of the membrane stress and bending stress, Lee and Bowness [26] proposed a concept of degree of bending (DOB). In Eq. 9, DOB is a parameter to measure the degree of bending of tubular joints, and it is defined as

$$\text{DOB} = \frac{\sigma_b}{\sigma_m + \sigma_b} = 1 - \frac{1}{2}\frac{\text{SCF}_{\text{inner}}}{\text{SCF}_{\text{outer}}} \tag{10}$$

where σ_b and σ_m are bending stress and membrane stress respectively. $\text{SCF}_{\text{inner}}$ and $\text{SCF}_{\text{outer}}$ are SCFs on the inner and outer surfaces of the chord. The same parametric equations of SCF and DOB are used in this study. Since the crack is symmetrical with respect to the crown, the crown SCF parametric equation is used for the crack deepest point. For the crack ends of the free surface which can be located anywhere along the weld toe, there is no specific SCF parametric equation that can be used in practice. In this paper, the crown SCF parametric equation is also used to calculate the Y values of the crack tips. For the DOB, the same strategy is applied in this study.

Parametric equation of M_{kj} (j=m,b) are available in the literature (Bowness and Lee [20]), while parametric equation of M_j (j=m,b) can be found in the other literature (Newman and Raju [19]) or from Eq. 5.

4.   DIRECT AND INDIRECT METHODS

The stress intensity factors of a surface crack in a tubular K-joint are obtained directly from the generated model used in this study. In order to assess the accuracy of Eq. 9, the stress intensity factor values at the deepest point and at the crack ends of the surface cracks are calculated using both the direct and indirect methods. The two sets of results are tabulated in Table 2 together with the experimental results. It appears that Eq. 9 always produces higher estimated values. Hence, Eq. 9 is very safe and conservative.

As mentioned previously, the stress intensity factor of the surface crack in a tubular K-joint can be expressed as

$$K = Y\sigma_{nom}\sqrt{\pi a} \tag{11}$$

where Y is a modification factor, a is the depth of a surface crack and σ_{nom} is the nominal stress.

In the assessment of the stress intensity factor, Y is called the modification factor. According to Eq. 9, the expression of Y can be written as

$$Y = M_{km}M_m\text{SCF} \times (1 - \text{DOB}) + M_{kb}M_b\text{SCF} \times \text{DOB} \tag{12}$$

Table 2. Comparison of SIF Values at the Deepest Point of a K-joint Specimen

a/T	SIF (MPa.m$^{1/2}$)		
	J-integral	Equation (9)	Experimental Results
0.12	17.36	23.45	16.32
0.22	20.69	26.34	18.44
0.35	22.58	27.56	20.66
0.42	23.33	28.74	21.49
0.55	24.05	30.12	22.62
0.71	24.97	31.22	23.71
0.82	25.74	31.81	24.54

In the analysis, Y can be obtained directly by using the stress intensity factor values divided by $\sigma_{nom}\sqrt{\pi a}$. The two sets of Y values can then be compared directly. In the parametric study, 1024 models with different geometrical parameters and crack shapes shown in Table 1 have been analyzed again. The numerical results of these models are used to assess the accuracy of the direct and indirect methods in this study.

4.1   Effect of Geometrical Parameters on Y

The first geometrical parameter to be investigated is γ which is a ratio of chord radius to chord thickness. From Figs. 12(a) and 12(b), it can be seen that Y increases gradually as γ increases by keeping the other parameters of c/a, a/T and β constant. However, the actual Y values obtained from the present study are much smaller than the corresponding values obtained from Eq. 12. This means that Eq. 12 produces relatively conservative estimation of stress intensity factor values. The trends of the graphs are consistent and reasonable. Figs. 13(a) and 13(b) show the relationship between Y and β which is a ratio of brace diameter to chord diameter, while keeping the other parameters c/a, τ and γ constant. It can be found that the trends of the graphs are consistent at the deepest, but different at the crack ends. In fact, Y has an inverse tendency at the crack ends as β increases for the direct and indirect method. The effect of parameter τ on the Y is illustrated in Figs. 14(a) and 14(b). It is clear that as τ increases Y increases too. The trends of the graphs are the same at both the deepest point and crack ends.
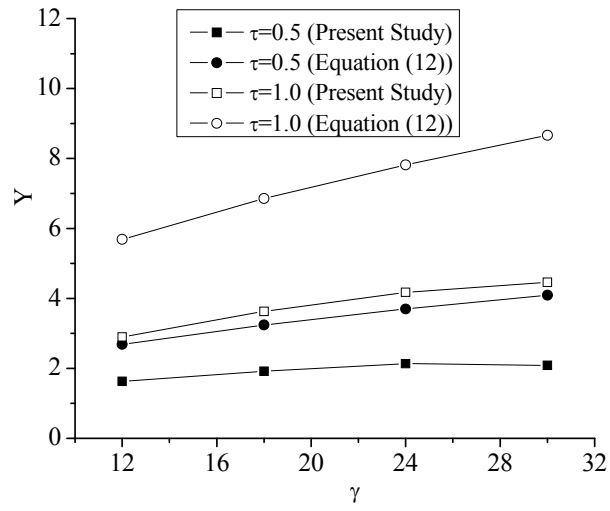
(a) at the deepest point
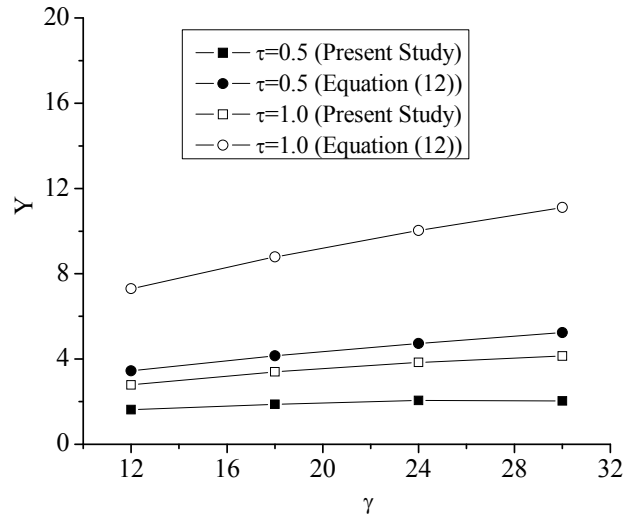
(b) at the crack ends

Figure 12. Effect of γ on *Y* (*c*/*a*=5, *a*/*T*=0.1, β=0.3)
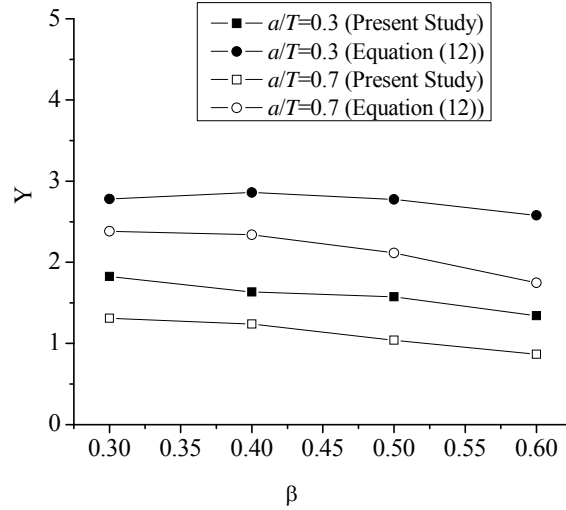
(a) at the deepest point
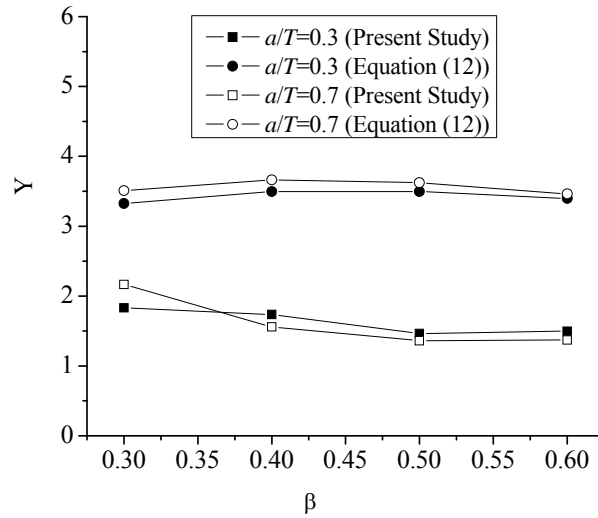
(b) at the crack ends

Figure 13. Effect of β on Y ($\gamma=18$, $\tau=0.5$, $c/a=6$)

4.2   Effects of Crack Shapes on Y

The effects of the crack shape on Y are illustrated in Figs. 15(a), 15(b), 16(a) and 16(b). Generally, Y decreases as a/T increases at the deepest point. Both methods produce the same conclusions. When β is small, Y decreases initially and then increases as a/T increases. But when β is large, Y increases as a/T increases. Hence, the trend of Y is not distinct at the crack ends. The effect of c/a on Y is the opposite. When c/a becomes larger, Y increases at the deepest point and slightly decreases at the crack ends. It should be noted that the series of solid circle almost coincides with the series of the blank circle in Fig. 16(b) when β is equal to 0.3. The effects of the crack shape on Y values can then be generalized as: for a deeper crack, Y at the deepest point is smaller and Y at the crack ends is larger; for a shallow and longer crack, Y at the deepest point is bigger and its value at the crack ends is smaller.

From these results, it can be seen that both direct and indirect methods can provide the same prediction of the effects of the crack shapes on the Y values at the deepest point, but very poor prediction are obtained at the crack ends. This may be because the crown SCF and DOB equations are used for the crack ends as the crack ends SCF and DOB equations are not readily available in the literature.
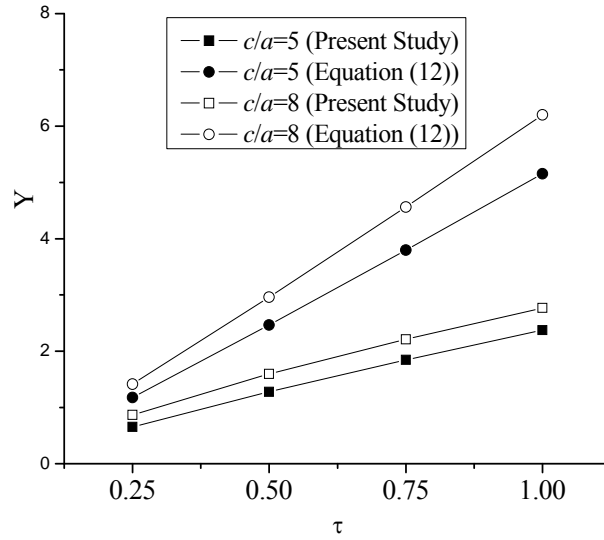
(a) at the deepest point
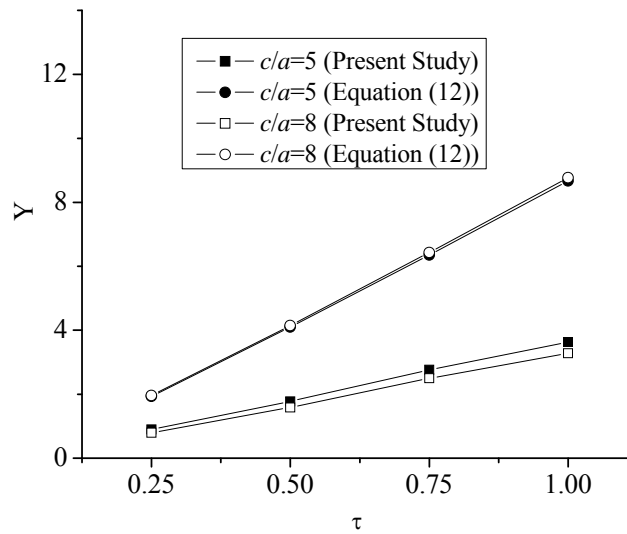
(b) at the crack ends

Figure 14. Effect of τ on Y (γ=24, a/T=0.5, β=6)
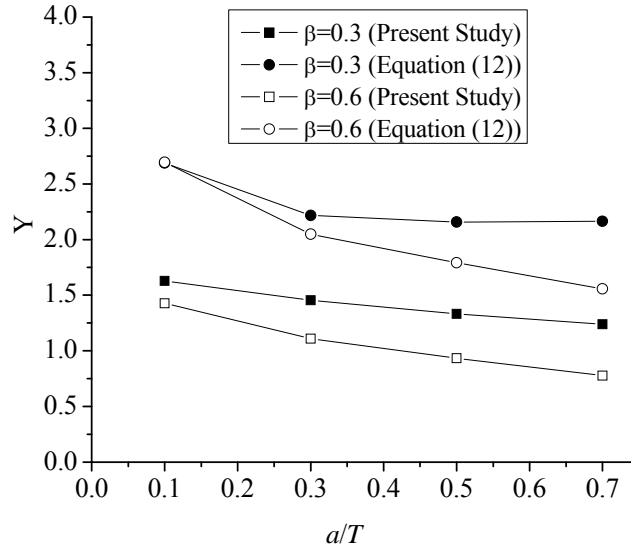
(a) at the deepest point
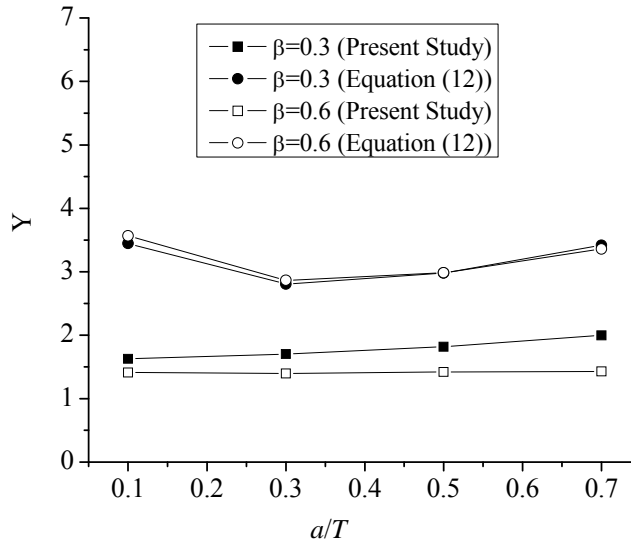
(b) at the crack ends

Figure 15. Effect of a/T on Y (γ=12, τ=0.5, c/a=5)

4.3   **Error Estimation Analysis**

To validate the accuracy of the Eq. 12, a comparison is carried out between the direct and indirect method results. An equation of relative error is introduced and defined as

$$\text{Relative Error} = \frac{Y_{\text{Equation}} - Y_{\text{FE}}}{Y_{\text{FE}}} \times 100\% \qquad (13)$$

where Y_{Equation} is the modification factor calculated using indirect method, and Y_{FE} is the modification calculated using direct method. Figure 17 shows the comparison results. From Figure 17, it can be seen that the Y_{Equation} calculated using the Eq. 12 is very conservative; it overestimates the stress intensity factor values by as much as 190.4% (β=0.5, γ=30, τ=0.5, a/T=0.1, c/a=5) at the deepest point, and 390.7% (β=0.4, γ=30, τ=0.5, a/T=0.5, c/a=8) at the crack ends of the surface crack respectively.
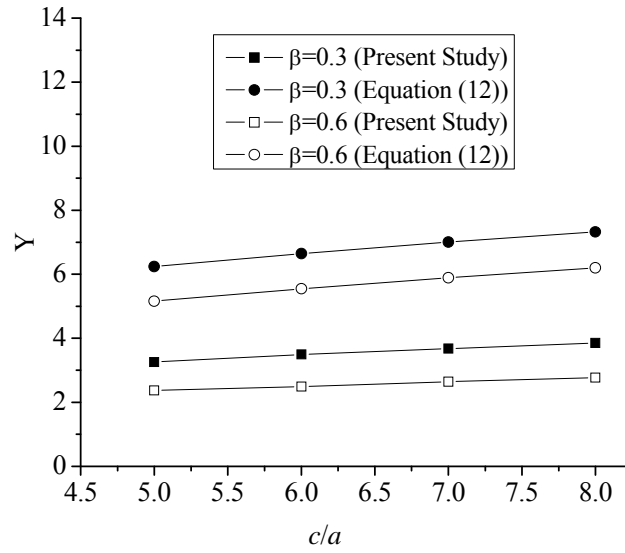
(a) at the deepest point
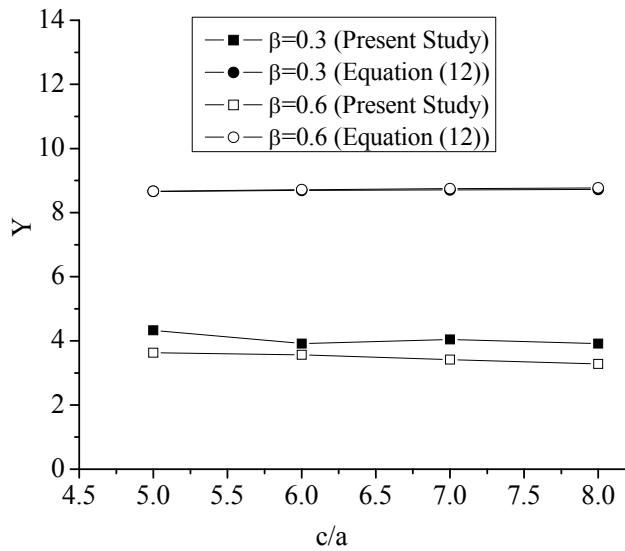
(b) at the crack ends

Figure 16. Effect of c/a on Y (γ=24, τ=1.0, a/T=0.5)
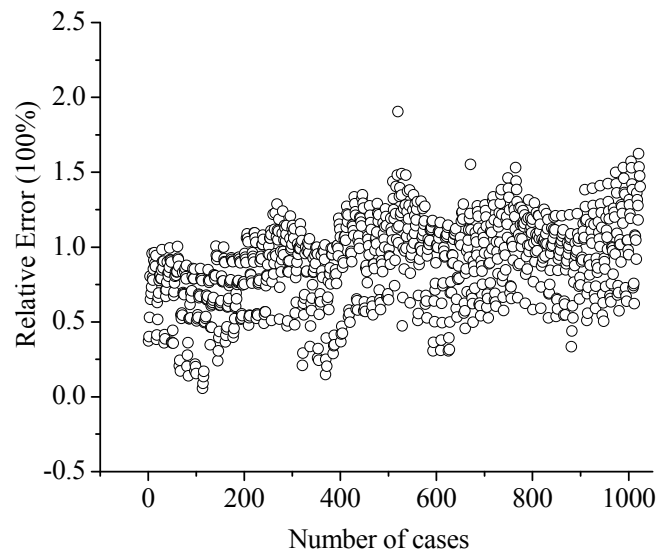
(a) at the deepest point
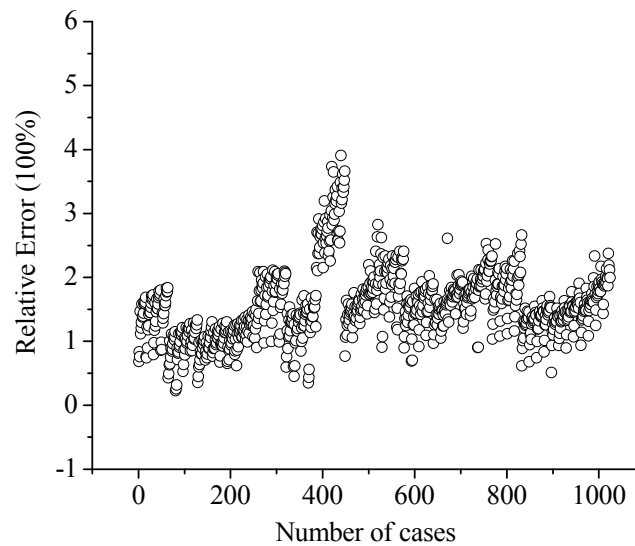
(b) at the crack ends

Figure 17. Error Analysis of Numerical Models

5.   CONCLUSIONS

A numerical model of a tubular K-joint containing a semi-elliptical surface crack has been presented and described briefly in this paper. The surface crack is modeled explicitly in the cracked joint. It is shown that the direct method can produce accurate stress intensity factors at the deepest point and also at the crack ends of the surface crack. In the indirect method, a T-butt solution used in conjunction with the stress concentration factors (SCFs) and degree of bending (DOB) is used to estimate the stress intensity factor values at the deepest point and also at the crack ends. The accuracy of both methods is assessed by comparing the modification factor *Y* values. From the parametric study of 1024 models, it is concluded that both the direct method and the indirect method can produce safe estimation of stress intensity factor values of a surface crack in a tubular K-joint. However, the

indirect method is very conservative, and it overestimates the stress intensity factor values by as much as 190.4% (β=0.5, γ=30, τ=0.5, a/T=0.1, c/a=5) at the deepest point, and 390.7% (β=0.4, γ=30, τ=0.5, a/T=0.5, c/a=8) at the crack ends of the surface crack respectively.

Nomenclatures

a	crack depth
b	plate width
c	half crack length
DOB	degree of bending
d	brace diameter
D	chord diameter
e	eccentricity
F	axial load
g	gap distance
H	correction factor
J	J-integral
K_I	Mode-I stress intensity factor
K_{II}	Mode-II stress intensity factor
K_{III}	Mode-III stress intensity factor
K_e	effective stress intensity factor
L	chord length
M_m	plain plate shape factor for tension
M_b	plain plate shape factor for bending
M_k	weld toe correction factor
M_{km}	weld toe correction factor due to membrane stress
M_{kb}	weld toe correction factor due to bending stress
N	number of cycles
Q	shape factor
r	brace radius
R	chord radius
SCF	stress concentration factor
SCF_{inner}	SCF on the inner surface of the chord
SCF_{outer}	SCF on the outer surface of the chord
S_b	bending stress in the plate
S_t	tension stress in the plate
t	plate thickness
T	chord thickness
Y	modification factor
Y_g	joint geometry factor
Y_s	crack size factor
Y_i	joint and crack coupling factor
Y_θ	intersecting angle factor
α	a ratio of $2L/D$
β	a ratio of d/D
γ	a ratio of $D/2T$
θ	intersecting angle between brace and chord
σ_{nom}	nominal stress
σ_m	membrane stress
σ_b	bending stress

τ	a ratio of t/T
ϕ	elliptical integral
Y_{Equation}	modification factor calculated using indirect method
Y_{FE}	modification factor calculated using direct method

REFERENCES

[1]   Cao, J.J., Yang, G.J. and Packer, J.A., "FE Mesh Generation for Circular Joints with or without Cracks", Proceeding of the 7th International Offshore and Polar Engineering Conference (ISOPE), USA, 1997, pp. 53-58.

[2]   Bowness, D. and Lee, M.M.K., "The Development of an Accurate Model for the Fatigue Assessment of Doubly Curved Cracks in Tubular Joints", International Journal of Fracture, 1995, Vol. 73, pp. 129-47.

[3]   Lie, S.T., Lee, C.K., Chiew, S.P. and Shao, Y.B., "Estimation of Stress Intensity Factors of Weld Toe Surface Cracks in Tubular K-Joints", 10th International Symposium on Tubular Structures, Madrid, Spain, 2003, pp. 347-355.

[4]   Lie, S.T., Lee, C.K., Chiew, S.P. and Shao, Y.B., "Mesh Modelling and Analysis of Cracked Uni-planar Tubular K-joints", Journal of Constructional Steel Research, 2005, Vol. 61, No. 2, pp. 235-264.

[5]   Shao, Y.B. and Lie, S.T., "Parametric Equation of Stress Intensity Factor for Tubular K-joint under Balanced Axial Loads", International Journal of Fatigue, 2005, Vol. 26, No. 6, pp. 666-679.

[6]   Shao, Y.B., Lie, S.T. and Chiew, S.P., "Effect of Chord Length Ratio of Tubular Joints on Stress Concentration at Weld Region", Proceedings of the 12th International Symposium on Tubular Structures, Shanghai, China, 2008, pp. 375-379.

[7]   Lie, S.T., Chiew, S.P., Lee, C.K. and Shao, Y.B., "Validation of a Surface Crack Stress Intensity Factors of a Tubular K-joint", International Journal of Pressure Vessels and Piping, 2005, Vol. 82, No. 8, pp. 610-617.

[8]   Thorpe, T.W., "A Simple Model of Fatigue Crack Growth in Welded Joints", Offshore Technology Report, 1986, OTH 86 255.

[9]   Haswell, J. and Hopkins, P., "A Review of Fracture Mechanics Models of Tubular Joints", Fatigue and Fracture of Engineering Materials and Structures, 1991, Vol. 14, No. 5, pp. 483-497.

[10]   Myers, P.T., "Corrosion Fatigue and Fracture Mechanics of High Strength Jack Up Steels", Ph.D. Thesis, University College London, London, UK, 1998.

[11]   Burdekin, F.M., Chu, W.H., Chan, W.T.W. and Manteghi, S., "Fracture Mechanics Analysis of Fatigue Crack Propagation in Tubular Joints", International Conference on Fatigue and Crack Growth in Offshore Structures, London, UK, 1986.

[12]   Bowness, D. and Lee, M.M.K., "Stress Intensity Factor Solutions for Semi-elliptical Weld-toe Cracks in T-butt Geometries", Fatigue and Fracture of Engineering Materials and Structures, 1996, Vol. 19, No. 6, pp. 787-797.

[13]   Bowness, D. and Lee, M.M.K., "Prediction of Weld Toe Magnification Factors for Semi-elliptical Cracks in T-butt Joint", International Journal of Fatigue, 2000, Vol. 22, No. 5, pp. 369-387.

[14]   Lee, M.M.K. and Bowness, D., "Prediction of Stress Intensity Factors in Semi-elliptical Weld Toe Cracks in Offshore Tubular Joints", Proceedings of the 9th International Symposium on Tubular Structures, Dusseldorf, Germany, 2001, pp. 299-308.

[15]   BS7910-Amendment 1, "Guide to Methods for Assessing the Acceptability of Flaws in Metallic Structures", British Standard Institution, London, UK, 2005.

[16] Marshall, P.W., "Design of Welded Tubular Connections: Basis and Use of AWS Code Provisions", Elsevier Science Publishers, Amsterdam, The Netherlands, 1992.

[17] Chong, R.H., Han, S. and Gipson, G.S., "Reliability of Solution Method and Empirical Formulas of Stress Intensity Factors for Weld Toe Cracks of Tubular Joints", Proceedings of the 10th Offshore Mechanics and Arctic Engineering Conference, ASME, 1991, Vol. 3(B), pp. 441-452.

[18] Huang, Z.W., "Stress Intensity Factor of Cracked Steel Tubular T and Y-joints under Complex Loads", Ph.D. Thesis, Nanyang Technological University, Singapore, 2002.

[19] Newman, J.C. and Raju, I.S., "An empirical Stress Intensity Factors Equation for the Surface Crack", Engineering Fracture Mechanics, 1981, Vol. 15, No. 2, pp. 185-192.

[20] Bowness, D. and Lee, M.M.K., "Fatigue Crack Curvature under the Weld Toe in an Offshore Tubular Joint", International Journal of Fatigue, 1998, Vol. 20, No. 6, pp. 481-490.

[21] Efthymiou, M. and Durkin, S., "Stress Concentrations in T/Y and gap/overlap K-joints. Proceedings Conference on Behaviour of Offshore Structures, Delft, Elsevier Science Publishers, Amsterdam, The Netherlands, 1985, pp. 429-440.

[22] Smedley, P. and Fisher, P., "Stress concentration Factors for Simple Tubular Joints", Proceedings of the 1st International Offshore and Polar Engineering Conference, International Society of Offshore and Polar Engineers, Edinburgh, UK, 1991, pp. 475-483.

[23] Zhao, X.L., Herion, S., Packer, J.A., Puthli, R., Sedlacek, G., Wardenier, J., Weynand, K., van Wingerde, A. and Yeomans, N., "Design Guide for Circular and Rectangular Hollow Section Joints under Fatigue Loading. CIDECT Publication No. 8, TUV-Verlag, Germany, 2000.

[24] Morgan, M.R. and Lee, M.M.K., "Prediction of Stress Concentration Factors in K-joints under Balanced Axial Loading", Proceedings of the 7th International Symposium on Tubular Structures, Hungary, 1996, pp. 301-308.

[25] Lee, M.M.K. and Morgan, M,R., "Prediction of Stress Concentration Factors in On-plane Moment Loaded Tubular K-joints", Proceedings of the 8th International Symposium on Tubular Structures, Singapore, 1998, pp. 305-314.

[26] Lee, M.M.K. and Bowness, D., "Factors Affecting the Fracture Mechanics Assessment of a Cracked Offshore Tubular Joint", Proceedings of the 8th International Symposium on Tubular Structures, Singapore, 1998, pp. 353-359.

CONSTRUCTION SEQUENCE SIMULATION OF A PRACTICAL SUSPEN-DOME IN JINAN OLYMPIC CENTER

Zhi-qiang Li[1], Zhi-hong Zhang[2,*], Shi-lin Dong[3] and Xue-yi Fu[4]

[1] Department of Building Engineering, Tongji University, Shanghai 200092, China
[2] College of Civil Engineering, Shanghai Normal University, Shanghai 200234, China
[3] Zhejiang University, Hangzhou 310027, China
[4] China Construction (Shenzhen) Design International, Shanghai 200235, China
*(Corresponding author: E-mail: zhangzh007@yahoo.com.cn)

ABSTRACT: Construction sequence simulation analysis of a practical suspen-dome of Jinan Olympic Center is discussed in the present paper. Suspen-dome is a kind of advanced large-span space structure which is composed of an upper single-layer latticed shell and a lower cable-bar system. It is also a kind of hybrid system due to a combination of cable elements, bar elements and beam elements. Construction errors and temperature fluctuation are of importance and need to be taken into consideration during the construction process. The construction error of the structure is simulated by using the random imperfection modal method. Using the integral structure model including the concrete supporting system, the effect of the temperature variation on the suspen-dome is analyzed. The construction of suspen-dome is a little complex due to the interaction between the upper single-layer latticed shell and the lower cable-bar system. The configurations of the structure during the construction could be determined by an inverse analysis method or a mixed analysis method depending on the stages adopted in each construction scheme. And the influence to the lower cable-bar system caused by the setting-up errors at nodes is studied on the basis of one feasible construction scheme. Some meaningful and universal conclusions are given out.

Keywords: Suspen-dome, Latticed shell, Cable-bar system, Hybrid space structure, Construction errors, Temperature changes, Construction sequence simulation, Inverse analysis method, Mixed analysis method

1.   INTRODUCTION

Structural design of the spherical suspen-dome with a diameter of 122m was carried out in 2006. This multi-purpose gymnasium locates in Jinan City, China. The arena has an approximate architectural area 60,000 m^2 which can accommodate more than 12,000 audiences for the local Olympic Games held in 2009. Suspen-dome with a diameter of 122m and a rise of 12.2m is chosen as the roof of this gymnasium (Figures 1 and 2). The finite element model of the upper single-layer reticulated shell consists of two-node beam element. The section of the two-node beam element is a circular thin-wall steel pipe with a diameter of 377mm, and thickness of 14mm or 16mm. A Sunflower-Kiewitt hybrid lattices is adopted for the upper spherical single-layer reticulated shell. Three hoops of cable-bars of Geiger type are adopted as the lower tensile system. Details of some typical joints are shown in Figures 3 to 5, such as support joint on the ring beam and two types of cable-struts joints.

Suspen-dome could be regarded as a cable-dome with the ridge cables substituted by a single-layer latticed shell. Compared to cable dome, suspen-dome is more rigid and can resist greater external loads. Further more, suspen-dome usually has a better flexibility to boundary conditions than cable dome. The structure is a kind of advanced hybrid space structures composed of beam elements, bar elements and cable elements [1]. The suspen-dome with a diameter of 122m of the gymnasium of Jinan Olympic Center is the largest in the world at present. A rise to span ratio of less than 0.15 is recommended by Kitipornchai [2].

Recent work mostly focuses on the structural properties of the suspen-dome and the design of pre-tension. The static and dynamic properties of the suspen-dome are enhanced compared with the corresponding single-layer latticed shell [3]. Parametric analyses of the factors affect the buckling

carrying capacity of the structure have been conducted. Also some design methods of pre-tension have been discussed by many researchers [4]. Unfortunately, the construction sequence simulation analysis has not been adequately investigated. More than ten suspen-dome roofs have been fabricated in the world especially in Asia. However, construction sequence simulation of cable-strut systems may be beneficial to the suspen-dome for the existence of the lower cable-bar system is to stiffen the upper single-layer latticed shell. Only implementing pre-tension to the diagonal cables, only implementing pre-tension to the hoop cables and only adjusting the length of struts are three basic methods for the construction of cable-dome [5]. But there are many difficulties in construction sequence simulation analysis of cable-dome for the coupling of mechanism displacement and elastic deformation during the construction. Nonlinear flexibility method was studied in the analysis of erection process of cable-dome by Luo [6]. However, it is not proper for the large-scale space structure because of the non-symmetric of the stiffness matrix. By controlling the original length of cables during the construction process, nonlinear finite element method was used to construction sequence simulation analysis of cable-dome by Shen [7]. Dynamic relaxation method was adopted to simulate the construction process of cable-struts by Zhang [8]. Because of the variation of geometry and component stress during the configuration process, it is pointed out by Chen [9] that only the equilibrium state of the structure after the completion of a construction stage should be considered. Inverse analysis method was proposed by Yuan [10] to simulate the construction of cable-domes step by step. However, the aforementioned studies are subject to the construction of cable dome but not for the suspen-dome. An experiment carried out by Li [11] confirmed that the suspen-dome could be constructed by implementing pre-tension to the hoop cables. Without consideration of the construction errors Li [12] simulated the construction process of a suspen-dome by a direct analysis method.

Construction sequence simulation analysis of suspen-dome is a little complex due to the interaction between the upper single-layer latticed shell and the lower cable-bar system. Actually, a considerably degree of error may be introduced if an inappropriate approach is applied to complete the analysis. Two kinds of simulation analysis methods are proposed in the present paper without any computational problems. The configuration of the structure during each construction step is determined by different methods depending on the construction stages being proceeded. Construction errors and temperature changes are of importance and need to be taken into consideration. On the basis of a practical suspen-dome roof of Jinan Olympic Center, the imperfection sensitivity and other factors effective are addressed. Construction errors of the structure are simulated. Random Imperfection Modal Method, in which a randomly generated imperfection samples subjected to a normal distribution, is applied. Using the integral structure model including the concrete supporting system for a more rational FEM analysis, the effect of temperature variation on the cable-bar system is investigated.

2.   FORCE FINDING ANALYSIS

The lattice of the upper single-layer reticulated shell of this practical suspen-dome is combined with the Kiewitt style inside and the Lamella style outside (Figure 1). The span of the structure is 122m with a rise-to-span ration of 1/10. The shape of the lower cable-bar system is rib-ring type. Three hoops of cable-bar system are designed to improve the structural performance. The suspen-dome is pin-jointed on the lower reinforced concrete ring beam with the perimeter nodes being restrained in all directions.
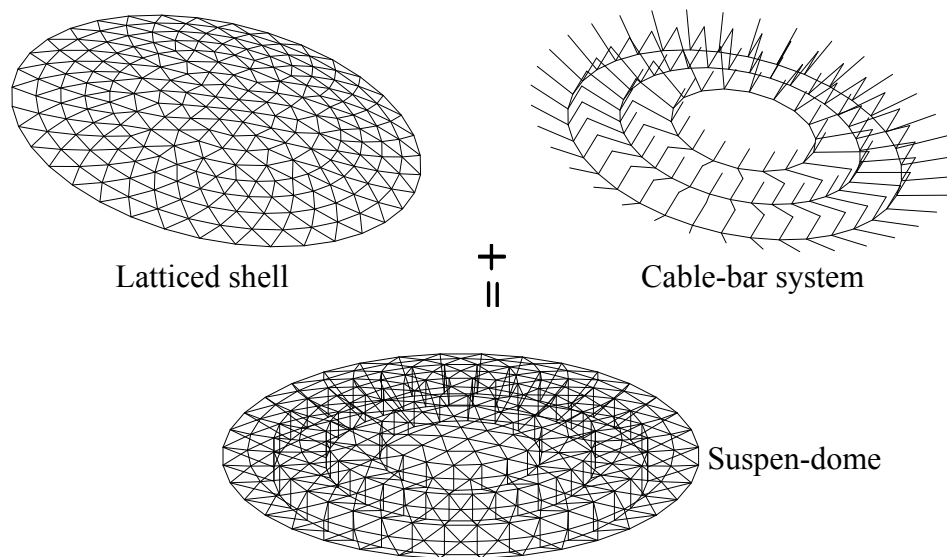
Figure 1. Suspen-dome
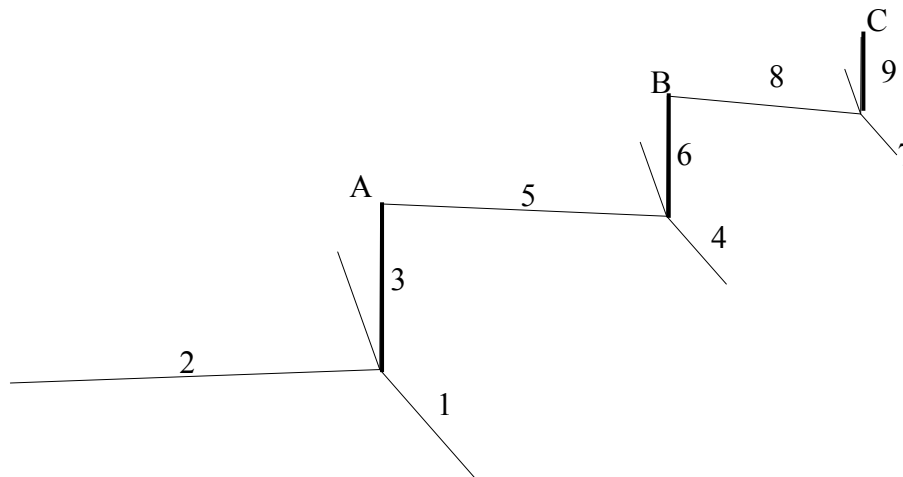
Figure 2. Group Number of Cable-struts
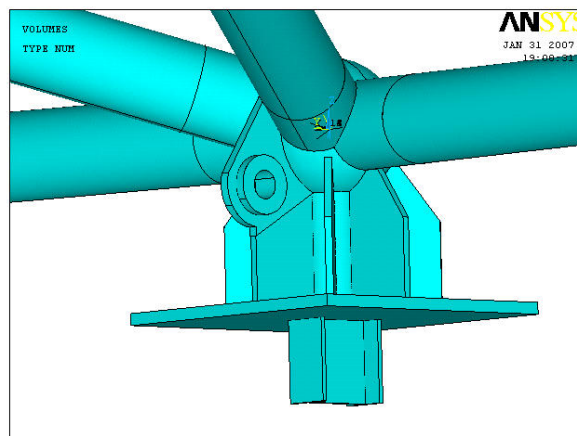
Figure 3. Support Joint
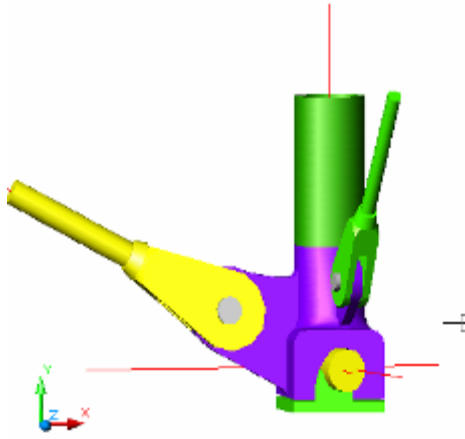
Figure 4. Cable-strut Joint   Figure 5. Cable-strut Joint
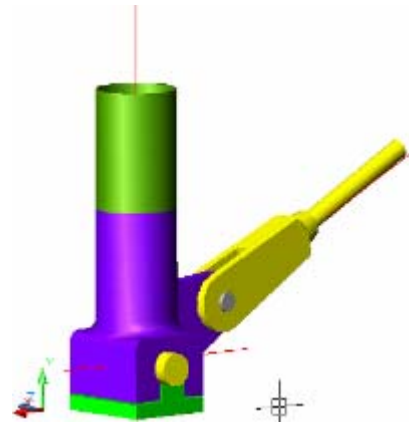
Table 1. Force Finding Analysis Results without Consideration of Self-weight (Units: kN)

Member group	Section	Pre-tension
1	Ø7X253	3.85798760E+03
2	Ø90	7.48215617E+02
3	Ø273X10	-3.27996133E+02
4	Ø5X187	1.45776145E+03
5	Ø55	2.82717311E+02
6	Ø245X10	-1.23935110E+02
7	Ø5X61	4.58668838E+02
8	Ø45	1.77230854E+02
9	Ø219X10	-7.76928916E+01

Figure 2 shows a typical frame of the lower cable-bar system. Typical nodes A, B and C are the top points of the compressive bars, and node D (not shown in Figure 2) is the central node of the upper single-layer latticed shell. The pre-tension force of the lower cable-bar system could be found according to local analysis method [13-14]. Considering to improve the structural characteristic of the upper single-layer latticed shell and to reduce the reaction force of the bearings due to a small rise-to-span ratio, the optimized pre-tension distribution is listed in Table 1.

3.   PARAMETRIC ANALYSIS OF THE SUSPEN-DOME

3.1   Boundary Conditions Effects On The Single-layer Latticed Shell

Either pin-joints or rigid-joints could be applied to be the boundary joints. But at the viewpoint of design and fabrication, structures with the boundary joints being pinned are more widely used in the actual situation for the difficulty of ideal rigid-joint assumption. The effect of different boundary conditions on the upper single-layer latticed shell is shown in Table 2. The vertical displacement at node D named U_D is almost the same under different boundary conditions. The vertical and radial horizontal reaction forces of the bearings named R_H and R_V are very close. However, the moment of the bearings could not be neglected when the suspen-dome is rigidly-jointed with ring-beam. The pin-jointed assumption is applied to the following analysis.

Table 2. The Effect of Different Supporting Conditions

	Pin-jointed	Rigid-jointed	Difference
U_D(mm)	-14.128	-14.749	4.40%
R_V(kN)	2.15E+02	2.15E+02	0.00%
R_H(kN)	4.88E+02	4.77E+02	-2.25%

3.2 Construction Errors Effects On The Single-layer Latticed Shell

A normal distribution assumption is applied to the nodal spatial position imperfection. The effect of construction errors on the single-layer latticed shell is listed in Table 3, which is investigated by random imperfection modal method. The maximum deviation ratio of the reaction force R_R is confined in approximately 5% when the maximum construction error is less than 0.15m. The vertical displacement of node D named U_D does not change too much as the maximum construction error increases.

Table 3. The Effect of Construction Errors on the Latticed Shell

Maximum error	U_D（mm）	R_R
30mm	-14.381	1.23%
60mm	-14.759	1.72%
90mm	-14.625	1.61%
120mm	-15.404	3.72%
150mm	-15.644	4.41%

3.3 The Equilibrium State of Suspen-dome Fabricated

The single-layer latticed shell is firstly installed. The suspen-dome woks without cladding/facility appended after the cable-bar system tensioned. The vertical displacement of the node D named U_D is -0.030427m. The horizontal and vertical reaction force of bearings R_H and R_V are approximately 9.78×10^5N and 2.50×10^5N respectively. With consideration of the self-weight and live load during the normal state, the axial internal-force of the cable-bar system is shown in Table 4.

Table 4. The Axial Force of Cable-bar System（Kn）

Member group	Axial force（kN）
1	3778.186
2	732.857
3	-306.308
4	1413.329
5	274.624
6	-115.922
7	449.795
8	173.747
9	-72.661

3.4   Construction Errors and Temperature Effects on - Suspen-dome

Some difference lies in the effect of construction errors and temperature variation on the suspen-dome with the boundary nodes being pin-jointed and rigidly-jointed. Without consideration of the elastic stiffness of the concrete supporting system, the effect of construction errors and temperature variation on the axial internal-force of cable-bar system is shown in Table 5 and Table 6, respectively. the effect of construction errors and temperature variation on the displacement and reaction force is listed in Table 7 and Table 8. The value of column R_μ denotes the maximum deviation ratio between the mean axial internal-force and the design pre-tension among each group of cable-bar elements. The value of column R_σ denotes the maximum deviation ratio between the axial internal-force standard deviation and the mean axial internal-force among each group of cable-bar elements. The value of column R_{RH} describes the maximum deviation ratio of the horizontal reaction force while the value of column R_{RV} is the vertical reaction force.

Table 5. Construction Error Effects on the Axial Internal-force of the Cable-bar Elements

Max error	R_σ	R_μ
30mm	1.75%	1.17%
60mm	5.05%	1.24%
90mm	9.27%	1.29%
120mm	11.42%	1.30%
150mm	18.42%	1.43%

Table 6. Temperature Variation Effects on the Axial Internal-force of the Cable-bar Elements

Temperature	R_σ	R_μ
+10℃	1.17%	-13.66%
+20℃	1.14%	-27.20%
-10℃	1.25%	13.47%
-20℃	1.29%	27.44%

Table 7. Construction Errors Effects on the Displacement and the Reaction Force

Max error	U_D（mm）	R_{RH}	R_{RV}
30mm	-30.37	1.57%	2.46%
60mm	-31.297	4.67%	5.66%
90mm	-30.933	4.90%	8.14%
120mm	-29.932	6.08%	9.08%
150mm	-28.835	7.70%	11.04%

Table 8. Temperature Variation Effects on the Displacement and the Reaction Force

Temperature	U_D（mm）	R_{RH}	R_{RV}
+10℃	-5.788	-30.13%	0.16%
+20℃	58.884	-60.00%	0.10%
-10℃	-55.14	30.54%	-0.29%
-20℃	-80.142	60.61%	0.10%

It is learned from Tables 5 to 8 that construction errors have a little effect on horizontal reaction force, but a significant effect on vertical reaction force. However, the effect of temperature variation on reaction force is on the contrary. It is also concluded that construction errors have little effect on the mean axial internal-force among each group of the cable-bar elements, but a significant effect on the standard deviation of the axial force. And the effect of temperature variation on the axial force among each group of the cable-bar elements is on the contrary. The guaranteed rate of the normal distribution between μ-σ and μ + σ is only 68.3% while between the interval (μ-3σ, μ+3σ) is 99.7%. Hence it is evident that maximum construction error should be under 0.03m for the deviation of axial force may be limited within 5.25%.

3.5 Temperature Effects Based on the Integral Structure Analysis
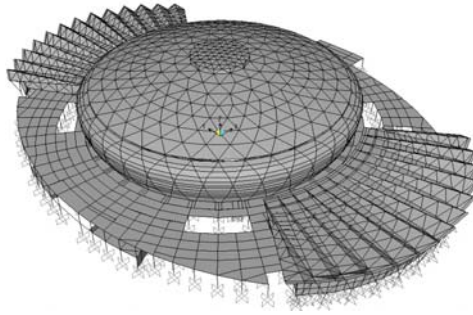
Figure 6. The Integral Model of the Gymnasium

The upper steel structure and the lower concrete supporting structure have a compatible state of deformation in real conditions. It may not be more rational to investigate the effects of temperature variation on the upper steel structure with the boundary nodes being pin-jointed without the consideration of the elastic stiffness contribution of the lower concrete supporting system. The linear thermal expansion coefficient of the concrete is very close to the steel. The effect of temperature variation on the axial force of the cable-bar element decreases while the integral structure model (Figure 6) with the lower concrete supporting system is adopted. The results are summarized in Table 9.

Table 9. Temperature Variation Effects on the Integral Model

Temperature	U_D（mm）	R_μ
+0℃	-9.306	0.00%
+10℃	-4.944	-1.50%
+20℃	-5.409	-3.00%
-10℃	-16.549	1.50%
-20℃	-23.798	3.00%

4.   CONSTRUCTION SEQUENCE SIMULATION ANALYSIS OF SUSPEN-DOME

The lower cable-bar system plays an important role in the resistance of the external loads. Implementing pre-tension to hoop cables and adjusting the length of struts could be used to complete the fabrication of suspen-dome. However, the method of implementing pre-tension to diagonal cables is used in the present paper. So the elements of group 2, group 5 and group 8 are used as actively-pre-tensioned cables.

Both mechanism and mechanical analysis must be carried out during the construction sequence simulations for the coupling of mechanism displacement and elastic deformation [14]. The configuration and the pre-tension force distribution of the suspen-dome vary with the construction process. The equilibrium state of the structure will be obtained if the configuration or the pre-tension distribution of the suspen-dome is determined during the construction.

Pre-tension contributes much to the increment of the ultimate carrying capacity of suspen-dome. It is noted that the configuration of the structure could be identified exactly as the pre-tension distribution is determined by nonlinear finite element analysis. The determination of the initial status without pre-tension is very difficult for the large degree of indeterminacy of the structure. The inverse analysis method could be applied to the identification of the configuration and the pre-tension distribution during the construction if a single-stage fabrication scheme is adopted, based on the state of the structure fabricated. Firstly, the state before the last step could be determined by killing elements fabricated at the last step. The rest may be deduced by analogy and the state of each step could be identified by killing elements fabricated at the next step. According to the inverse analysis method, the controlling parameters including the pre-tension and configuration of the structure in each construction step could be identified by removing the diagonal cables in sequence. Each equilibrium state during the construction could be determined. This method has an advantage of clear in conception and convenient in computation. And the ideal state of the structure given out byarchitects could be obtained if the inverse analysis method is applied to construction sequence simulation.

However, the inverse analysis method may result in a problem of high construction costsince the diagonal cables are tensioned for only once. Therefore, a multi-stage fabrication scheme may be necessary to reduce construction cost. And a mixed animation analysis method composed of inverse analysis firstly and direct analysis secondly with acceptable accuracy is proposed in the paper, while a multi-stages fabrication scheme is applied to the construction. The inverse analysis is used to obtain the intermediate state for purpose of decreasing the axial internal-force of cables at the first stage while the direct analysis is used to obtain the controlling state at the second stage. The mixed animation analysis method could be used in the engineering practice very well for better applicability and lower construction cost.

Three construction schemes are presented in details from Section 4.1 to Section 4.3.

4.1   Scheme 1

A single-stage fabrication scheme is adopted in this Section. Each group of diagonal cables is tensioned respectively for only one time. Tensile force at each step could be obtained in the equilibrium state by killing elements fabricated in the next step. As shown in Figure 7, the sequence of the construction in scheme 1 is as follows:

Table 10. The Variation of the Axial Force of the Cable-bar Elements (Units: kN)

Group	Step 1	Step 2	Step 3
1	0	0	3778.186
2	0	0	*732.857*
3	0	0	-306.308
4	0	712.963	1413.329
5	0	*138.862*	274.624
6	0	-55.821	-115.922
7	225.372	311.421	449.795
8	*87.236*	120.290	173.747
9	-34.559	-49.111	-72.661

Table 11. The Displacement of the Typical Nodes A, B, C and D (Units: mm)

disp	Step 1	Step 2	Step 3
U_A	-15.867524	-49.227523	4.751852
U_B	-31.966751	0.914842	8.518034
U_C	6.930325	26.713785	12.395205
U_D	-10.389931	-7.598448	-30.426954

Step 1, 50.2% of the designed pre-tension is imposed to the elements of group 8 (the inner hoop of diagonal cables);

Step 2, 50.56% of the designed pre-tension is imposed to the elements of group 5 (the middle hoop of diagonal cables);

Step 3, 100% of the designed pre-tension is imposed to the elements of group 2 (the outermost hoop of diagonal cables);

The steps of the animation analysis are opposite to the sequence of construction. Hence, the inverse analysis method is adopted. The sequences of animation analysis are presented in the following text:

Step 1, the equilibrium state of the structure and the tensile force of the actively-pre-tension cables described in the aforementioned text are obtained by killing the elements of group 2 and 5;

Step 2, the equilibrium state and the tensile force of the cables of group 5 could be identified by killing the elements of group 2;

Step 3, the equilibrium state and the tensile force of the cables of group 2 are equal to the ideal fabricated state of the structure;

The variation of the axial internal-force of the cable-bar elements is shown in the Table 10, where the bold italic number denotes the controlling tensile force of the actively-pre-tension cables in each single construction step. The displacement of the structure during the construction is listed in Table 11.
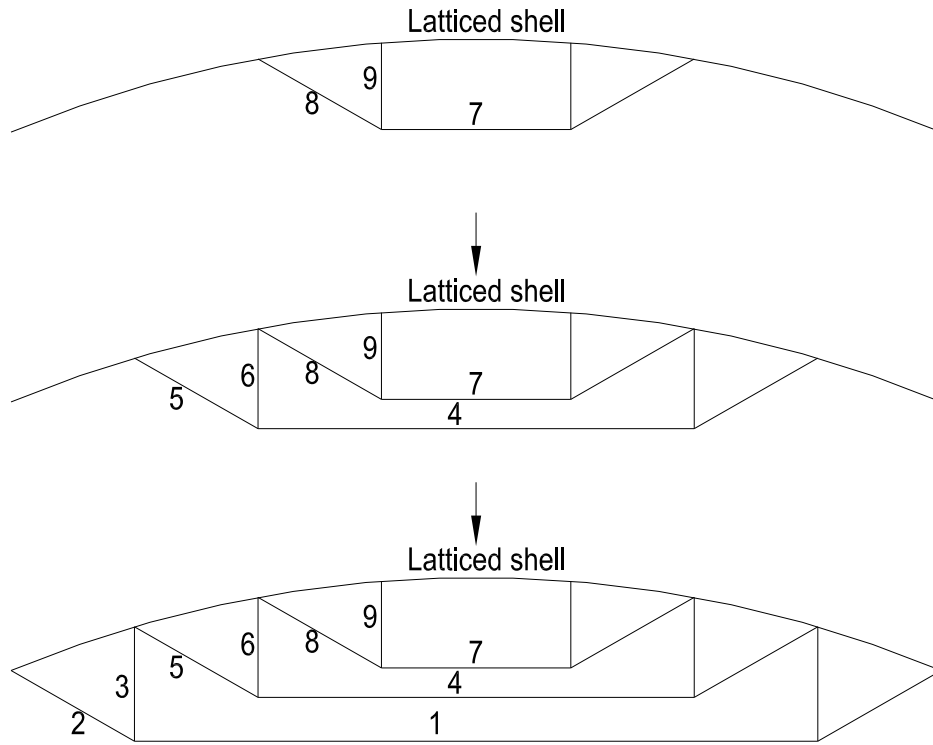
Figure 7. Construction Sequence in Scheme 1

Note that the tensile force imposed to the elements of group 5 and 8 are approximately 50.2% and 50.56% of the designed pre-tension respectively in this scheme. The largest tensile force of the actively-pre-tension cables is 732857N. It is shown that the nodes near to the cables being tensioned have the upward vertical displacement. The space position of each node meets the design state after the structure constructed.

4.2   Scheme 2
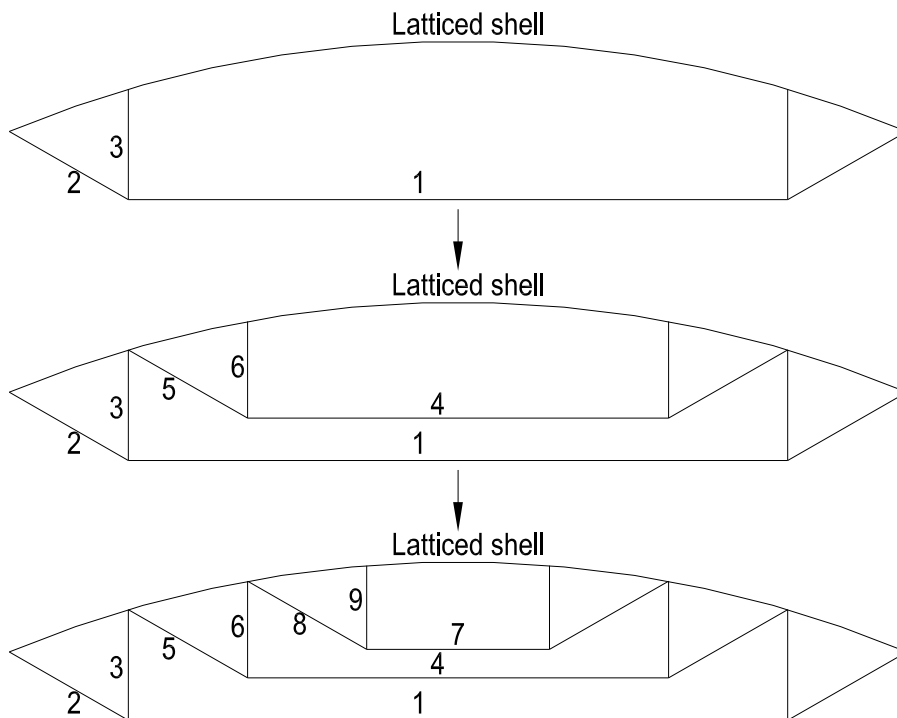
Figure 8. Construction Sequence in Scheme 2

A single-stage fabrication method is adopted in this scheme. The diagonal cables of cable-bar system of each ring are tensioned simultaneously. Diagonal cables in different rings are tensioned respectively for only one time. Tensile force in each step could be acquired in the equilibrium state by killing elements fabricated in the next step. As shown in Figure 8, the construction steps in this scheme are as follows:

Step 1, 77.78% of the design pre-tension force is imposed to the elements of group 2;

Step 2, 92.76% of the design pre-tension force is imposed to the elements of group 5;

Step 3, 100% of the design pre-tension force is imposed to the elements of group 8;

The arrangement of this construction scheme is just on the contrary of the scheme 1. The steps of the animation in ANSYS are opposite to the actual situation. Each configuration of the structure is determined by the inverse analysis respectively since a single-stage fabrication scheme is applied according to the aforementioned text. The sequences of animation analysis by the nonlinear finite element method in ANSYS are presented as follows:

Step 1, the equilibrium state and the tensile force of the elements of group 2 are obtained by killing the elements of group 5 and 8;

Step 2, the equilibrium state and the tensile force of the elements of group 5 are computed out by killing the elements of group 8;

Step 3, the equilibrium state and the tensile force of the elements of group 8 are just the ideal fabricated state of the structure;

Table 12. The Variation of the Axial Internal-force of the Cable-bar Elements (Units: kN)

Group	Step 1	Step 2	Step 3
1	2933.442	3689.205	3778.186
2	*570.046*	715.473	732.857
3	-235.557	-298.477	-306.308
4	0	1310.571	1413.329
5	0	*254.737*	274.624
6	0	-107.103	-115.922
7	0	0	449.795
8	0	0	*173.747*
9	0	0	-72.661

Table 13. The Displacement of the Typical Nodes A, B, C and D (Units: mm)

disp	Step 1	Step 2	Step 3
U_A	55.08182	10.113194	4.751852
U_B	-36.695176	30.941798	8.518034
U_C	-49.284646	-29.192398	12.395205
U_D	-38.559757	-37.318611	-30.426954

The variation of the axial internal-force of the cable-bar elements is given out in Table 12. The bold italic number denotes the controlling tensile force of the actively-pre-tension cables in each construction step. The displacement of the structure during the configuration is shown in Table 13. Note that the tensile force exerted to the elements of group 2 and 5 are approximately 77.78% and 92.76% of the designed pre-tension. The largest tensile force of actively-pre-tension cables is 570046N in this scheme. It is noted that the configuration of the structure is close to the design state after the completion of the implement of the elements of group 2 and 5. It implies that the contribution of the implemented pre-tension of the elements of group 8 to the fabrication of the suspen-dome could be omitted. And the nodes near to the cables being tensioned have a positive vertical displacement. It seems that the position of each node meets the design state after the structure constructed.

4.3   Scheme 3

A two-stage fabrication method is adopted in this scheme. The actively-pre-tensioned cables are tensioned simultaneously in each step. Diagonal cables in different rings are tensioned respectively for twice. Tensile force of each step in stage 1 is assumed to 50% of the design pre-tension. Tensile force of each step in stage 2 could be acquired in the equilibrium state by killing elements fabricated in the next step. The arrangements of the construction are as follows:

Stage 1:
Step 1, 50% of the design pre-tension is imposed to the elements of group 2;
Step 2, 50% of the design pre-tension is imposed to the elements of group 5;
Step 3, 50% of the design pre-tension is imposed to the elements of group 8;

Stage 2:
Step 1, 79.44% of the design pre-tension is imposed to the elements of group 8;
Step 2, 84.4% of the design pre-tension is imposed to the elements of group 5;
Step 3, 100% of the design pre-tension is imposed to the elements of group 2;

A mixed analysis method combined with the inverse analysis and direct analysis is applied to the construction sequence simulation of the structure in this scheme. Each configuration of the structure during the construction is determined by the nonlinear finite element analysis. The tensile force of the actively-pre-tension cables of group 8 and 5 should be set to approximately 79.44% and 84.4% of the designed pre-tension respectively in the stage 2. The arrangements of the animation computation are described according to the sequences of the calculations as follows:

Stage 1:

Step 1, the equilibrium state in this step is obtained by the following three parts of analysis:

An intermediate state is obtained by the analysis of killing the elements of group 8;

A state is obtained by the analysis of killing the elements of group 5 from the latest state;

A single-point temperature stress is imposed to one end of the elements of group 2 to simulate a compressive force until the axial internal-force of the actively-pre-tensioned cables achieve approximately 50% of the design pre-tension force from the second state in this step. The temperature could be determined by some trial computations.

Step 2, the equilibrium state in this step is obtained by the following two parts of analysis:

An intermediate state is obtained by the analysis of alive the elements of group 5 being killed from the state of step 1 firstly;

A single-point temperature stress is imposed to one end of the elements of group 5 to simulate a compressive force until the axial internal-force of the actively-pre-tension cables achieve approximately 50% of the design pre-tension from the latest state in this step. The temperature could be determined by some trial computations.

Step 3, the equilibrium state in this step is obtained by the following two parts of analysis:

An intermediate state is obtained by the analysis of alive the elements of group 8 being killed from the state of step 2 firstly;

A single-point temperature stress is imposed to one end of the elements of group 8 to simulate a compressive force until the axial internal-force of the actively-pre-tension cables achieve approximately 50% of the design pre-tension from the latest state in this step. The temperature could be determined by some trial computations.

Stage 2:

Step 1, the temperature of the end of the elements of group 8 which is used as the actively-pre-tension point in the last stage should be set to zero for the reason of energy conservation. And then the axial internal-force of the actively-pre-tension cables achieve approximately 79.44% of the design pre-tension force after the analysis completed;

Step 2, the temperature of the end of the elements of group 5 which is used as the actively-pre-tension point in the last stage should be set to zero for the reason of energy conservation. It is noted that the axial internal-force of the actively-pre-tension cables achieve approximately 84.4% of the design pre-tension force after the nonlinear analysis finished;

Step 3, the temperature of the end of the elements of group 2 which is used as the actively-pre-tension point in the last stage should be set to zero for the reason of energy conservation. Note that the axial internal-force of the cables and bars achieve approximately 100% of the design pre-tension force after the computation fulfilled;

The variation of the axial internal-force of the cable-bar elements is shown in Table 14 while the displacement of the structure during the fabrication is presented in Table 15. The bold italics number in Table 14 denotes the controlling force of the actively-pre-tensioned cable in each construction step. The tensile force of the elements of group 8 in the stage 2 is 79.44% of the design pre-tension but not 100%, while those elements of group 5 in the stage 2 is 84.4% of the design pre-tension. A desired axial internal-force of each element is recorded when the last construction step completed. The nodes which are close to the actively-pre-tension cables have a positive vertical displacement. It is noted that the position of each node meets the design state after the structure constructed. A mostly economical construction method of scheme 3 could be regarded for the lowest magnitude tensile force of the actively-pre-tensioned cables in the above 3 schemes with the maximum value of 366615N during the construction. Therefore, cheaper equipments could be used for the construction. In this scheme the structure rigidity is shaped gently and engineers have more chance to adjust the construction errors.

Table 14. The Variation of the Axial Force of the Cable-bar Elements (Units: kN)

Group	Step 1	Step 2	Step 3	Step 4	Step 5	Step 6
1	1888.494	2271.428	2315.070	2341.094	2557.788	3778.186
2	*366.615*	440.973	449.479	454.552	496.647	*732.857*
3	-144.892	-177.900	-181.740	-184.041	-202.916	-306.308
4	0	706.163	757.943	787.603	1191.159	1413.329
5	0	*137.389*	147.584	153.434	*231.795*	274.624
6	0	-55.117	-59.947	-62.760	-97.558	-115.922
7	0	0	223.507	357.443	405.799	449.795
8	0	0	*86.389*	*138.023*	156.702	173.747
9	0	0	-34.369	-56.810	-65.007	-72.661

Table 15. The Vertical Displacement of the Typical Nodes A, B, C and D (Units: mm)

Disp	Step1	Step2	Step3	Step4	Step5	Step6
U_A	27.378023	4.620033	1.992812	0.427138	-12.428725	4.607384
U_B	-26.383106	7.599213	-3.477436	-9.949669	6.060556	8.382912
U_C	-31.769468	-23.459562	-3.470519	8.335725	16.886617	12.342352
U_D	-26.452058	-26.218994	-24.937856	-24.541326	-24.673249	-32.994649

5.   NODAL SPTIAL POSITION ERROR EFFECTS ON CONSTRUCTION

The effect due to nodal spatial position errors on the lower cable-bar system during the construction is analyzed. Based on the Scheme 1 of fabrication, the effect of the nodal position errors is investigated by using random imperfection modal method where the randomly normal distribution imperfection samples are generated. The effects of different magnitude of nodal position errors at all construction steps are listed from Table 19 to Table 20. Since guarante rate of the normal distribution between μ-σ and μ + σ is only 68.3% while between the interval (μ-3σ, μ+3σ) is 99.7%, it is obvious that the maximum nodal spatial position error should be under 0.03m with the deviation of axial internal-force may achieve the limited value of approximately 11.4%.

Table 19. The Effect of Position Errors on the Construction Step 1

Max error	R_R	R_σ
30mm	5.18%	0.30%
60mm	6.93%	2.08%
90mm	6.32%	4.05%
120mm	6.56%	7.60%
150mm	6.94%	7.62%

Table 20. The Effect of Position Error on the Construction Step 2

Max error	R_R	R_σ
30mm	3.24%	3.80%
60mm	5.95%	7.05%
90mm	9.85%	9.08%
120mm	10.41%	14.90%
150mm	15.84%	20.70%

6.   CONCLUSIONS

(1) Effects of different supporting conditions on the upper single layer latticed shell of the suspen-dome are not significant.

(2) Nodal spatial position errors should be restricted under an ultimate magnitude for its significant effect on suspen-dome.

(3) Little effects of construction errors on the mean axial internal-force among each group of cable-bar elements is obtained, while a great effect on the standard deviation of the axial force is obtained. And the effect of temperature variation is just on the contrary.

(4) A relatively low influence of temperature variation to the structure could be realized if integral structure model with concrete supporting system is adopted.

(5) The displacement of the structure during the construction is combined with mechanism displacement and elastic deformation. And a significant effect of the passively-pre-tension cables on the actively-pre-tensioned cables during the construction process should be much concerned.

(6) The configuration of the structure could be determined exactly as the pre-tension distribution is acquired. The inverse analysis method is suggested for the construction sequence simulation analysis of the suspen-dome if a single-stage fabrication scheme is adopted. A mixed analysis method with a combination of inverse and direct analysis proposed may be beneficial for the construction sequence simulation analysis of suspen-dome if a multi-stage- fabrication scheme is adopted.

(7) A multi-stage fabrication scheme is recommended due to low cost of construction.

ACKNOWLEDGEMENTS

REFERENCES

[1]   Dong, S.L. and Zhao, Y., "Discussion On Types and Classifications of Spatial Structures", Journal of Civil Engineering, 2004, Vol. 37, No. 1, pp. 7-12. [In Chinese]
[2]   Kitipornchai, S. and Kang, W.J. et al., "Factors Affecting the Design and Construction of Lamella Suspen-dome Systems", Journal of Constructional Steel Research, 2005, Vol. 61, pp. 764-785.
[3]   Kang, W.J. and Chen, Z.H. et al., "Analysis and Design of The General and Outmost-ring Stiffened Suspen-dome Structures", Engineering Structures, 2003, Vol. 25, pp. 1685–1695.
[4]   Kawaguchi, M. and Abe, M. et al., "Design, Tests and Realization of 'Suspen-dome' System", Journal of the IASS, 1999, Vol. 40, No. 131, pp. 179–92.
[5]   Zhen, J.H and Dong, S.L. et al., "Experimental Research on Construction Process of Levy Type Cable Dome", Journal of Building Structures, 2006, Vol. 27, No. 1, pp. 112-116. [In Chinese]

[6]   Luo, Y.Z. and Shen, Y.B., "Initial Configuration Determination of Cable Dome Structure and Analysis of Its Configuration Process", Journal of Zhejiang University (Engineering Science), 2004, Vol. 38, No. 10, pp. 1321-1327. [in Chinese]

[7]   Shen, Z.Y. and Zhang, L.X., "Simulation of Erection Procedures of Cable Domes Based on FEM", Chinese Journal of Computational Mechanics, 2002, Vol. 19, No. 4, pp. 466-471. [in Chinese]

[8]   Zhang, Z.H. and Dong, S.L. et al., "Design and Construction Analysis of Cable-strut Tensile Structures", Spatial Structures, 2003, Vol. 9, No. 2, pp. 20-24. [in Chinese]

[9]   Chen, L.M. and Dong, S.L. et al., "Theoretical and Experimental Study on The Construction of Cable Domes", Journal of Civil Engineering, 2006, Vol. 39, No. 11, pp. 33-36. [in Chinese]

[10]   Yuan, X.F. and Dong, S.L., "Inverse Analysis of Construction Process of Cable Dome", Journal of Building Structures, 2001, Vol. 22, No. 2, pp. 75-79. [in Chinese]

[11]   Li, G.L. and Wang, Z.Q. et al., "Test Study on Shaping of Double Ellipse Suspen-dome", Architecture Technology, 2007, Vol. 38, No. 5, pp. 348-351. [in Chinese]

[12]   Li, Y.M. and Zhang, Y.G., "Determination of Cable Forces During Construction for Cable-supported Latticed Shells", Journal of Building Structures, 2004, Vol. 25, No. 4, pp. 76-81. [in Chinese]

[13]   Zhang, Z.H. and Zhang, M.S., "Discussion on The Equilibrium Matrix Theory and Static and Stability Analysis of A Hybrid Spatial Structure Composed of Cables, Bars and Beams", Engineering Mechanics, 2004, Vol. 22, No. 6, pp. 7-14. [in Chinese]

[14]   Zhang, Z.H. and Zhang, M.S. et al., "Discussion on Some Problems of Beam-string Structures", Engineering Mechanics, 2004, Vol. 21, No. 6, pp. 26-30. [in Chinese]

INFLUENCE OF CABLE SLIDING ON THE STABILITY OF SUSPEN-DOME WITH STACKED ARCHES STRUCTURES

Liu Hongbo[1] and Chen Zhihua[1, 2, *]

[1] Department of Civil Engineering, Tianjin University, Tianjin 300072, China
[2] Tianjin Key Laboratory of Civil Engineering Structures and New Materials, Tianjin 300072, China
*(Corresponding author: E-mail: zhchen@tju.edu.cn)

ABSTRACT: A new type of continuous cable joint is presented in this paper for the suspen-dome with stacked arch. For this new cable joint, there are two state: locked state and unlocked state. In the locked state, the hoop cable cannot slide around cable joint. In the unlocked state, the hoop cable can slide around cable joint. In order to analyze the stability of suspen-dome with stacked arches structures under condition that the continuous cable joint is unlocked state, A three-node sliding cable element was used and its tangent stiffness matrix was determined based on the principal of virtual work and uniform strain assumption. The element was then implemented in commercial finite element software ABAQUS as a user defined element and applied in the stability analysis of a suspen-dome with stacked arches structure. Both symmetric and asymmetric load were considered for the suspen-dome with stacked arches structure to investigate the influence of cable joint state on its stability behavior. It was concluded that the stability behavior when the continuous cable joint is locked is better than that of when the continuous cable joint is unlocked.

Keywords: Suspen-dome with stacked arch structures, Continuous cable joint, Sliding cable element, Stability

1. INTRODUCTION

Steel cables are widely adopted in long-span structures due to their high strength and low self-weight. By pre-stressing the steel cables, more effective structures can be achieved to span larger distance, such as suspen-dome structures [1], beam string structures [2], cable dome [3], Cable supported barrel vault structure [4] and so on. Suspen-dome structure has been widely applied as roof structures in many buildings, such as Hikarigaoka dome and Fureai dome in Japan, Badminton Gymnasium for 2008 Beijing Olympic Games in China, and Jinan Olympic sports center's gymnasium for the 2009 11th National Olympic Games in China. Arch structures are a traditional structure, and it can cover long span. Introducing arch structures into grid structures, some effective structures can be also achieved to span longer distance, such as the roof structures of Huhhot Airport and Yangtze River Flood-control Model-testing Hall [5].

In order to form a more effective structure, suspen-dome with stacked arch structure was presented by combining the suspen-dome structures and arch structures, which has been adopted in the roof structure of Chiping Gymnasium. The suspen-dome with stacked arch structure is to use the advantages of arch structures to enhance the suspen-dome structures. Thus the integral mechanical behaviour of the new hybrid structures is efficiently improved, the structural span can be increased and the architectural shapes of large-span structures are also enriched. Therefore, suspen-dome with stacked arch structures have been developed, as a kind of new large-span space structural system.

Many investigations have been performed for the suspen-dome structures through experimental research and numerical analysis. Therefore, the fundamental properties for these structures can be well understood [3-12]. Due to the existence of arch, the structural behavior of suspen-dome with stacked arch structure is different from suspen-dome structures. Therefore, it is desired to conduct some research on the structural behavior of suspen-dome with stacked arch structure.

2.   STRUCTURAL FORM AND ARRANGEMENT

The Chiping Gymnasium is taken as an example to introduce the form and arrangement of suspen-dome with stacked arches structures, as it shown in Figure 1~ Figure 6. The suspen-dome with stacked arches structures consist of upper arch and lower suspen-dome, and the arch and suspen-dome is connected by struts as it shown in Figure 2 and Figure 3. For the low suspen-dome, it consists of single-layer lattice shell, radial steel bars, hoop cables and struts as it shown in Figure 4 and Figure 5. Seven rings of radial steel bars, hoop cables and struts were arranged under single-layer lattice shell in suspen-dome. For the pre-stressing of hoop cables, it is determined by optimization analysis using ANSYS. Under dead load and half of live load, the optimal pre-stressing force for each hoop is 127 kN, 420 kN, 390 kN, 530 kN, 810 kN, 1242 kN, 2060 kN, respectively. Two hoops of bearings are set in this structure as it shown in Figure 3 and Figure 5.
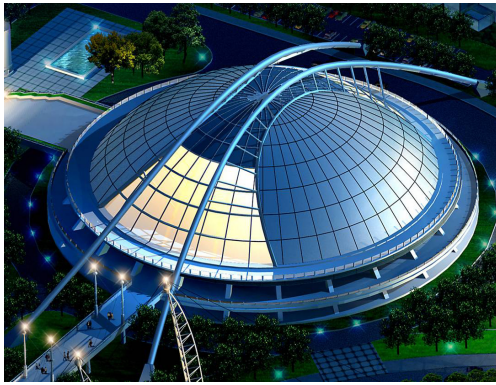
Figure 1. Overview of Chiping Gymnasium
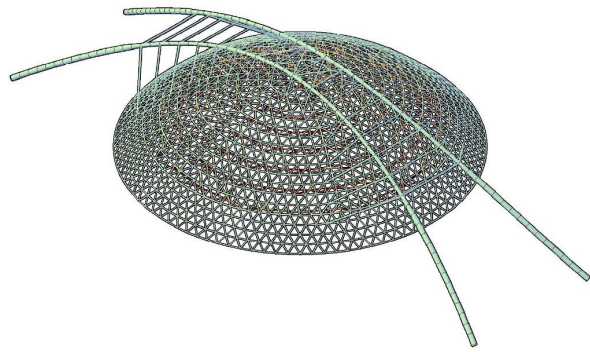
Figure 2. Axonometric View of Structural System
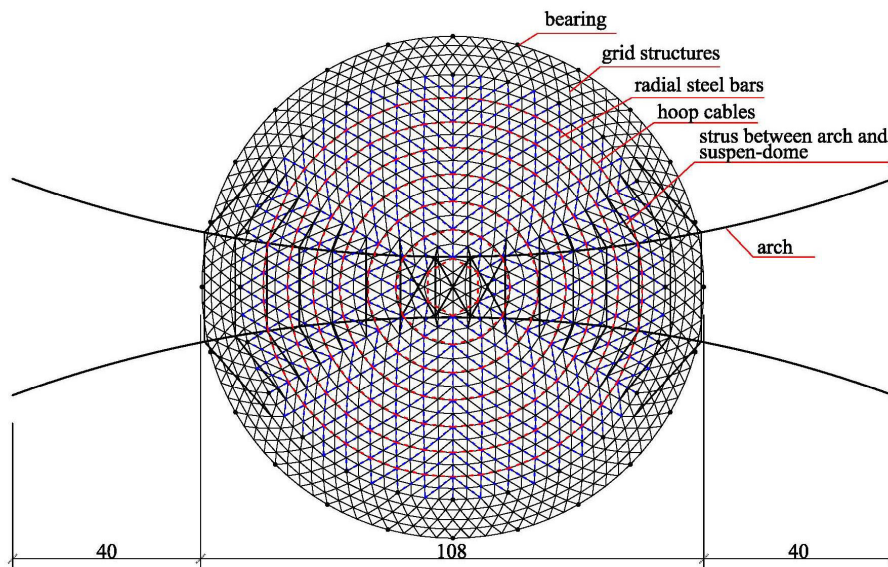
Figure 3. Top View of the Suspen-dome with Stacked Arch Structural
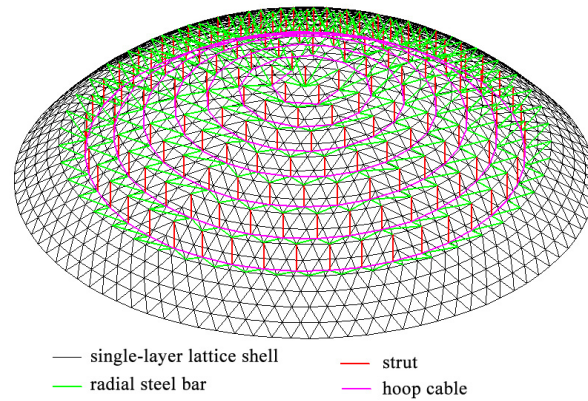
Figure 4. Axonometric View of Suspen-dome Structure
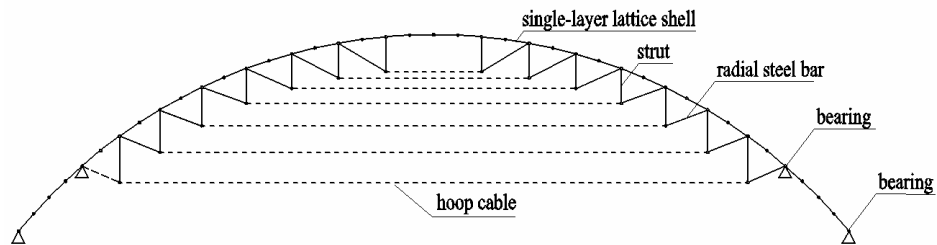
Figure 5. Sectional View of Suspen-dome Structure
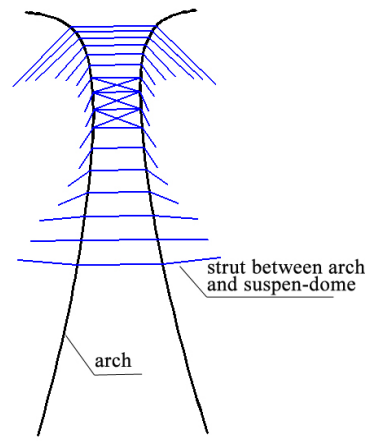
Figure 6. Arch Structure

In practice, two kinds cable joints are usually considered for suspen-dome structures. One is non-continuous cable joint as shown in Figure 7, and the other is continuous cable joint as shown in Figure 8. If the non-continuous cable joint is adopted, the two adjacent hoop cables are independent and the hoop cables cannot slide around joints. Comparatively, if the continuous cable joint is adopted, each circumference hoop cable is a continuous cable and the hoop cable can slide around joints. Therefore, the continuous cable joint must be used when the pre-stressing is introduced by tensioning hoop cables.
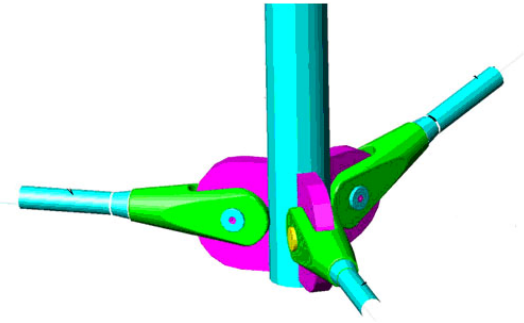
Figure 7. Non-sliding Cable-strut Joint

Figure 8. Sliding Cable-strut Joint

In the pre-stressing construction process, it is found that there is significant friction between cable and joint in the present continuous cable joint, which induces large pre-stressing loss[13]. In order to overcome this problem, a new continuous cable joint is presented for the suspen-dome with stacked arch structures as it shown in Figure 9 and Figure 10. Compared with the past continuous cable joint, the sliding friction between cable and joint is replaced to rolling friction because the rolling friction is much smaller than sliding friction.
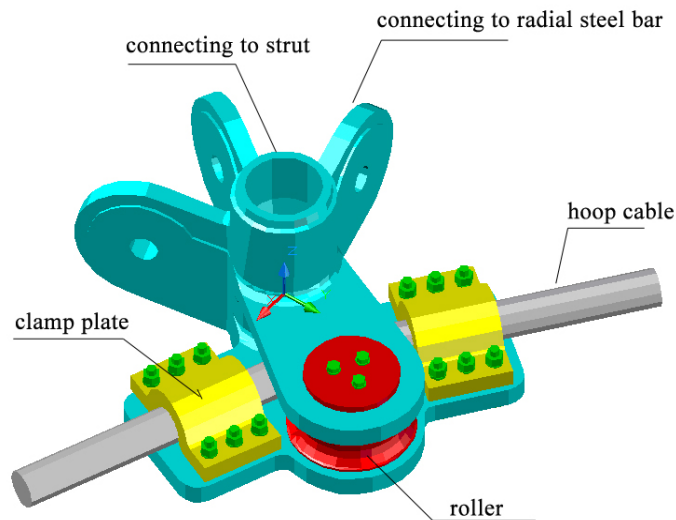
Figure 9. Assembly Drawing of the Presented Continuous Cable Joint
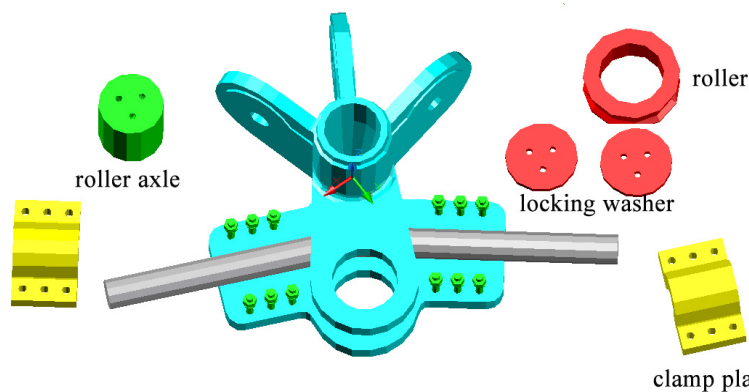
Figure 10. Decomposition Drawing of the Presented Continuous Cable Joint

The new continuous cable joint has two states. One is locked state and the cable is locked by clamp plates in this state. The other is unlocked state and the cable is unlocked by clamp plates in this state. In the pre-stressing construction, the unlocked state is used. For the usage stage, it is confused for the best state choice. In order to choose a rational joint state, the stability behavior of suspen-dome with stacked arch structures is investigated under both locked state and unlocked state.

3. THREE-NODE SLIDING CABLE ELEMENT

In suspen-dome with stacked arches structures, the hoop cable usually threads through a number of cable-strut joints. If the non-sliding cable-strut joint used, the cables can then be simplified as 2-node straight bar elements separated by adjacent joints in finite element analysis. If the sliding cable-strut joint is used, the above simplification may cause significant error due to the neglect of cable sliding. Some techniques have been presented to consider the cable sliding based on finite element analysis with simplified separate cable elements [14-16]. They all need manual iteration intervened by engineers, which are time consuming especially for large scale cable structures. Formulating sliding cable element is a more convenient way to simulate sliding cables. Sliding cable elements have been developed and verified for the analysis of parachute systems [17]. In this paper, a tangent stiffness matrix of three-node sliding cable element was determined based on the principle of virtual work and total Lagrange formulation presented in reference 17. The element was then implemented in commercial finite element software ABAQUS as a user defined element [18].

A three-node cable element is as shown in Figure 11. The cable element has three node, node 1, node 2 and node 3, and each node has three displacement degrees of freedom. The fundamental kinematic assumption of the three-node cable element states that: (1) the cable remains straight between adjacent nodes; (2) the self-weight of the cable can be ignored and all the loads act directly on the nodes; (3) the strain is uniform along the element, i.e., the strain in all segments of the cable is the same at any time; (4) the sliding node can not slide across the adjacent nodes along the cable, which means the order of the nodes along the cable remains unchanged.
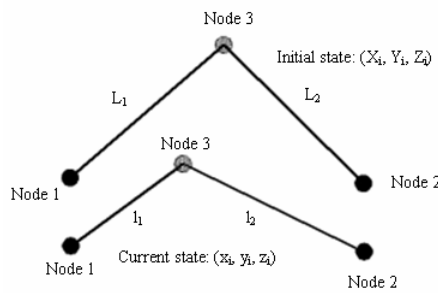
Figure 11. A Three-node Cable Element

The current element length is determined from the current nodal coordinates (x_1, y_1, z_1), (x_2, y_2, z_2), and (x_3, y_3, z_3) as

$$l = l_1 + l_2 \tag{1}$$

In which

$$l_1^2 = (x_3 - x_1)^2 + (y_3 - y_1)^2 + (z_3 - z_1)^2 \tag{2}$$

$$l_2^2 = (x_3 - x_2)^2 + (y_3 - y_2)^2 + (z_3 - z_2)^2 \tag{3}$$

The current nodal coordinates are related to the initial coordinates (X_1, Y_1, Z_1), (X_2, Y_2, Z_2), and (X_3, Y_3, Z_3) and current nodal displacements (u_1, v_1, w_1), (u_2, v_2, w_2), and (u_3, v_3, w_3) by

$$x_i = X_i + u_i \,;\, y_i = Y_i + v_i \,;\, z_i = Z_i + w_i \qquad (i = 1, 2, 3) \tag{4}$$

The principle of virtual work for the three-node cable element in total Lagrange formulation (TL) can be expressed as:

$$\int_L S_{11} \delta e_{11} A_0 dL = P \delta d \tag{5}$$

In which

$$\delta d = (\delta u_1 \; \delta v_1 \; \delta w_1 \; \delta u_2 \; \delta v_2 \; \delta w_2 \; \delta u_3 \; \delta v_3 \; \delta w_3)^T \tag{6}$$

in which e_{11} is the Green - Lagrange strain, S_{11} is the second Piola - Kirchhoff stress, L is the total length of the cable at initial configuration, P and δd are the node loads and displacements respectively and A_0 is the cross-sectional area of the cable, which is a constant over the entire element length. In the TL formulation, the integration is performed over the initial configuration. Because the strain and stress are assumed to be constant along the element, the integration in Eq. 5 is performed analytically:

$$S_{11} \delta e_{11} A_0 L = P \delta d \tag{7}$$

Assume

$$\delta e_{11} = B \delta d \tag{8}$$

In which B is a vector of 9. Substitute Eq. 8 into Eq. 7, gives:

$$S_{11} B A_0 L \delta d = P \delta d \tag{9}$$

Considering the randomicity of the variation of node displacements δd, the equilibrium equation of the three-node cable element can be expressed as:

$$S_{11} B A_0 L = P \tag{10}$$

The incremental equilibrium equation of the sliding cable element can then be termed as:

$$K \Delta d = P \tag{11}$$

In which K is the tangent stiffness matrix of the sliding cable element, and

$$K = \frac{\partial(S_{11}BA_0L)}{\partial d} = A_0 LB^T \frac{\partial S_{11}}{\partial d} + A_0 LS_{11} \frac{\partial B}{\partial d} \tag{12}$$

The second Piola - Kirchhoff stress for the one-dimensional sliding cable element is given by:

$$S_{11} = S_{11}^0 + S_{11}^T + Ee_{11} \tag{13}$$

In which S_{11}^0 is the initial stress in the cable; S_{11}^T is the thermal stress in the cable induced by temperature variation and E is the Young's modulus. Then

$$\frac{\partial S_{11}}{\partial d} = \frac{\partial\left(S_{11}^0 + S_{11}^T + Ee_{11}\right)}{\partial d} = E\frac{\partial e_{11}}{\partial d} = EB \tag{14}$$

For the one-dimensional cable element, the Green-Lagrange strain is given by [8]:

$$e_{11} = \frac{(l_1 + l_2)^2 - (L)^2}{2L^2} \tag{15}$$

Then

$$B = \frac{\partial e_{11}}{\partial d} = \frac{\partial\left(\dfrac{(l_1 + l_2)^2 - (L)^2}{2L^2}\right)}{\partial d} = \frac{l}{L^2}\frac{\partial l}{\partial d} = \frac{(l_1 + l_2)}{L^2}\left(\frac{\partial l_1}{\partial d} + \frac{\partial l_2}{\partial d}\right) \tag{16}$$

In which

$$\frac{\partial l_1}{\partial d} = \left\{(-1)\times\frac{\Delta x_1}{l_1} \quad (-1)\times\frac{\Delta y_1}{l_1} \quad (-1)\times\frac{\Delta z_1}{l_1} \quad 0 \quad 0 \quad 0 \quad \frac{\Delta x_1}{l_1} \quad \frac{\Delta y_1}{l_1} \quad \frac{\Delta z_1}{l_1}\right\}^T \tag{17}$$

$$\frac{\partial l_2}{\partial d} = \left\{0 \quad 0 \quad 0 \quad (-1)\times\frac{\Delta x_2}{l_2} \quad (-1)\times\frac{\Delta y_2}{l_2} \quad (-1)\times\frac{\Delta z_2}{l_2} \quad \frac{\Delta x_2}{l_2} \quad \frac{\Delta y_2}{l_2} \quad \frac{\Delta z_2}{l_2}\right\}^T \tag{18}$$

$$\frac{\partial l}{\partial d} = \left\{(-1)\times\frac{\Delta x_1}{l_1} \quad (-1)\times\frac{\Delta y_1}{l_1} \quad (-1)\times\frac{\Delta x_1}{l_1} \quad (-1)\times\frac{\Delta y_2}{l_2} \quad (-1)\times\frac{\Delta z_2}{l_2} \quad \frac{\Delta x_2}{l_2}+\frac{\Delta x_1}{l_1} \quad \frac{\Delta y_2}{l_2}+\frac{\Delta y_1}{l_1} \quad \frac{\Delta z_2}{l_2}+\frac{\Delta z_1}{l_1}\right\}^T \tag{19}$$

Then

$$\frac{\partial B}{\partial d} = \frac{\partial\left(\dfrac{l}{L^2}\dfrac{\partial l}{\partial d}\right)}{\partial d} = \frac{1}{L^2}\left(\frac{\partial l}{\partial d}\frac{\partial l}{\partial d} + l\frac{\partial^2 l}{\partial d^2}\right) \tag{20}$$

In which

$$
\frac{\partial^2 l}{\partial d^2} = (-1) \times
\begin{Bmatrix}
\frac{\Delta x_1^2 - l_1^2}{l_1^3} & \Delta x_1 \Delta y_1 & \Delta x_1 \Delta z_1 & 0 & 0 & 0 & (-1) \times \frac{\Delta x_1^2 - l_1^2}{l_1^3} & (-1) \times \Delta x_1 \Delta y_1 & (-1) \times \Delta x_1 \Delta z_1 \\[4pt]
\Delta x_1 \Delta y_1 & \frac{\Delta y_1^2 - l_1^2}{l_1^3} & \Delta y_1 \Delta z_1 & 0 & 0 & 0 & (-1) \times \Delta x_1 \Delta y_1 & (-1) \times \frac{\Delta y_1^2 - l_1^2}{l_1^3} & (-1) \times \Delta y_1 \Delta z_1 \\[4pt]
\Delta x_1 \Delta z_1 & \Delta y_1 \Delta z_1 & \frac{\Delta z_1^2 - l_1^2}{l_1^3} & 0 & 0 & 0 & (-1) \times \Delta x_1 \Delta z_1 & (-1) \times \Delta y_1 \Delta z_1 & (-1) \times \frac{\Delta z_1^2 - l_1^2}{l_1^3} \\[4pt]
& & & \frac{\Delta x_2^2 - l_2^2}{l_2^3} & \Delta x_2 \Delta y_2 & \Delta x_2 \Delta z_2 & (-1) \times \frac{\Delta x_2^2 - l_2^2}{l_2^3} & (-1) \times \Delta x_2 \Delta y_2 & (-1) \times \Delta x_2 \Delta z_2 \\[4pt]
& & & \Delta x_2 \Delta y_2 & \frac{\Delta y_2^2 - l_2^2}{l_2^3} & \Delta y_2 \Delta z_2 & (-1) \times \Delta x_2 \Delta y_2 & (-1) \times \frac{\Delta y_2^2 - l_2^2}{l_2^3} & (-1) \times \Delta y_2 \Delta z_2 \\[4pt]
& & & \Delta x_2 \Delta z_2 & \Delta y_2 \Delta z_2 & \frac{\Delta y_2^2 - l_2^2}{l_2^3} & (-1) \times \Delta x_2 \Delta z_2 & (-1) \times \Delta y_2 \Delta z_2 & (-1) \times \frac{\Delta y_2^2 - l_2^2}{l_2^3} \\[4pt]
& & & & & & \frac{\Delta x_1^2 - l_1^2}{l_1^3} + \frac{\Delta x_2^2 - l_2^2}{l_2^3} & \Delta x_1 \Delta y_1 + \Delta x_2 \Delta y_2 & \Delta x_1 \Delta z_1 + \Delta x_2 \Delta z_2 \\[4pt]
& & & & & & \Delta x_1 \Delta y_1 + \Delta x_2 \Delta y_2 & \frac{\Delta y_1^2 - l_1^2}{l_1^3} + \frac{\Delta y_2^2 - l_2^2}{l_2^3} & \Delta y_1 \Delta z_1 + \Delta y_2 \Delta z_2 \\[4pt]
sym & & & & & & \Delta x_1 \Delta z_1 + \Delta x_2 \Delta z_2 & \Delta y_1 \Delta z_1 + \Delta y_2 \Delta z_2 & \frac{\Delta z_1^2 - l_1^2}{l_1^3} + \frac{\Delta z_2^2 - l_2^2}{l_2^3}
\end{Bmatrix}
\tag{21}
$$

The $\partial B / \partial d$ can be determined by substituting Eq. 21 and Eq. 19 into Eq. 20. Then the tangent stiffness matrix can then be determined for the three-node cable element by substituting Eq. 13 ~ Eq. 21 into Eq. 12. The three-node cable element presented in this paper is implemented in ABAQUS as a user defined element and applied to study the stability of suspen-dome with stacked arch structure under condition that the continuous cable joint is unlocked state.

4.   STABILITY INVESTIGATION

This section will concentrate on the stability behavior of suspen-dome with stacked arch structure. Following are the main purpose: 1) study the stability behavior of suspen-dome with stacked arch structure if the continuous cable joint is unlocked or locked; 2) study the stability behavior of suspen-dome with stacked arch structure under symmetric and asymmetric load.

4.1   FEM Model of Suspen-dome with Stacked Arches

In this study, the roof structure of Chiping Gymnasium was taken as the studied model. Two finite element models, Model A and Model B, were setup with commercial finite element software ABAQUS. In the Model A, the continuous cable joint is locked and the hoop cables were simulated by Element T3D2 (No compression). In the Model B, the continuous cable joint is unlocked and the hoop cables were simulated by the user-defined three-node sliding cable element. Element types for other members of the Suspen-dome with stacked arch structure are all same for Model-A and Model-B, as shown in Table 1. The nodal displacement DX, DY and DZ of all nodes at bearing as it shown in Figure 3 were restrained. Materials for all the members and cables were assumed to be elastic. The Young's module are $E = 2.06 \times 10^8 \, \text{kN/m}^2$ for the steel tubes and $E = 1.95 \times 10^8 \, \text{kN/m}^2$ for the steel cables. The material for steel cables was set to be no compression material. The FE model of the suspen-dome with stacked arch structure is shown in Figure 12.
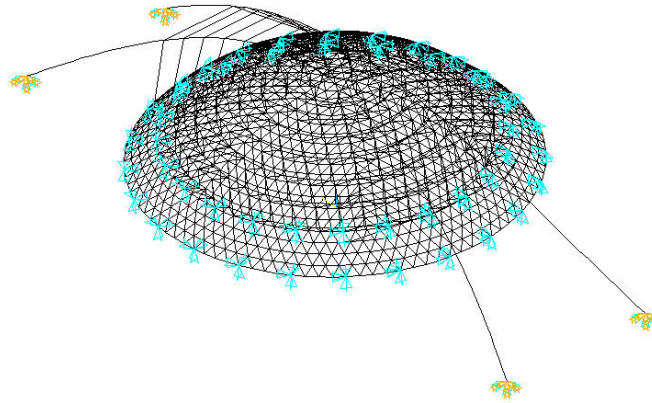
Figure 12. FEM Model of Suspen-dome with Stacked Arch Structure

Table 1. Element Type for Finite Element Models

Members	Element type	
	Model-A	Model-B
Single-layer lattice dome	B33 (2-node 3-D cubic beam element)	
Arch	B33 (2-node 3-D cubic beam element)	
Strut	T3D2 (2-node linear displacement 3-D truss element)	
Radial cables	T3D2 (No compression)	
Latitudinal cables	Three-node sliding cable element	T3D2 (No compression)

4.2   Load Cases for Stability Analysis of Suspen-dome with Stacked Arches

In design practice, the stability of lattice dome structures is often evaluated by tracing the nonlinear equilibrium path of the structure under proportional loading. Geometric nonlinearity should be considered and arc-length method is often adopted for equilibrium path tracing. The displacement-controlled method is used in this stability analysis.

Only uniform loads were considered in the stability analysis besides pre-stressing in hoop cables. In order to investigate the stability behavior under various load case, four load cases were considered as it shown Figure 15. For the Load Case 1, Uniform loads were applied on the entire span of single layer lattice shell. For the Load Case 2, Uniform loads were applied on the inner area of single layer lattice shell. For the Load Case 3, Uniform loads were applied on the upper half span of single layer lattice shell. For the Load Case 4, Uniform loads were applied on the right half span of single layer lattice shell.

(a) Load Case 1   (b) Load Case 2

(c) Load Case 3   (d) Load Case 4
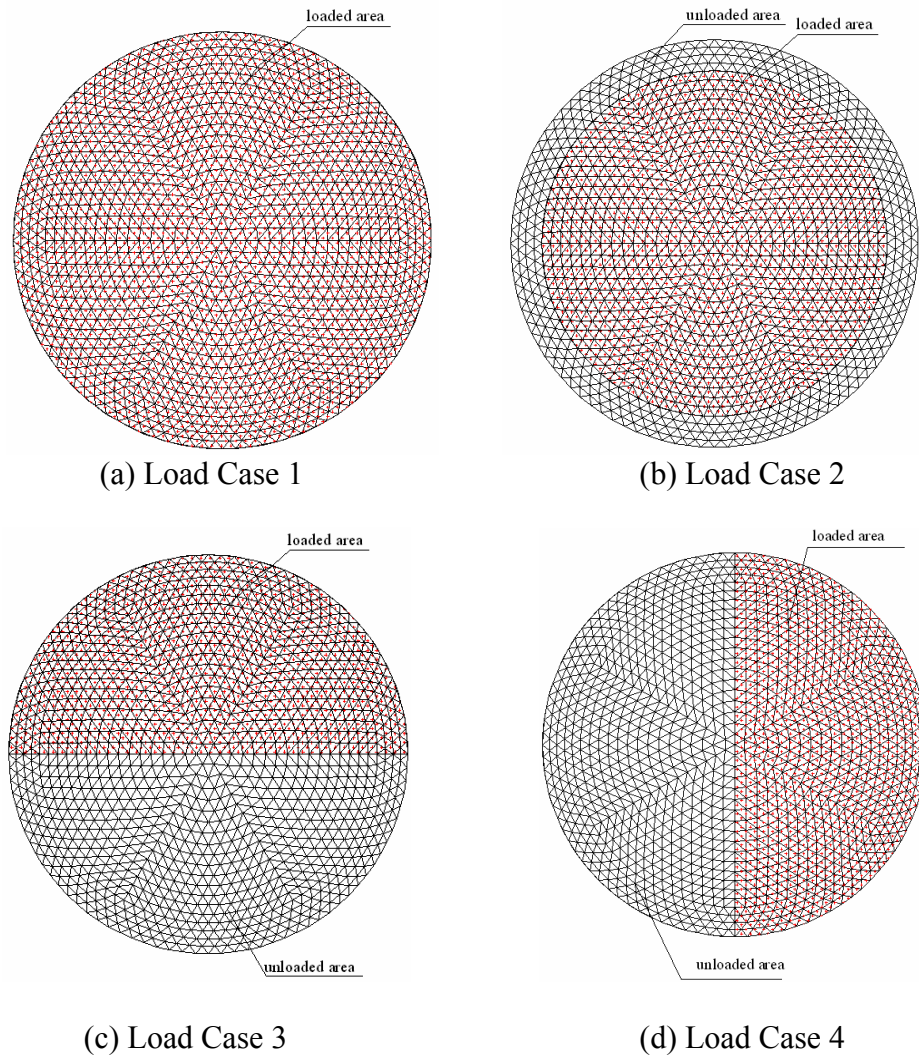
Figure 13. Loading Conditions

4.3   Stability Analysis under Load Case 1

Figure 14 and Figure 15 shows that the instability modes for Model A and Model B under Load Case 1. Model A is firstly instable near the outmost rings. Model B is firstly instable near the center. Figure 16 shows that the typical load-displacement curves for Model A and Model B. From the Load-displacement curves, it can be concluded that the critical load of Model A with value of 13.78 kN/m^2 is 5.6% higher than that of Model B with value of 13.05 kN/m^2. Due to the existence of above arches, the nodal displacement and member stress is very uniform under uniform loading. For the Model A, because the continuous cable joint is locked, the adjacent members will share some displacement and member stress if local nodal displacement or member stress is extreme large. Therefore, the stability behavior of Model A is better than that of Model B under Load Case 1.
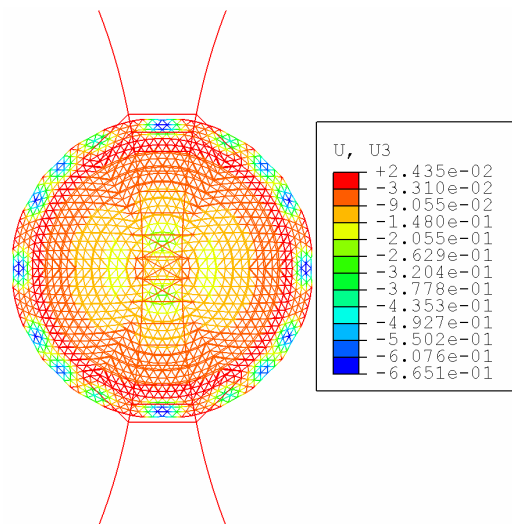
Figure 14. Instability shape of Model A under Load Case 1
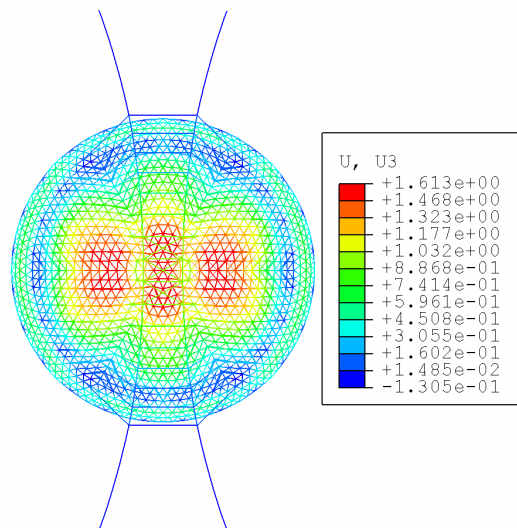
Figure 15. Instability Shape of Model B under Load Case 1
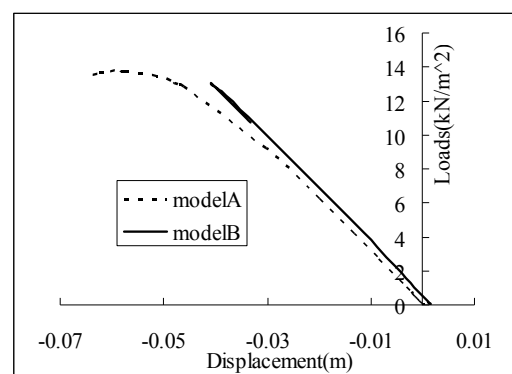
Figure 16. Load-displacement Curves by Nonlinear Stability Analysis for Load Case 1

4.4   Stability Analysis under Load Case 2

Figure 17 and Figure 18 shows that the instability modes for Model A and Model B under Load Case 2. It is clear that the instability shape of Model A is symmetric and Model B is asymmetric. Figure 19 shows that the typical load-displacement curves for Model A and Model B. From the Load-displacement curves, it can be concluded that the critical load of Model A with value of 16.04 kN/m^2 is 24.4% higher than that of Model B with value of 12.89 kN/m^2. Similar to the stability under Load Case 1, it is concluded that the stability behavior of Model A is better than that of Model B under Load Case 2.
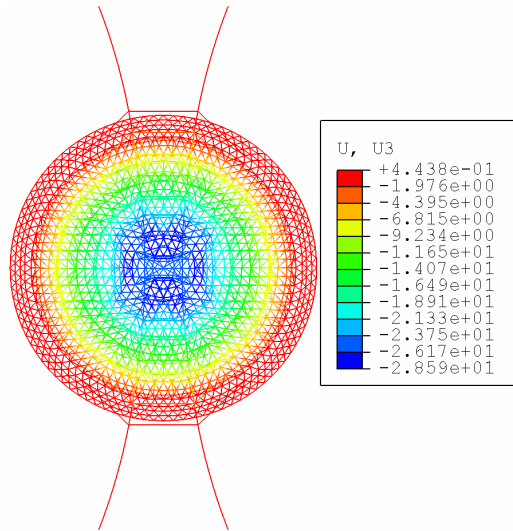
Figure 17 Instability shape of Model A under Load Case 2
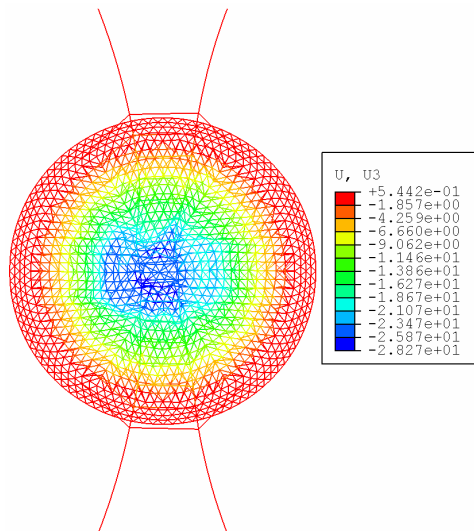
Figure 18 Instability shape of Model B under Load Case 2
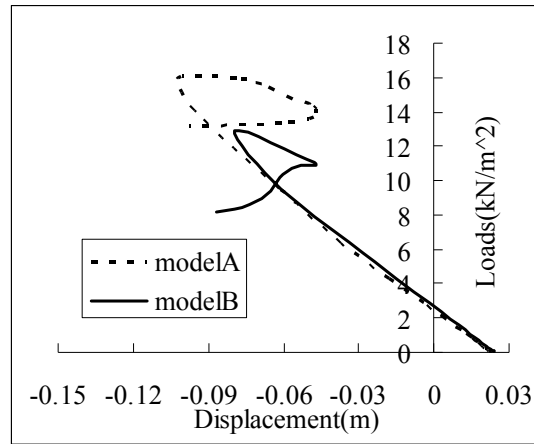
Figure 19. Load-displacement Curves by Nonlinear Stability Analysis for Load Case 2

4.5   Stability analysis under Load Case 3

Figure 20 and Figure 21 shows that the instability modes for Model A and Model B under Load Case 3. It is clear that the instability area of Model A is larger than that of Model B. Figure 22 shows that the typical load-displacement curves for Model A and Model B. From the Load-displacement curves, it can be concluded that the critical load of Model A with value of 15.44 kN/m^2 is 42.5% higher than that of Model B with value of 10.85 kN/m^2. Similar to the stability under Load Case 1, it is concluded that the stability behavior of Model A is better than that of Model B under Load Case 3.
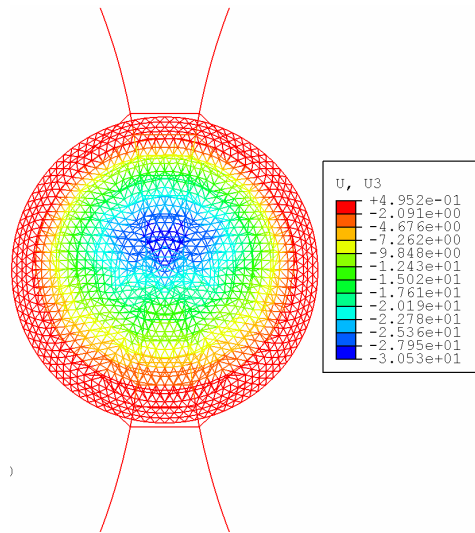
Figure 20. Instability Shape of Model A under Load Case 3
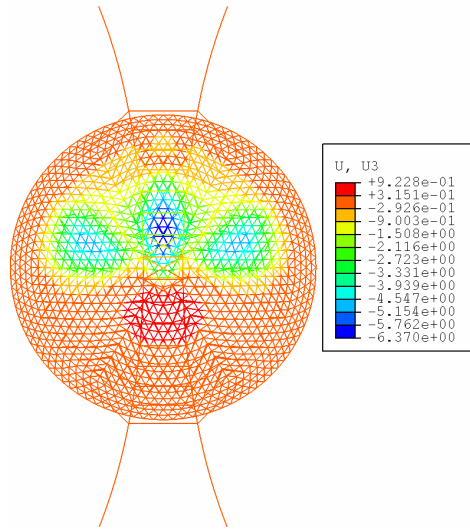
Figure 21. Instability Shape of Model B under Load Case 3
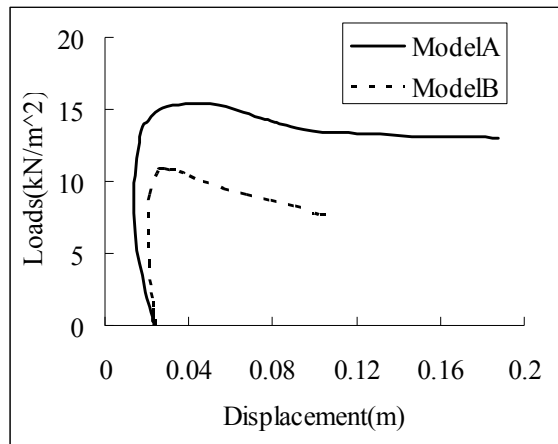
Figure 22. Load-displacement Curves by Nonlinear Stability Analysis for Load Case 3

4.6   Stability analysis under Load Case 4

Figure 23 and Figure 24 shows that the instability modes for Model A and Model B under Load Case 4. It is clear that the instability area of Model A is larger than that of Model B. Figure 25 shows that the typical load-displacement curves for Model A and Model B. From the Load-displacement curves, it can be concluded that the critical load of Model A with value of 17.07 kN/m^2 is 9.7% higher than that of Model B with value of 15.56 kN/m^2. Similar to the stability under Load Case 1, it is concluded that the stability behavior of Model A is better than that of Model B under Load Case 4.
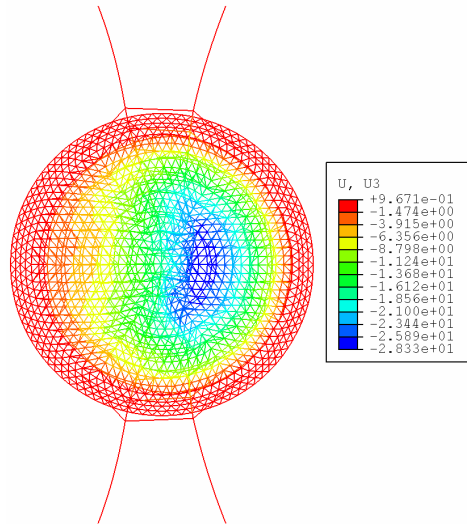
Figure 23. Instability Shape of Model A under Load Case 4
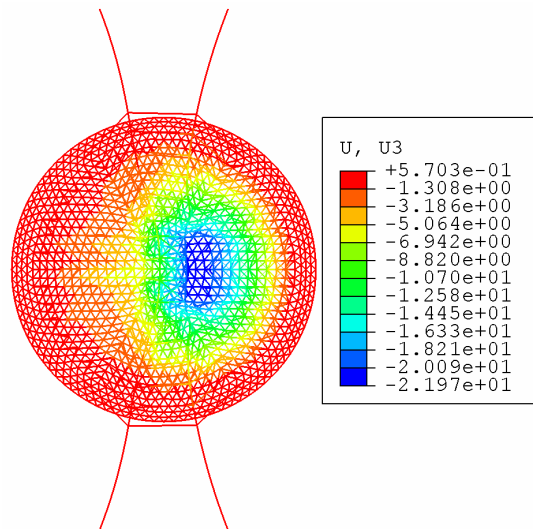
Figure 24. Instability Shape of Model B under Load Case 4
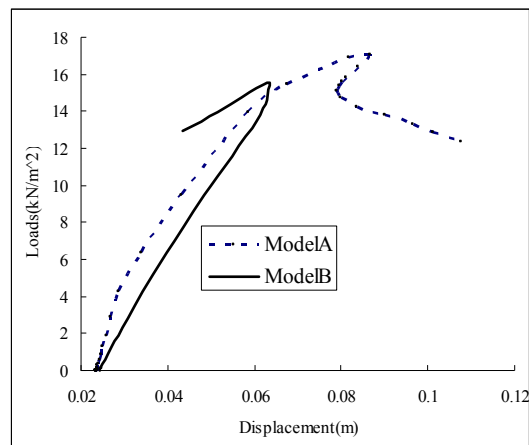
Figure 25. Load-displacement Curves by Nonlinear Stability Analysis for Load Case 4

5.   CONCLUSIONS

A new structural system of suspen-dome with stacked arch structure is presented in this paper. In order to study the stability behavior of the suspen-dome with stacked arch structure under condition that the hoop cable can slide around cable joint, the tangent stiffness matrix of a three-node sliding cable element was derived. Then the three-node sliding cable element was implemented in commercial finite element software ABAQUS as a user defined element and applied in the stability analysis of a suspen-dome with stacked arch structure under both symmetric and asymmetric loads. The following conclusions were obtained from the stability analysis results:

1) the critical load when the continuous cable joint is locked is higher than that when the of continuous cable joint is unlocked;

2) if the continuous cable joint is locked, the adjacent members will share some displacement and member stress if local nodal displacement or member stress is extreme large;

3) if the continuous cable joint is unlocked, the adjacent members cannot share some displacement and member stress effectively if local nodal displacement or member stress is extreme large;

4) compared with the stability under condition that the continuous cable joint is unlocked, the stability behavior is better under condition that the continuous cable joint is locked.

REFERENCES

[1]   Kawaguchi, M., Abe, M. and Tatemichi, I., "Design, Tests and Realization of 'suspen-dome' System, Journal of the IAAS, 1999, Vol. 40, No. 131, pp. 179-192.

[2]   Saitoh, M. and Okada, A., "The Role of String in Hybrid String Structure", Engineering Structures, 1999, Vol. 21, No. 8, pp. 280-284.

[3]   Kawaguchi, M., Tatemichi, I. and Chen, P.S., "Optimum Shapes of a Cable Dome Structure", Engineering Structures, 1999, Vol. 21, No. 8, pp. 719-725.

[4]   Chen, Z.H., Qiao, W.T. and Yan, X.Y., "Cable Supported Barrel Vault Structure System and Research on Mechanics Feature", Advanced Steel Construction, 2010, Vol. 6, No. 3, pp. 867-878.

[5]   Zhou, Z., Meng, S.P. and Wu, J., "Pretension Process Analysis of Arch-supported Prestressed Grid Structures Based on Member Initial Deformation", Advances in Structural Engineering, 2010, Vol. 13, No. 4, pp. 641-649.

[6]   Kang, W.J., Chen, Z.H., Lam, H.F., et al., "Analysis and Design of the General and Outmost-ring Stiffed Suspen-dome Structures", Engineering Structures, 2003, Vol. 25, pp. 1685-1695.

[7]   Kitipornchai, S., Kang, W.J., Lam, H.F., et al., "Facters Affecting the Design and Construction of Lamella Suspendome Systemes", Journal of Constructional Steel Research, 2005, Vol. 61, No. 6, pp. 764-785.

[8]   Chen, Z.H. and Li, Y., "Parameter Analysis on Stability of a Suspendome", International Journal of Space Structure, 2005, Vol. 20, No. 2, pp. 115-124.

[9]   Cui, X.Q. and Guo, Y.L., "Influence of Gliding Cable Joint on Mechanical Behavior of Suspen-dome Structures", International Journal of Space Structure, 2004, Vol. 19, No. 3, pp. 149-154

[10]   Cao, Q.S. and Zhang, Z.H., "A Simplified Strategy for Force Finding Analysis of Suspendomes", Engineering Structures, 2010, Vol. 32, No. 1, pp. 306-310.

[11]   Zhang, Z.H., Cao, Q.S., Dong, S.L. and Fu, X.Y., "Structural Design of a Practical Suspendome", Advanced Steel Construction, 2008, Vol. 4, No. 4, pp. 323-340.

[12]   Zhang, A.L., Liu, X.C., Wang, D.M., et al., "Static Experimental Study on the Model of the Suspend-dome of the Badminton Gymnasium for 2008 Olympic Games", Journal of Building Structures, 2007, Vol. 28, No. 6, pp. 58-67.

[13]   Wang, S., Zhang, G.J., Zhang, A.L., et al., "The Prestress Loss Analysis of Cable-strut Joint of the Badminton Gymnasium for 2008 Olympic Games", Journal of Building Structures, 2007, Vol. 28, No. 6, pp. 39-44.

[14]   Chen, Z.H., Liu, H.B., Wang, X.D., Zhou, T., "Establishing and Application of Cable-Sliding Criterion Equation", Advanced Steel Construction, 2011, Vol. 7, No. 2, pp. 131-143.

[15]   Cui, X.Q. and Guo, Y.L., "Influence of Gliding Cable Joint on Mechanical Behavior of Suspend-dome Structures", International Journal of Space Structures 2004, Vol. 19, No. 3, pp. 149-154.

[16]   Zhang, G.F., Dong, S.L., et al., "Research on Sliding Cable in Construction of Suspend-dome Structures", Journal of Zhejiang University (Engineering Science), 2008, Vol. 42, No. 6, pp. 1051-1057. [In Chinese]

[17]   Zhou, B., Accorsi, M.L. and Leonard, J.W., "Finite Element Formulation for Modeling Sliding Cable Elements", Computers & Structures, 2004, Vol. 82, No. 2-3, pp. 271-280.

[18]   ABAQUS/Standard User's Manual, Hibbitt, Karlsson & Sorensen Inc, Pawtucket (RI), 2002.

WELDED ALUMINUM ALLOY PLATE GIRDERS SUBJECTED TO SHEAR FORCE

Feng Zhou [1a, 1b], Ben Young [2,*] and Hin-Chung Lam [3]

[1a] Department of Building Engineering, Tongji University ,1239 Siping Road, Shanghai 200092, China
[1b] State Key Laboratory of Disaster Reduction in Civil Engineering, Shanghai 200092, China
[2] Department of Civil Engineering, The University of Hong Kong, Pokfulam Road, Hong Kong, China
[3] Katech International Ltd., Hung To Road, Kwun Tong, Hong Kong, China
*(Corresponding author: E-mail: young@hku.hk)

ABSTRACT: Numerical investigation of aluminum alloy plate girders subjected to shear force has been presented in this paper. The aluminum alloy plate girders were fabricated by welding three plates to form an I-section. A total of 118 numerical data are presented. A non-linear finite element model is developed and verified against experimental results. Geometric and material non-linearities were included in the finite element model. The welding of the aluminum alloy plate girders and the influence of the heat affected zone (HAZ) are also considered and carefully modeled. A sensitivity analysis on geometric imperfections of the aluminum alloy plate girders was performed. It was shown that the finite element model closely predicted the ultimate loads, web deformations and failure modes of aluminum alloy plate girders. Hence, the model was used for an extensive parametric study of cross-section geometries, and the web slenderness value ranged from 49 to 393. The test results and the shear resistances predicted by the finite element analysis were compared with the design strengths obtained using the European Code and American Specification for aluminum structures. Based on the experimental and numerical results, a design method for shear resistance of aluminum alloy plate girders is proposed in this study. The proposed design method is modified from the design rules in the EC9 Code. It is shown that the proposed design strengths are generally conservative and reliable.

Keywords: Aluminum structures, Design rules, Numerical investigation, Plate girder, Sensitivity analysis, Shear resistance

1. INTRODUCTION

In the past years, structural members in the form of plate girders have been widely used in the construction of buildings, bridges and other structures. They are popular to be used by designers since they can be tailor-made to suit any situation whereas hot-rolled steel sections are only rolled in a limited number of profiles. It should be noted that plate girders can also be fabricated from aluminum alloy. Aluminum alloy is much lighter than steel and sometimes it may be very useful for design of structures where the self-weight is an important design criterion. In addition, the nature of aluminum alloy would not normally rust so the maintenance of an aluminum structure is minimal and as a result of considerable cost-saving. Therefore, aluminum alloy plate girders have certain advantages over steel plate girders and should be investigated to gain a better understanding of their behaviour.

The webs of aluminum alloy plate girders are usually slender, hence, easy to buckle in shear at relative low applied loads. In order to provide an efficient and economical design, advantage should be taken of the post-buckling capacity of the plate girder. It has been well-documented by Evans [1] that a transversely stiffened girder can withstand loads considerably in excess of the load at which web buckling first occurs. This post-buckling reserve of strength arises from the development of tension field action within the web.

The post-buckling behaviour of steel plate girder has been studied by many researchers [2―6]. However, a comparatively little research has been conducted on aluminum alloy plate girders subjected to shear force. Evans and Hamoodi [7] performed twenty-two tests to investigate the

post-buckling behaviour of welded aluminum alloy plate girders. The girders have transverse or longitudinal web stiffeners and are subjected to different combinations of shear and bending loads. It was observed that, although shear sway mechanisms similar to those for steel girders was developed, the webs of aluminum girders may fracture in the heat affected zones (HAZ) adjacent to the welds. It is shown that the tension field theory, originally developed for steel girders, may overestimate the shear-carrying capacity of aluminum girders and it is concluded that the theory requires some modification before it can be applied with confidence to aluminum girders. Based on these experimental results, a finite element model was developed by Cheng et al. [8] to investigate the shear resistance of aluminum alloy plate girders. However, the welding of the aluminum alloy plate girder is not considered. Hence, the influence of the heat affected zone (HAZ) is ignored. It should be noted that heating the material tends to erase the effect of precipitation-heat treatments and strain-hardening, so arc welding, which brings a localized portion of the metal to the melting point, decreases the material's strength at the weld [9].

The objective of this paper is to assess the appropriateness of the shear resistance design rules in the current specifications for aluminum alloy plate girders. An accurate finite element model (FEM) was developed to investigate the behaviour of aluminum alloy plate girders subjected to shear force. The finite element analysis (FEA) program ABAQUS [10] was used for the numerical investigation. The FEM included geometric and material non-linearities. The welding of the aluminum alloy plate girder and the influence of the heat affected zone (HAZ) are considered and carefully modeled. The FEM was verified against the aluminum alloy plate girder tests conducted by Lam [11]. Aluminum alloy plate girders with end posts (web stiffeners) consist of a single plate were investigated. Parametric study was performed to investigate the effect of cross-section geometries on the shear resistance of aluminum alloy plate girder. The test results as well as the shear resistances predicted by the FEA were compared with the design strengths obtained using the European Code [12] and American Specification [13] for aluminum structures. Modifications on the design rules of EC9 [12] Code are made for the proposed design method for shear resistance of aluminum alloy plate girders with end posts.

2.   SUMMARY OF EXPERIMENTAL INVESTIGATION

A test program has been conducted by Lam [11] to investigate the shear behaviour of aluminum alloy plate girders with end posts consisting of a single plate. A total of eight tests of 7020 series and 6082 series aluminum alloy plate girders have been conducted. Both series of 7020 and 6082 aluminum alloy plate girders consist of two panels of equal depth for each specimen. At mid-span between the panels of each girder, a very strong intermediate doubled-sided vertical stiffener was used. Each panel comprised two equal flanges of rectangular cross-section, a rectangular web plate of uniform thickness and an end post consisting of a single plate. The layout and the definition of symbols for an aluminum alloy plate girder are shown in Figure 1. The dimensions and material properties are shown in Table 1.

Prior to testing, one of the panels of the girder was reinforced while the other panel was instrumented for testing. The girder was simply supported at its ends and subjected to a vertical point load which was applied by a servo-controlled hydraulic jack. Each girder was loaded predominantly in shear. During the tests, two different failure modes were observed. The collapse behaviour of the test II-7020 and test II-6082 are similar, but entirely different from the other tests. The failure modes observed for most of the aluminum alloy plate girders of test I, test III and test IV of both series of 7020 and 6082 were mainly shear buckling. Figure 2a shows the failure mode of the test I-7020. The aluminum alloy plate girders failed by buckling in the end post for test II-7020 and test II-6082, as clearly shown in Figure 3a. The severe deformation of the failed end

post can be seen in Figure 3a. In addition to the buckling of the end post, which occurred at a position of about one-third of the height of the post, the web panel has also buckled. The ultimate loads of the aluminum alloy plate girder tests are shown in Table 2. The experimental investigation is detailed in Lam [11].

(a) Front view   (b) End view
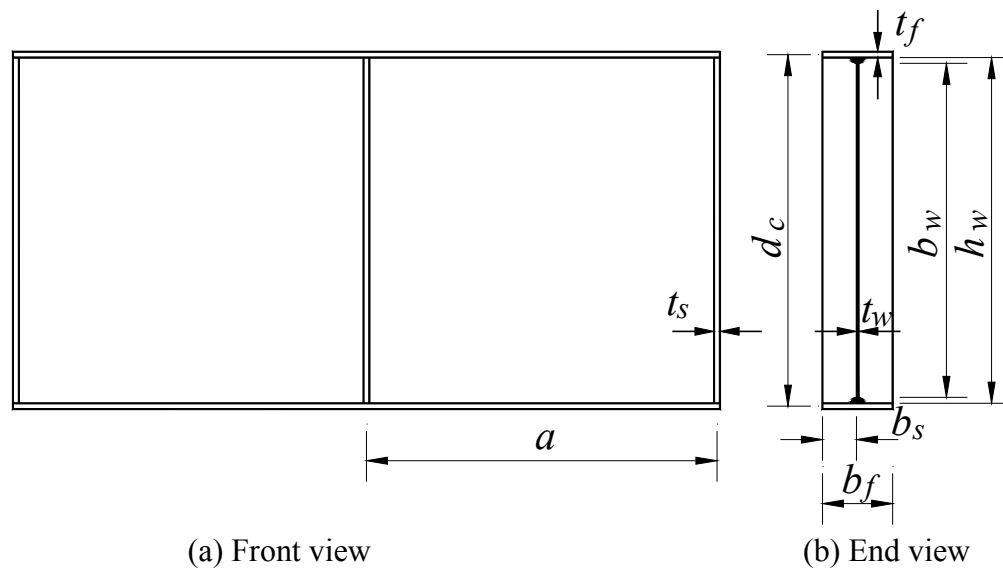
Figure 1. Definition of Symbols
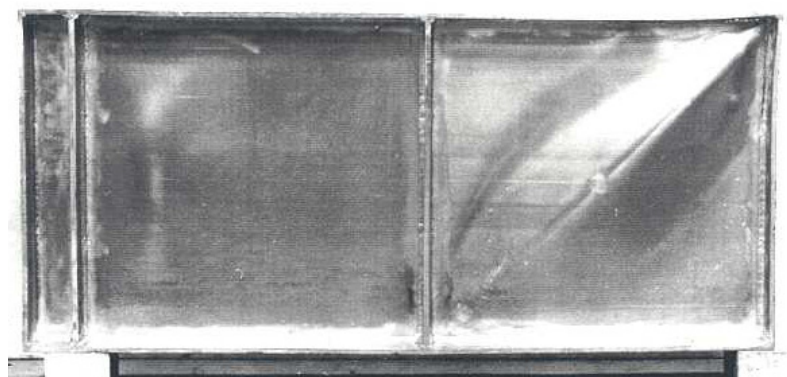
(a) Experiment (Lam 1993)
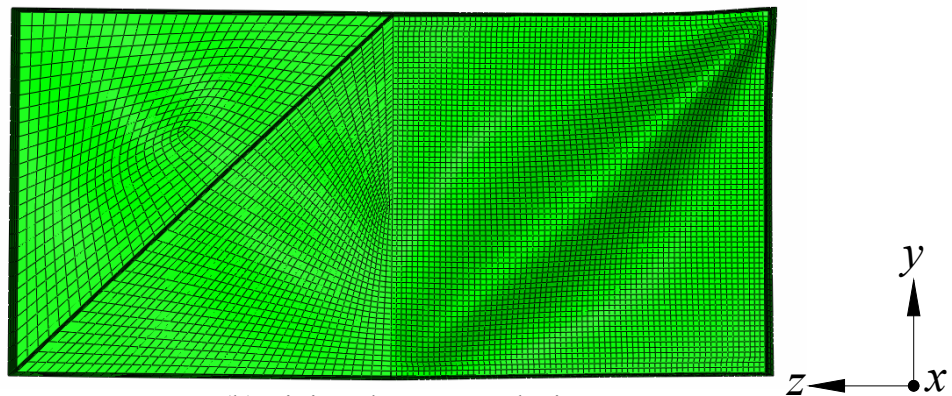
(b) Finite Element Analysis

Figure 2. Comparison of Experimental and Numerical Failure Mode of Specimen Test I −7020

(a) Experiment (Lam 1993)

y

z ← • x
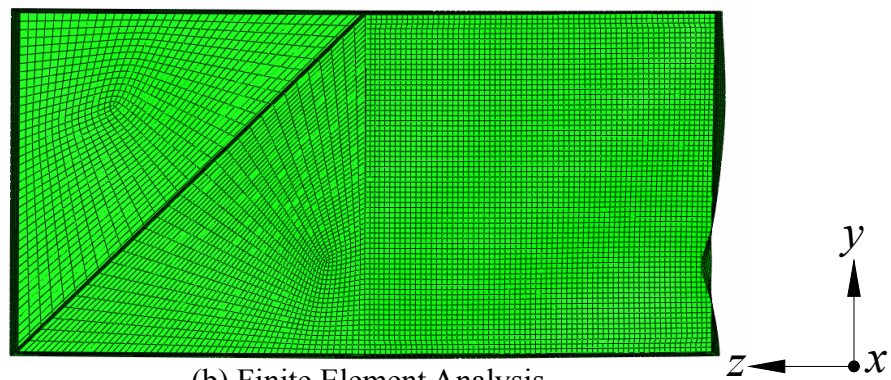
(b) Finite Element Analysis

Figure 3. Comparison of Experimental and Numerical Failure Mode of Specimen Test II −7020

Table 1. Dimensions and Material Properties of Test Specimens (Lam 1993)

Specimen	Series	Web			Space	Flange			Stiffener			Young's modulus
		h_w	t_w	f_w	a	b_f	t_f	f_f	b_s	t_s	f_s	E
		(mm)	(mm)	(MPa)	(mm)	(mm)	(mm)	(MPa)	(mm)	(mm)	(MPa)	(MPa)
Test I	7020	601.0	3.15	334.1	633.2	129.5	9.85	341.6	64.4	9.65	341.6	70400
Test II		598.5	3.15	334.1	630.7	128.7	9.70	341.6	64.5	3.15	334.1	70300
Test III		598.5	3.15	334.1	632.3	129.0	9.69	341.6	65.1	6.26	317.4	70333
Test IV		601.0	3.15	334.1	633.3	129.6	9.84	341.6	55.0	9.55	341.6	70400
Test I	6082	602.0	3.18	245.1	632.8	129.0	9.74	272.5	64.4	9.80	272.5	70000
Test II		600.0	3.18	245.1	630.6	129.0	9.80	272.5	63.7	3.22	245.1	70000
Test III		600.0	3.18	245.1	631.1	129.0	9.80	272.5	64.0	6.43	278.4	70000
Test IV		602.0	3.18	245.1	635.3	129.0	9.74	272.5	54.5	9.80	272.5	70000

Note: b_s shown above is actually half of the b_s shown in the experiments conducted by Lam (1993)

Table 2. Comparison of Numerical Results with Test Results

Specimen	Series	Exp. load per web V_{Exp}	Comparison					
			V_{Exp}/V_{FEA}					
		(kN)	$h_w/100$	$h_w/200$	$h_w/500$	$h_w/1000$	$h_w/3000$	$h_w/6000$
Test I	7020	157.0	1.00	0.99	0.98	0.97	0.97	0.97
Test II		118.5	1.07	1.04	1.03	1.03	1.03	1.03
Test III		152.0	1.05	1.04	1.04	1.03	1.03	1.03
Test IV		156.8	0.96	0.97	0.97	0.98	0.98	0.98
Test I	6082	119.0	0.93	0.94	0.94	0.94	0.94	0.94
Test II		84.5	1.00	0.99	0.98	0.98	0.98	0.98
Test III		113.5	0.97	0.98	0.98	0.98	0.98	0.98
Test IV		134.5	1.05	1.06	1.07	1.08	1.08	1.08
		Mean	1.004	1.001	0.999	0.999	0.999	0.999
		COV	0.049	0.041	0.043	0.045	0.045	0.045

3. NUMERICAL INVESTIGATION

3.1 General

The non-linear finite element analysis program ABAQUS [10] version 6.7 was used to simulate the ultimate loads, web deformations and failure modes of aluminum alloy plate girders with end posts. The finite element simulation consisted of two steps. The first step is linear perturbation analysis, which was performed on a "perfect" geometry to obtain probable elastic buckling modes of the aluminum alloy plate girder. The second step is non-linear analysis by incorporating both geometric and material non-linearities, which was performed to obtain the ultimate load, web deformation and failure mode of the aluminum alloy plate girder.

In the finite element model (FEM), the measured cross-section dimensions, material properties obtained from coupon tests and initial geometric imperfections were used. The model was based on the centerline dimensions of the cross-sections. The welding of the aluminum alloy plate girder and the influence of the heat affected zone (HAZ) were considered and carefully modeled.

3.2 Element Type and Mesh

The four-node doubly curved general-purpose shell elements S4R were used in the finite element analysis (FEA) to model the aluminium alloy plate girder components. It is mentioned in the ABAQUS manual that S4R element is suitable for complex buckling behaviour. The S4R element has six degrees of freedom per node and provides accurate solutions to most applications [10]. Five integration points were taken in the thickness direction. The finite element mesh used in the model was investigated by varying the size of the elements in the cross-section to provide both accurate results and less computational time. The finer mesh size of 8×8mm (length by width) in the HAZ areas and the finite element mesh size of 15×15mm for the rest of the section were used. Figures 2b and 3b show the geometry and the mesh of the plate girders.

3.3.   Boundary Condition and Method of Loading

The aluminum alloy plate girder was simply supported at its end and subjected to a vertical point load. Following the test procedure, the simply supported end boundary conditions were modeled by restraining the translational degrees of freedom in the Y and Z directions at one end and restraining the translational degree of freedom in the Y direction only at the other end.

The loading method used in the FEA was identical to that used in the tests. The displacement control method was used for the analysis of the aluminum alloy plate girder. Vertical point load was applied to the girder by specifying a displacement to the nodes at the center of the girder.

3.4   Material Modelling

As mentioned earlier, the first step of the FEA is a linear analysis where there is a linear relationship between the applied loads and the response of the structure. In this step, the stiffness of the structure remained constant. Hence, only the density, Young's modulus and Poisson's ratio defined the material properties. However, the second step of the FEA is a non-linearity analysis where the stiffness of the structure changed as it deformed. The material non-linearity was incorporated in the FEM by specifying the true values of stresses and strains. The plasticity of the material was simulated by a mathematical model, known as the incremental plasticity model, and the true stress (σ_{true}) and plastic true strain (ε_{true}^{pl}) were specified in ABAQUS [10].

It is well-known that a heat affected zone (HAZ) develops in an aluminum alloy plate girder adjacent to the welds. In the HAZ, the strength varies from a minimum at the weld to the full strength of the virgin material at a certain distance away from the weld. The welding of the aluminum alloy plate girder and the influence of the heat affected zone (HAZ) are also considered and carefully modeled in this study. The extent of the HAZ and material properties of the HAZ are predicted according to EC9 Code [12], then modeled accordingly in the FEM.

4.   SENSITIVITY ANALYSIS AND VERIFICATION OF FINITE ELEMENT MODEL

A sensitivity analysis on geometric imperfections of the aluminum alloy plate girders was performed for both series of 7020 and 6082 to determine the most appropriate scale factor for the finite element model (FEM). A number of scale factors expressed in terms of 1/100, 1/200, 1/500, 1/1000, 1/3000 and 1/6000 of the depth of the web between the flanges (h_w) were investigated. The results of the sensitivity analysis are shown in Table 2, in which, V_{Exp} is the experimental ultimate load, and V_{FEA} is the ultimate load predicted by the FEA. It is shown that using the scale factors of 1/100, 1/200, 1/500, 1/1000, 1/3000 and 1/6000 of the depth of the web between the flanges (h_w) provide good predictions compared with the experimental results. The results obtained for different scale factors are relatively close. Generally, the scale factor of 1/200 of the depth of the web between the flanges provides the best predictions for both series of 7020 and 6082 in terms of the mean value and coefficient of variation (COV). Hence, a scale factor of $h_w/200$ was chosen for the verification of the finite element model as well as for the parametric study.

In the verification of the developed FEM, a total of eight aluminum alloy plate girders subjected to shear force were analyzed. A comparison between the experimental results and the finite element results was carried out. The main objective of this comparison is to verify and check the accuracy of the finite element model. The comparison of the test results (V_{Exp}) with the shear resistance of aluminum alloy plate girders (V_{FEA}) predicted by the FEA is shown in Table 2.   It can be seen that good agreement has been achieved between both results for all specimens where a scale factor of

1/200 of the depth of the web between the flanges was used in modeling the geometric imperfections of the aluminum alloy plate girders. A maximum difference of 6% was observed between the experimental and numerical results for specimens Test I-6082 and Test IV-6082. The mean value of the V_{Exp}/V_{FEA} ratio is 1.001 with the corresponding coefficient of variation (COV) of 0.041.

Two different failure modes were observed from the tests and also verified by the finite element model, as shown in Figures 2 and 3. The failure mode of the tests II-7020 and test II-6082 is entirely different from the other tests as mentioned in the Summary of Experimental Investigation Section. A typical comparison of the load-web deformation curves between experimental and finite element analysis for specimen test I-7020 is shown in Figure 4. It is shown that both the failure modes and the load-web deformation curves reflect good agreement between the experimental and finite element results.
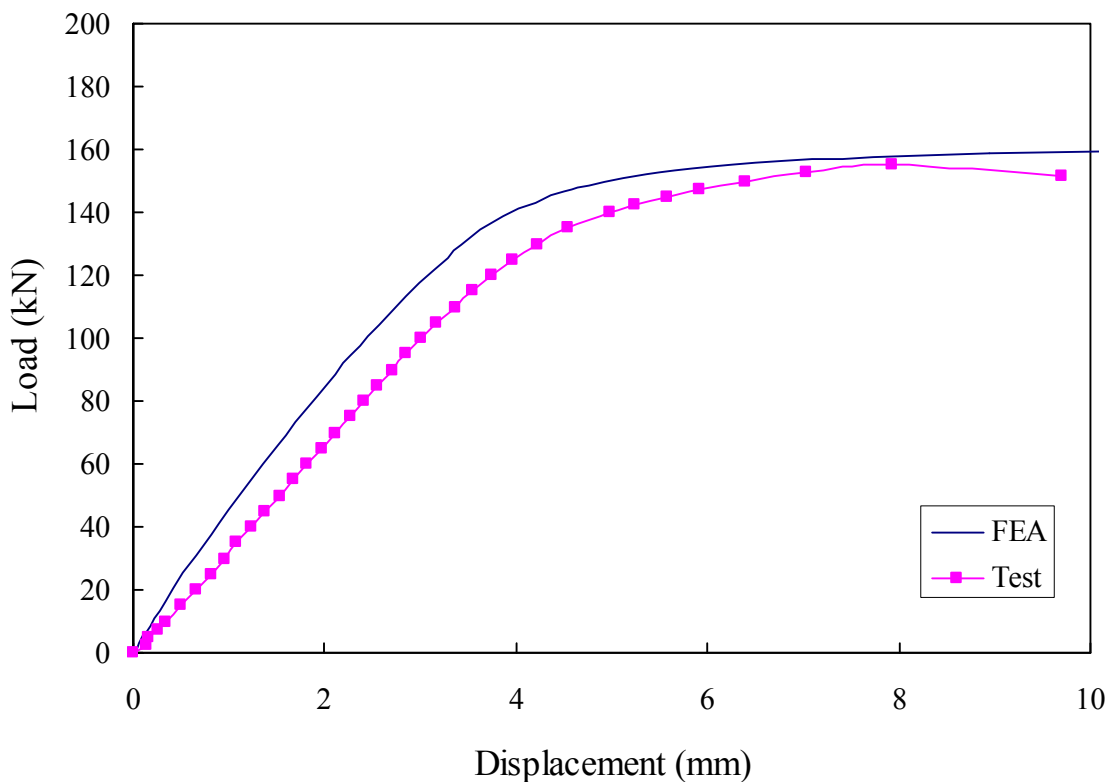
Figure 4. Comparison of Experimental and Numerical Load-web Deformation Curves
for Specimen Test I – 7020

5.   PARAMETRIC STUDY

It is shown that the FEM closely predicted the shear behaviour of aluminum alloy plate girders with end posts consisting of a single plate. Hence, parametric study was carried out to study the effects of cross-section geometries on the shear ultimate load of aluminum alloy plate girder. A total of 118 specimens in 4 Groups were analyzed in the parametric study. In Group 1, 35 specimens were analyzed to investigate the effects of web on the shear behaviour of aluminum alloy plate girder. The dimensions of web varied and the web slenderness (h_w/t_w) ranged from 98 to 393 while the dimensions of flange and stiffener were kept constant, as shown in Table 3. Five different aspect ratios (a/b_w) were investigated in this study. In Group 2, 40 specimens were analyzed to investigate the effects of bending rigidity of flange on the collapse behaviour of aluminum alloy plate girder.

The dimensions of flange and web varied and four different flange-to-web thickness ratios (t_f/t_w) of 2, 3, 4 and 5 were investigated, while the dimensions of stiffener were kept constant, as shown in Table 4. In Group 3, 36 specimens were analyzed to investigate the effects of bending rigidity of stiffener on the collapse behaviour of aluminum alloy plate girder. The dimensions of stiffener and web varied and four different stiffener-to-web thickness ratios (t_s/t_w) of 2, 3, 4 and 5 were investigated, while the dimensions of flange were kept constant, as shown in Table 5. The half width of stiffener (b_s) was also investigated in Group 4, as shown in Table 6, where 7 specimens with half width of stiffeners were analyzed. The material properties of test specimen of Test II-6082 were used in the parametric study.

Table 3. Cross-section Dimensions of Parametric Study for Group 1

Specimen	Web			Space		Flange		Stiffener	
	d_c	t_w	h_w/t_w	a	a/b_w	b_f	t_f	b_s	t_s
	(mm)	(mm)		(mm)		(mm)	(mm)	(mm)	(mm)
G1-T1.5-A0.5	600	1.5	393	300	0.56	200	10	100	10
G1-T1.5-A1.0	600	1.5	393	600	1.11	200	10	100	10
G1-T1.5-A2.0	600	1.5	393	1200	2.22	200	10	100	10
G1-T1.5-A3.0	600	1.5	393	1800	3.33	200	10	100	10
G1-T1.5-A4.0	600	1.5	393	2400	4.44	200	10	100	10
G1-T2.0-A0.5	600	2.0	295	300	0.56	200	10	100	10
G1-T2.0-A1.0	600	2.0	295	600	1.11	200	10	100	10
G1-T2.0-A2.0	600	2.0	295	1200	2.22	200	10	100	10
G1-T2.0-A3.0	600	2.0	295	1800	3.33	200	10	100	10
G1-T2.0-A4.0	600	2.0	295	2400	4.44	200	10	100	10
G1-T2.5-A0.5	600	2.5	236	300	0.56	200	10	100	10
G1-T2.5-A1.0	600	2.5	236	600	1.11	200	10	100	10
G1-T2.5-A2.0	600	2.5	236	1200	2.22	200	10	100	10
G1-T2.5-A3.0	600	2.5	236	1800	3.33	200	10	100	10
G1-T2.5-A4.0	600	2.5	236	2400	4.44	200	10	100	10
G1-T3.0-A0.5	600	3.0	197	300	0.56	200	10	100	10
G1-T3.0-A1.0	600	3.0	197	600	1.11	200	10	100	10
G1-T3.0-A2.0	600	3.0	197	1200	2.22	200	10	100	10
G1-T3.0-A3.0	600	3.0	197	1800	3.33	200	10	100	10
G1-T3.0-A4.0	600	3.0	197	2400	4.44	200	10	100	10
G1-T4.0-A0.5	600	4.0	148	300	0.56	200	10	100	10
G1-T4.0-A1.0	600	4.0	148	600	1.11	200	10	100	10
G1-T4.0-A2.0	600	4.0	148	1200	2.22	200	10	100	10
G1-T4.0-A3.0	600	4.0	148	1800	3.33	200	10	100	10
G1-T4.0-A4.0	600	4.0	148	2400	4.44	200	10	100	10
G1-T6.0-A0.5	600	6.0	98	300	0.56	200	10	100	10
G1-T6.0-A1.0	600	6.0	98	600	1.11	200	10	100	10
G1-T6.0-A2.0	600	6.0	98	1200	2.22	200	10	100	10
G1-T6.0-A3.0	600	6.0	98	1800	3.33	200	10	100	10
G1-T6.0-A4.0	600	6.0	98	2400	4.44	200	10	100	10
G1-T12.0-A0.5	600	12.0	49	300	0.56	200	10	100	10
G1-T12.0-A1.0	600	12.0	49	600	1.11	200	10	100	10
G1-T12.0-A2.0	600	12.0	49	1200	2.22	200	10	100	10
G1-T12.0-A3.0	600	12.0	49	1800	3.33	200	10	100	10
G1-T12.0-A4.0	600	12.0	49	2400	4.44	200	10	100	10

Table 4. Cross-section Dimensions of Parametric Study for Group 2

Specimen	Web			Space		Flange		Stiffener	
	d_c	t_w	h_w/t_w	a	a/b_w	b_f	t_f	b_s	t_s
	(mm)	(mm)		(mm)		(mm)	(mm)	(mm)	(mm)
G2-T1.5-F2-A1.0	600	1.5	398	600	1.10	200	3.0	100	10
G2-T1.5-F3-A1.0	600	1.5	397	600	1.10	200	4.5	100	10
G2-T1.5-F4-A1.0	600	1.5	396	600	1.10	200	6.0	100	10
G2-T1.5-F5-A1.0	600	1.5	395	600	1.11	200	7.5	100	10
G2-T2.0-F2-A1.0	600	2.0	298	600	1.10	200	4.0	100	10
G2-T2.0-F3-A1.0	600	2.0	297	600	1.10	200	6.0	100	10
G2-T2.0-F4-A1.0	600	2.0	296	600	1.11	200	8.0	100	10
G2-T2.0-F5-A1.0	600	2.0	295	600	1.11	200	10.0	100	10
G2-T2.5-F2-A1.0	600	2.5	238	600	1.10	200	5.0	100	10
G2-T2.5-F3-A1.0	600	2.5	237	600	1.11	200	7.5	100	10
G2-T2.5-F4-A1.0	600	2.5	236	600	1.11	200	10.0	100	10
G2-T2.5-F5-A1.0	600	2.5	235	600	1.12	200	12.5	100	10
G2-T3.0-F2-A1.0	600	3.0	198	600	1.10	200	6.0	100	10
G2-T3.0-F3-A1.0	600	3.0	197	600	1.11	200	9.0	100	10
G2-T3.0-F4-A1.0	600	3.0	196	600	1.12	200	12.0	100	10
G2-T3.0-F5-A1.0	600	3.0	195	600	1.12	200	15.0	100	10
G2-T6.0-F2-A1.0	600	6.0	98	600	1.12	200	12.0	100	10
G2-T6.0-F3-A1.0	600	6.0	97	600	1.13	200	18.0	100	10
G2-T6.0-F4-A1.0	600	6.0	96	600	1.14	200	24.0	100	10
G2-T6.0-F5-A1.0	600	6.0	95	600	1.15	200	30.0	100	10
G2-T1.5-F2-A2.0	600	1.5	398	1200	2.19	200	3.0	100	10
G2-T1.5-F3-A2.0	600	1.5	397	1200	2.20	200	4.5	100	10
G2-T1.5-F4-A2.0	600	1.5	396	1200	2.21	200	6.0	100	10
G2-T1.5-F5-A2.0	600	1.5	395	1200	2.21	200	7.5	100	10
G2-T2.0-F2-A2.0	600	2.0	298	1200	2.20	200	4.0	100	10
G2-T2.0-F3-A2.0	600	2.0	297	1200	2.21	200	6.0	100	10
G2-T2.0-F4-A2.0	600	2.0	296	1200	2.21	200	8.0	100	10
G2-T2.0-F5-A2.0	600	2.0	295	1200	2.22	200	10.0	100	10
G2-T2.5-F2-A2.0	600	2.5	238	1200	2.20	200	5.0	100	10
G2-T2.5-F3-A2.0	600	2.5	237	1200	2.21	200	7.5	100	10
G2-T2.5-F4-A2.0	600	2.5	236	1200	2.22	200	10.0	100	10
G2-T2.5-F5-A2.0	600	2.5	235	1200	2.23	200	12.5	100	10
G2-T3.0-F2-A2.0	600	3.0	198	1200	2.21	200	6.0	100	10
G2-T3.0-F3-A2.0	600	3.0	197	1200	2.22	200	9.0	100	10
G2-T3.0-F4-A2.0	600	3.0	196	1200	2.23	200	12.0	100	10
G2-T3.0-F5-A2.0	600	3.0	195	1200	2.24	200	15.0	100	10
G2-T6.0-F2-A2.0	600	6.0	98	1200	2.23	200	12.0	100	10
G2-T6.0-F3-A2.0	600	6.0	97	1200	2.26	200	18.0	100	10
G2-T6.0-F4-A2.0	600	6.0	96	1200	2.28	200	24.0	100	10
G2-T6.0-F5-A2.0	600	6.0	95	1200	2.31	200	30.0	100	10

Table 5. Cross-section Dimensions of Parametric Study for Group 3

Specimen	Web			Space		Flange		Stiffener	
	d_c	t_w	h_w/t_w	a	a/b_w	b_f	t_f	b_s	t_s
	(mm)	(mm)		(mm)		(mm)	(mm)	(mm)	(mm)
G3-T2.0-S2-A0.5	600	2.0	295	300	0.56	200	10	100	4.0
G3-T2.0-S3-A0.5	600	2.0	295	300	0.56	200	10	100	6.0
G3-T2.0-S4-A0.5	600	2.0	295	300	0.56	200	10	100	8.0
G3-T2.0-S5-A0.5	600	2.0	295	300	0.56	200	10	100	10.0
G3-T2.5-S2-A0.5	600	2.5	236	300	0.56	200	10	100	5.0
G3-T2.5-S3-A0.5	600	2.5	236	300	0.56	200	10	100	7.5
G3-T2.5-S4-A0.5	600	2.5	236	300	0.56	200	10	100	10.0
G3-T2.5-S5-A0.5	600	2.5	236	300	0.56	200	10	100	12.5
G3-T3.0-S2-A0.5	600	3.0	197	300	0.56	200	10	100	6.0
G3-T3.0-S3-A0.5	600	3.0	197	300	0.56	200	10	100	9.0
G3-T3.0-S4-A0.5	600	3.0	197	300	0.56	200	10	100	12.0
G3-T3.0-S5-A0.5	600	3.0	197	300	0.56	200	10	100	15.0
G3-T6.0-S2-A0.5	600	6.0	98	300	0.56	200	10	100	12.0
G3-T6.0-S3-A0.5	600	6.0	98	300	0.56	200	10	100	18.0
G3-T6.0-S4-A0.5	600	6.0	98	300	0.56	200	10	100	24.0
G3-T6.0-S5-A0.5	600	6.0	98	300	0.56	200	10	100	30.0
G3-T1.5-S2-A1.0	600	1.5	393	600	1.11	200	10	100	3.0
G3-T1.5-S3-A1.0	600	1.5	393	600	1.11	200	10	100	4.5
G3-T1.5-S4-A1.0	600	1.5	393	600	1.11	200	10	100	6.0
G3-T1.5-S5-A1.0	600	1.5	393	600	1.11	200	10	100	7.5
G3-T2.0-S2-A1.0	600	2.0	295	600	1.11	200	10	100	4.0
G3-T2.0-S3-A1.0	600	2.0	295	600	1.11	200	10	100	6.0
G3-T2.0-S4-A1.0	600	2.0	295	600	1.11	200	10	100	8.0
G3-T2.0-S5-A1.0	600	2.0	295	600	1.11	200	10	100	10.0
G3-T2.5-S2-A1.0	600	2.5	236	600	1.11	200	10	100	5.0
G3-T2.5-S3-A1.0	600	2.5	236	600	1.11	200	10	100	7.5
G3-T2.5-S4-A1.0	600	2.5	236	600	1.11	200	10	100	10.0
G3-T2.5-S5-A1.0	600	2.5	236	600	1.11	200	10	100	12.5
G3-T3.0-S2-A1.0	600	3.0	197	600	1.11	200	10	100	6.0
G3-T3.0-S3-A1.0	600	3.0	197	600	1.11	200	10	100	9.0
G3-T3.0-S4-A1.0	600	3.0	197	600	1.11	200	10	100	12.0
G3-T3.0-S5-A1.0	600	3.0	197	600	1.11	200	10	100	15.0
G3-T6.0-S2-A1.0	600	6.0	98	600	1.11	200	10	100	12.0
G3-T6.0-S3-A1.0	600	6.0	98	600	1.11	200	10	100	18.0
G3-T6.0-S4-A1.0	600	6.0	98	600	1.11	200	10	100	24.0
G3-T6.0-S5-A1.0	600	6.0	98	600	1.11	200	10	100	30.0

Table 6. Cross-section Dimensions of Parametric Study for Group 4

Specimen	Web			Space		Flange		Stiffener	
	d_c	t_w	h_w/t_w	a	a/b_w	b_f	t_f	b_s	t_s
	(mm)	(mm)		(mm)		(mm)	(mm)	(mm)	(mm)
G4-T1.5	600	1.5	393	600	1.11	200	10	50	10
G4-T2.0	600	2.0	295	600	1.11	200	10	50	10
G4-T2.5	600	2.5	236	600	1.11	200	10	50	10
G4-T3.0	600	3.0	197	600	1.11	200	10	50	10
G4-T4.0	600	4.0	148	600	1.11	200	10	50	10
G4-T6.0	600	6.0	98	600	1.11	200	10	50	10
G4-T12.0	600	12.0	49	600	1.11	200	10	50	10

6. DISCUSSION

The web slenderness (h_w/t_w) has significant effect on the shear resistance of aluminum alloy plate girder, as shown in Figure 5, where the vertical axis of the graph shows the normalized shear resistance ($\rho = V / \left(t_w h_w f_w / \sqrt{3} \right)$) and the horizontal axis of the graph shows the web slenderness (h_w/t_w). Five different aspect ratios (a/b_w) of 0.56, 1.11, 2.22, 3.33 and 4.44 are considered. It is shown that the normalized shear resistance decreases as the web slenderness increases.

It is known that when the web is in the post-buckling range, a load-carrying mechanism is developed, whereby any additional shear load is carried by an inclined tensile membrane stress field. This tensile field anchors against the top and bottom flanges and against the transverse stiffener on either side of the web panel. Hence, the effects of the bending rigidity of the flanges and the non-rigid end post are also investigated in this study. Figures 6 and 7 show the effect of the bending rigidity of the flanges on the shear resistance of aluminum alloy plate girders for the case of the aspect ratios $a/b_w = 1.11$ and 2.22, respectively. It is shown that the bending rigidity of the flanges has significant effect on the shear resistance of aluminum alloy plate girder.

In order to study the effect of the non-rigid end post, the shear resistances of some aluminum alloy plate girders with different dimensions of non-rigid end post were calculated. Figures 8 and 9 show the effect of the non-rigid end post on the shear resistance of aluminum alloy plate girders for the case of the aspect ratios $a/b_w = 0.56$ and 1.11, respectively. The ratio of shear resistance of aluminum plate girders with half width of stiffeners to that of aluminum alloy plate girders with full width of stiffeners ($V(0.5bs)/V(bs)$) against the web slenderness (h_w/t_w) is plotted in Figure 10. It is shown that the non-rigid end post has significant effect on the shear resistance of aluminum alloy plate girder.
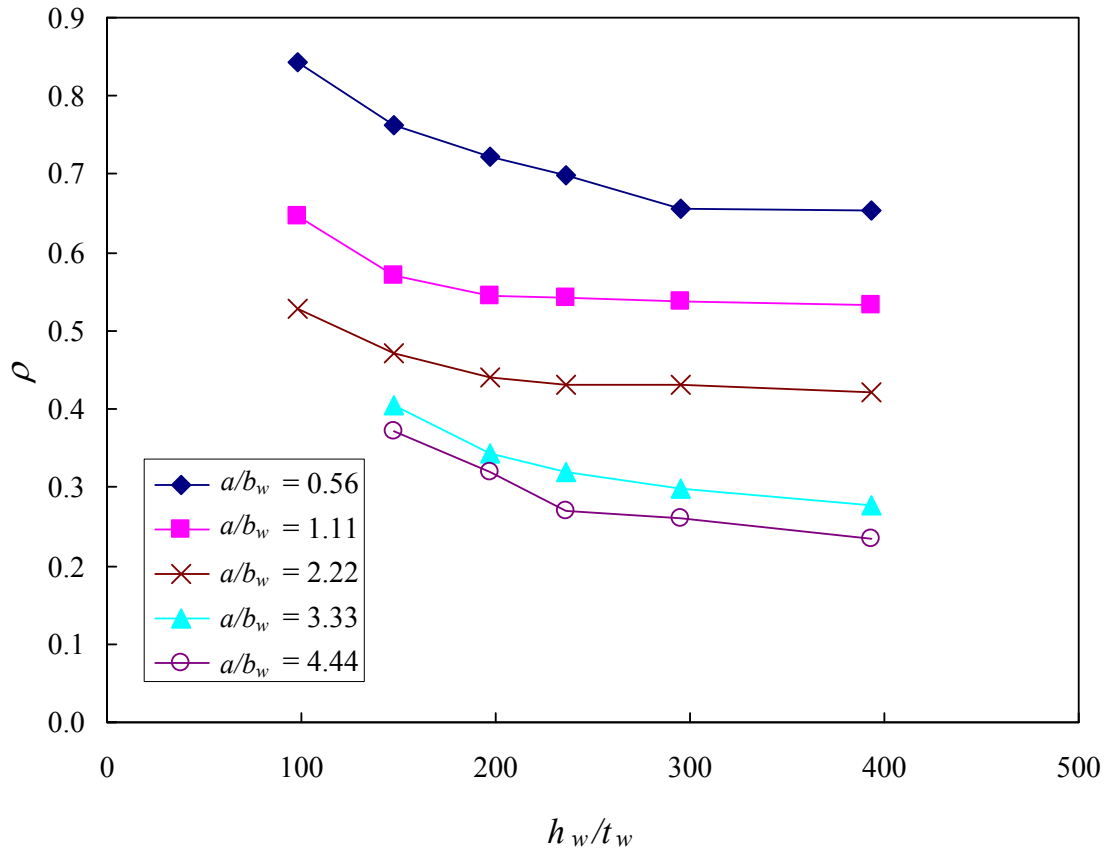
Figure 5. The Effect of Web Slenderness
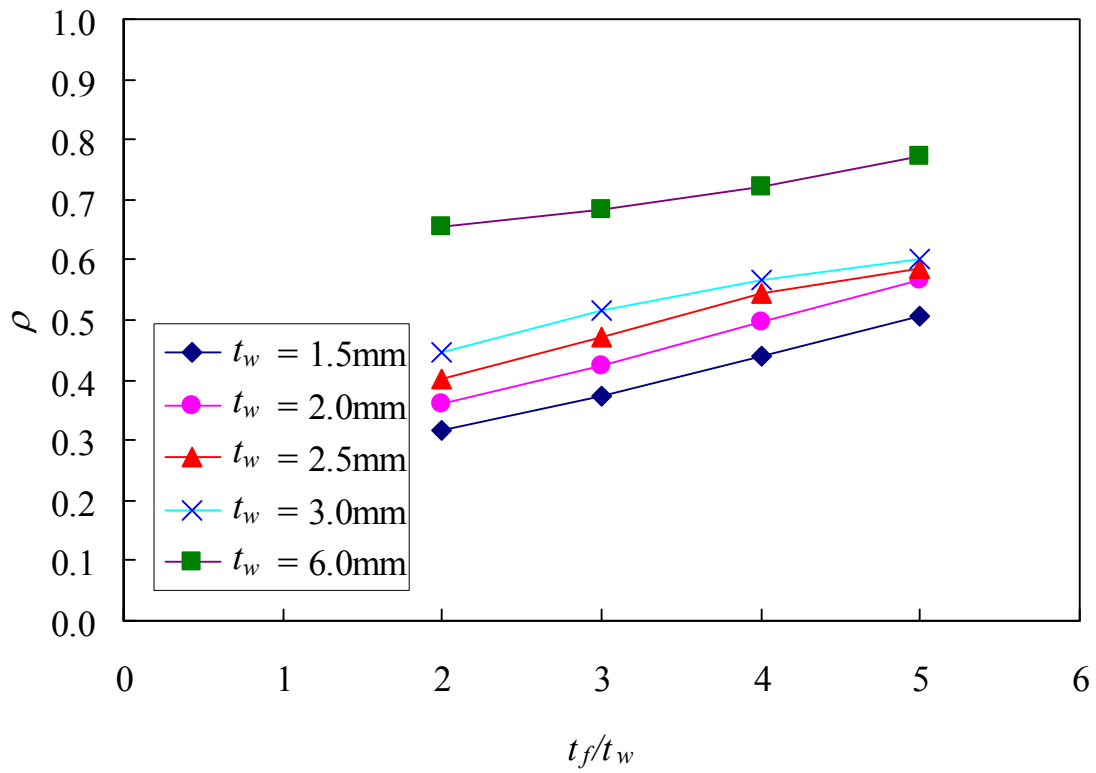
Figure 6. The Effect of Bending Rigidity of the Flange (Aspect Ratio $a/b_w = 1.11$)
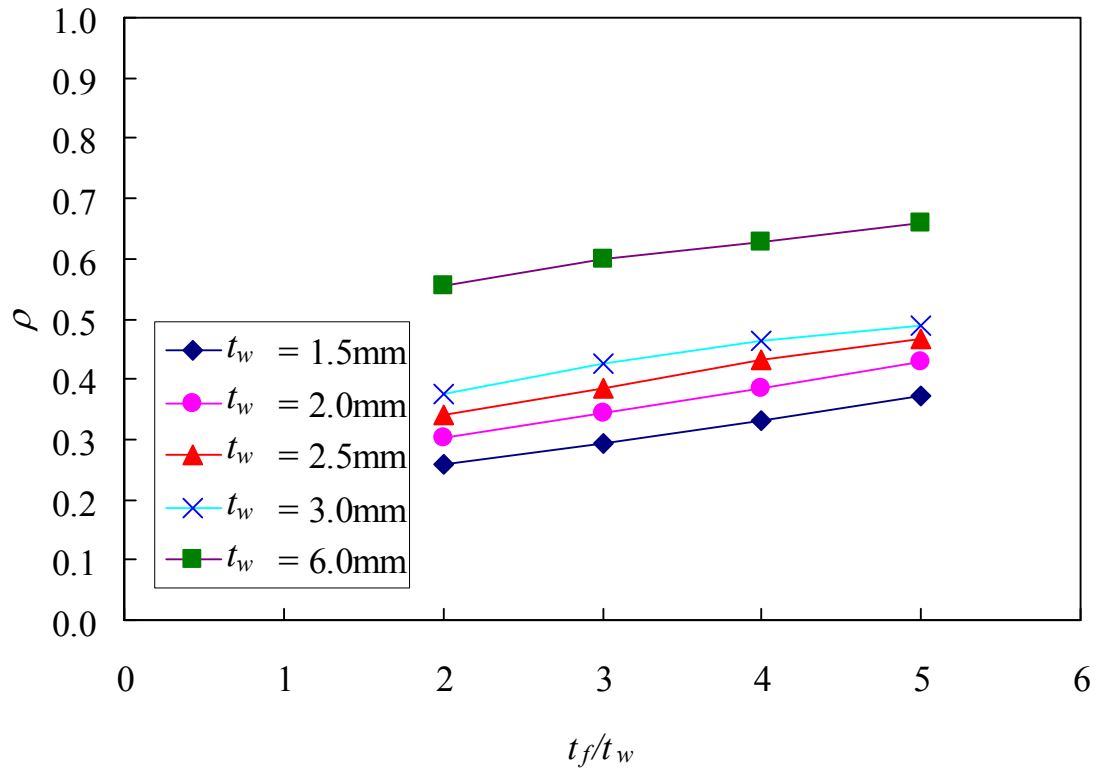
Figure 7. The Effect of Bending Rigidity of the Flange (Aspect Ratio $a/b_w = 2.22$)
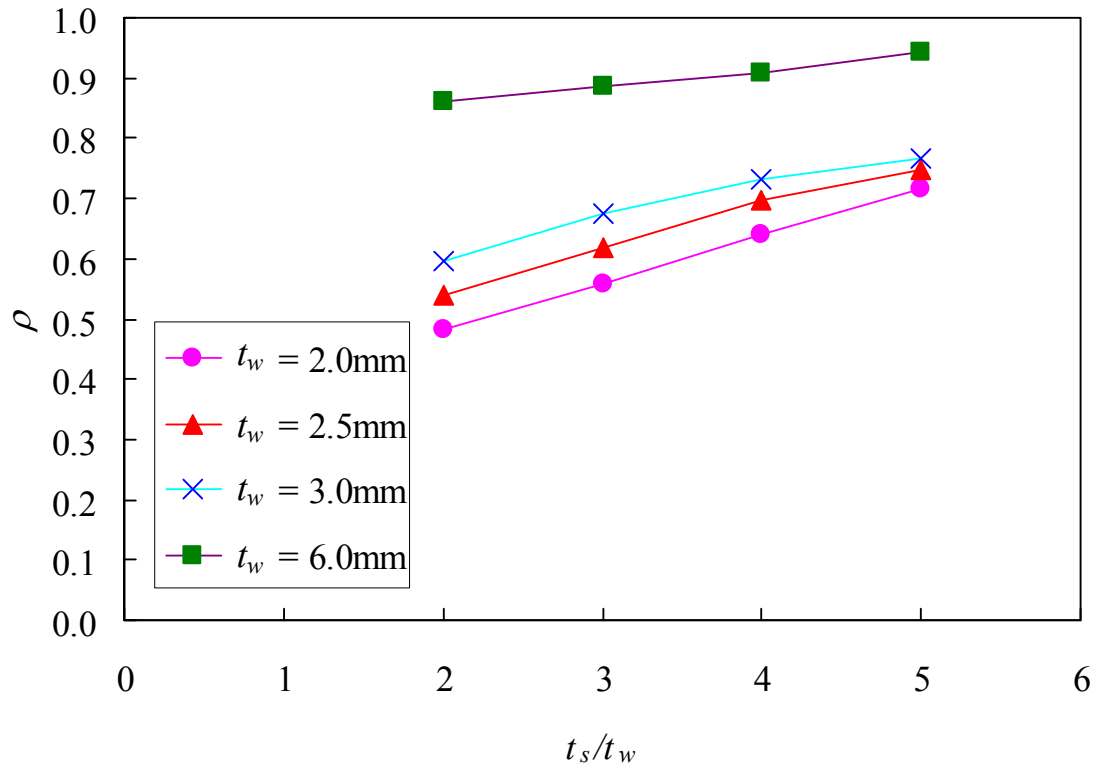
Figure 8. The Effect of Non-rigid End Post (Aspect Ratio $a/b_w = 0.56$)
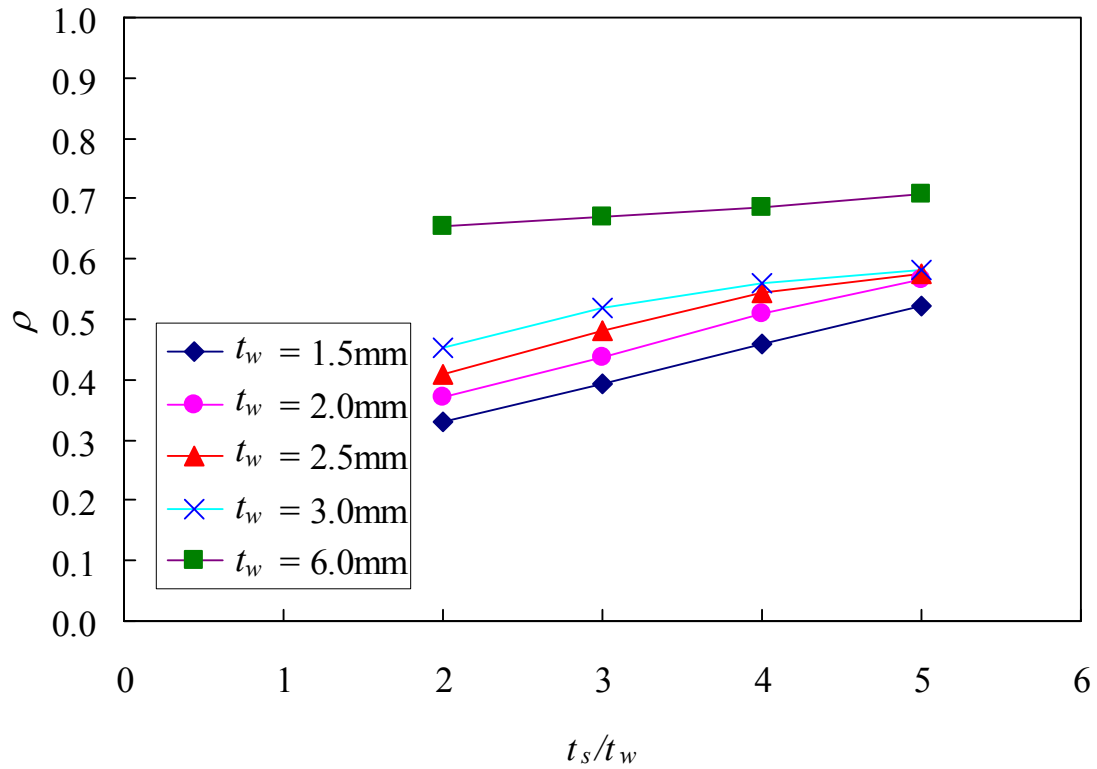
Figure 9. The Effect of Non-rigid End Post (Aspect Ratio $a/b_w = 1.11$)
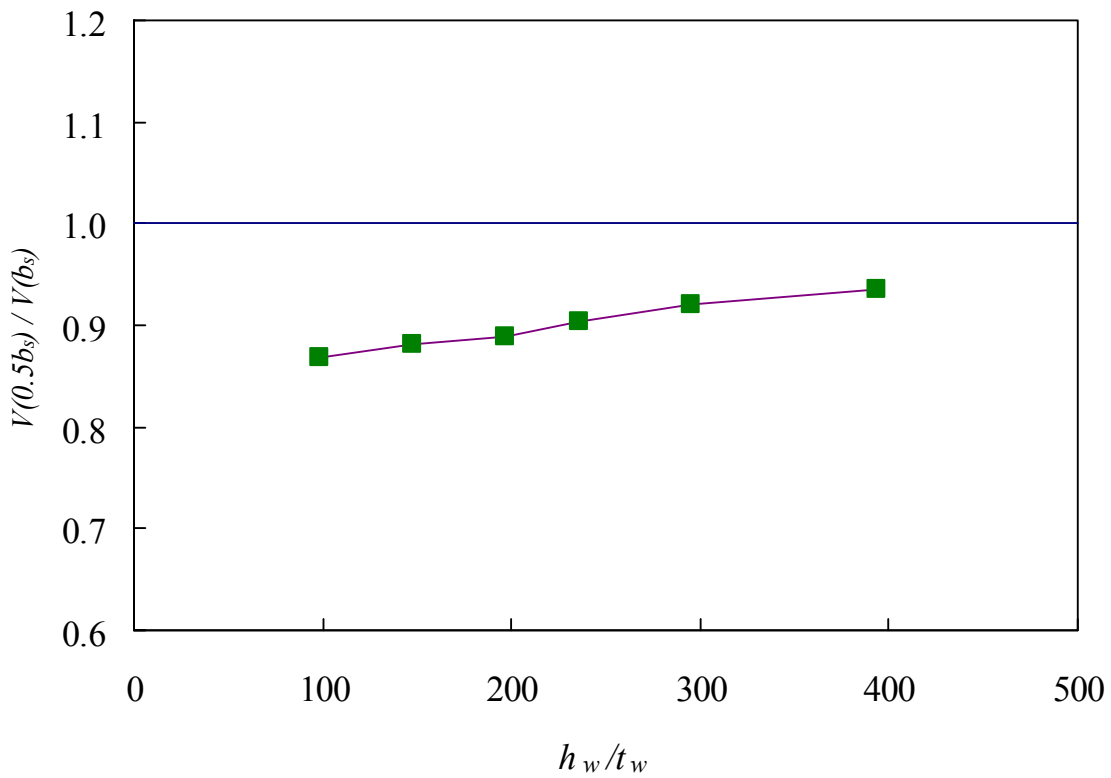
Figure 10. Comparison of Shear Strengths with Different Widths of Non-rigid End Post
(Aspect Ratio $a/b_w = 1.11$)

7.   DESIGN RULES

The current EC9 Code [12] and AA Specification [13] are used to predict the shear resistance of aluminum alloy plate girders. It should be noted that the end posts consisting of a single plate is belonged to the non-rigid end post. In EC9 Code, the shear design resistance V_{EC} of aluminum alloy plate girder with web stiffeners is the sum of the contribution $V_{w,EC}$ of the web and $V_{f,EC}$ of the flanges.

$$V_{EC} = V_{w,EC} + V_{f,EC} \tag{1}$$

where $V_{w,EC}$ includes partial tension field action in the web according to Eqs. 2 – 5 and $V_{f,EC}$ is an increase of the tension field caused by local bending resistance of the flanges according to Eqs. 6 – 7.

$$V_{w,EC} = \rho_v t_w h_w \frac{f_w}{\sqrt{3}} \tag{2}$$

where ρ_v is a factor for shear buckling obtained from the Table 7, t_w is the web thickness, h_w is the web depth between flanges and f_w is the tensile yield stress of the web material. The slenderness parameter λ_w is defined as:

$$\lambda_w = \frac{0.81}{\sqrt{k_\tau}} \frac{b_w}{t_w} \sqrt{\frac{f_w}{E}} \tag{3}$$

where

$$k_\tau = 5.34 + 4.00(b_w/a)^2 \qquad \text{when } a/b_w \geq 1 \tag{4}$$

$$k_\tau = 4.00 + 5.34(b_w/a)^2 \qquad \text{when } a/b_w < 1 \quad (5)$$

in which, b_w is the depth of straight portion of a web excluding the welds, a is the distance between transverse stiffeners and E is the Young's modulus of the aluminum alloy material.

If the flange resistance is not completely utilized in withstanding the bending moment, then the shear resistance contribution $V_{f,EC}$ from the flanges may be included in the shear buckling resistance as follows:

$$V_{f,EC} = \frac{b_f t_f^2 f_f}{c} \left(1 - \left(\frac{M_{Ed}}{M_{f,BS}} \right)^2 \right) \tag{6}$$

where b_f is the flange width, t_f is the flange thickness, f_f is the yield stress of the flange material, M_{Ed} is the design bending moment and $M_{f,BS}$ is the design moment resistance of a cross-section considering the flanges only.

$$c = a \left(0.08 + \frac{4.4 b_f t_f^2 f_f}{t_w b_w^2 f_w} \right) \tag{7}$$

In AA Specification, the shear design stress ($f_{v,AA}$) of stiffened flat elements supported on both edges is defined as follows:

$$f_{v,AA} = f_w / \sqrt{3} \qquad\qquad \text{for } a_e/t_w \leq \text{S}_1 \qquad\qquad (8)$$

$$f_{v,AA} = 1.375\left[B_s - 1.25D_s \frac{a_e}{t} \right] \qquad \text{for } \text{S}_1 < a_e/t_w \leq \text{S}_2 \qquad\qquad (9)$$

$$f_{v,AA} = \frac{1.375\pi^2 E}{(1.25a_e/t)^2} \qquad\qquad \text{for } \text{S}_2 < a_e/t_w \qquad\qquad (10)$$

where, $a_e = \dfrac{a_1}{\sqrt{1+0.7(a_1/a_2)^2}}$, a_1 is shorter dimension of rectangular panel, a_2 is longer dimension

of rectangular panel, $S_1 = \dfrac{B_s - \dfrac{f_w}{1.375\sqrt{3}}}{1.25D_s}$ and $\text{S}_2 = a_e/t_w$ at the intersection of Eqs. 9 and 10. The

term B_s and D_s are defined in the AA Specification as:

$$B_s = \frac{f_w}{\sqrt{3}}\left[1 + \frac{\left(f_w/\sqrt{3}\right)^{1/3}}{17.7} \right] \qquad\qquad (11)$$

$$D_s = \frac{B_s}{10}\left(\frac{B_s}{E} \right)^{1/2} \qquad\qquad (12)$$

Table 7. Factor ρ_v for Shear Buckling

BS EN 1999-1-1		Proposed	
Range of λ_w	Non-rigid end post	Range of λ_w	Non-rigid end post
$\lambda_w \leq 0.83/\eta$	η	$\lambda_w \leq 0.83/\eta$	η
$0.83/\eta \leq \lambda_w < 0.937$	$0.83/\lambda_w$	$0.83/\eta \leq \lambda_w < 2.3$	$0.72/\lambda_w$
$0.937 \leq \lambda_w$	$0.83/\lambda_w$	$2.3 \leq \lambda_w$	$1.8/(3.4+\lambda_w)$

$\eta = 0.7 + 0.35 f_{aw}/f_{ow}$ but not more than 1.2 where f_{aw} is the ultimate strength of the web material and f_{ow} is the strength for overall yielding.

8.   RELIABILITY ANALYSIS

The reliability of the design rules for aluminum alloy plate girders subject to shear force is evaluated using reliability analysis. The reliability index (β) is a relative measure of the safety of the design. A target reliability index of 2.5 for aluminum alloy plate girders is recommended as a lower limit in the AA Specification [13]. The design rules are considered to be reliable if the reliability index is greater than 2.5. The resistance (capacity) factor (ϕ_{v1}) for shear resistance as

recommended by the current EC9 Code [12] and AA Specification [13] are shown in Tables 8 − 11. The load combinations of 1.35DL + 1.5LL and 1.2DL + 1.6LL as specified in the European Code and the American Society of Civil Engineers Standard [14], respectively, were used in the reliability analysis, where DL is the dead load and LL is the live load. The statistical parameters are obtained from the AA Specification for aluminum alloy plate girders subjected to shear force, where $M_m = 1.10$, $F_m = 1.00$, $V_M = 0.06$, and $V_F = 0.05$, which are the mean values and coefficients of variation for material properties and fabrication factors. The statistical parameters U_m and U_P are the mean value and coefficient of variation of load ratio, respectively, as shown in Tables 8 − 11. In calculating the reliability index, the correction factor in the AA Specification was used. The respective resistance factor (ϕ_{v1}) and load combinations for the current EC9 Code and AA Specification were used to calculate the corresponding reliability index (β_1). For the purpose of direct comparison, a constant resistant factor (ϕ_{v2}) of 0.8 and a load combination of 1.2DL + 1.6LL as specified in the AA Specification were used to calculate the reliability index (β_2) for the EC9 Code and AA Specification, as shown in Tables 8−11. Reliability analysis is detailed in the AA Specification [13].

9.   COMPARISON OF EXPERIMENTAL AND NUMERICAL RESULTS WITH CURRENT DESIGN STRENGTHS

The shear ultimate loads (V_{Exp}) obtained from the tests and the shear strengths (V_{FEA}) predicted by the finite element analysis were compared with the nominal shear resistances predicted using the EC9 Code [12] and AA Specification [13]. Tables 8 − 11 show the comparison of the test results (V_{Exp}) and the shear strengths (V_{FEA}) predicted by the FEA with the unfactored design strengths. The design strengths were calculated using the measured cross-section dimensions of each specimen and the measured material properties.

The design strengths predicted by the EC9 Code are generally conservative but not reliable, except for Group 2 where the mean value of the load ratio V/V_{EC} is 1.38 with the corresponding coefficient of variation (COV) of 0.181 and the reliability index $\beta_1 = 3.06$ and $\beta_2 = 3.62$, as shown in Table 9. For AA Specification, the design strengths are generally very conservative. The maximum mean value of the load ratio V/V_{AA} is 4.11 with the corresponding COV of 0.642 and the reliability indices (β_1 and β_2) of 3.05, as shown in Table 9.

10.   MODIFIED DESIGN METHOD

Modifications on the design rules of EC9 Code are made for the design of aluminum alloy plate girder with end posts consisting of a single plate. The only modification to the shear design resistance equation is the term related to the contribution V_w of the web. The modified shear design resistance V_P of aluminum alloy plate girder with web stiffeners is defined as:

$$V_P = V_{w,P} + V_{f,P} \tag{13}$$

where, $V_{w,P} = \rho_v t_w h_w \dfrac{f_w}{\sqrt{3}}$ and the modified factor ρ_v for shear buckling is shown in Table 7. The

comparison of shear buckling factor ρ_v predicted by the current EC9 Code and modified design method is shown in Figure 11. It should be noted that the contribution $V_{f,P}$ of the flanges remains the same and it is defined in Eqs 6 − 7. The modified design method was calibrated against the experimental and numerical results.

Table 8. Comparison of Experimental and Numerical Results with Design Strengths (Group 1)

Specimen	Measured		Test and FEA	Design			Comparison		
	h_w/t_w	a/b_w	V_{Exp} and V_{FEA}	V_{EC}	V_{AA}	V_p	V/V_{EC}	V/V_{AA}	V/V_p
			(kN)	(kN)	(kN)	(kN)			
Test I-7020	191	1.13	157.0	133.1	58.3	140.1	1.18	2.69	1.12
Test II-7020	190	1.14	118.5	134.5	58.3	141.4	0.88	2.03	0.84
Test III-7020	190	1.14	152.0	131.9	58.3	138.8	1.15	2.61	1.10
Test IV-7020	191	1.13	156.8	133.1	58.3	140.1	1.18	2.69	1.12
Test I-6082	190	1.13	119.0	112.1	59.5	111.4	1.06	2.00	1.07
Test II-6082	189	1.13	84.5	114.4	59.5	113.6	0.74	1.42	0.74
Test III-6082	189	1.13	113.5	112.6	59.6	111.8	1.01	1.90	1.02
Test IV-6082	190	1.13	134.5	110.4	59.3	109.8	1.22	2.27	1.22
G1-T1.5-A0.5	393	0.56	81.8	85.5	16.3	89.3	0.96	5.01	0.92
G1-T1.5-A1.0	393	1.11	66.8	46.2	6.5	52.8	1.45	10.28	1.27
G1-T1.5-A2.0	393	2.22	52.8	28.8	4.7	35.6	1.83	11.15	1.48
G1-T1.5-A3.0	393	3.33	34.8	23.6	4.4	30.5	1.47	7.89	1.14
G1-T1.5-A4.0	393	4.44	29.4	21.0	4.3	27.9	1.40	6.85	1.06
G1-T2.0-A0.5	295	0.56	109.4	119.3	38.7	118.3	0.92	2.82	0.92
G1-T2.0-A1.0	295	1.11	89.6	65.6	15.4	72.6	1.37	5.82	1.23
G1-T2.0-A2.0	295	2.22	71.9	42.7	11.2	51.0	1.68	6.41	1.41
G1-T2.0-A3.0	295	3.33	49.7	36.3	10.5	44.8	1.37	4.76	1.11
G1-T2.0-A4.0	295	4.44	43.7	32.9	10.2	41.5	1.33	4.29	1.05
G1-T2.5-A0.5	236	0.56	145.8	156.8	113.0	146.6	0.93	1.29	0.99
G1-T2.5-A1.0	236	1.11	113.3	87.5	30.1	92.7	1.29	3.77	1.22
G1-T2.5-A2.0	236	2.22	90.1	59.1	21.9	67.2	1.52	4.11	1.34
G1-T2.5-A3.0	236	3.33	66.8	51.3	20.4	59.9	1.30	3.27	1.12
G1-T2.5-A4.0	236	4.44	56.4	47.4	19.9	56.2	1.19	2.84	1.00
G1-T3.0-A0.5	197	0.56	180.9	198.6	187.3	183.9	0.91	0.97	0.98
G1-T3.0-A1.0	197	1.11	136.6	112.3	52.0	112.8	1.22	2.63	1.21
G1-T3.0-A2.0	197	2.22	110.4	77.8	37.9	83.6	1.42	2.91	1.32
G1-T3.0-A3.0	197	3.33	86.2	68.4	35.3	75.2	1.26	2.44	1.15
G1-T3.0-A4.0	197	4.44	79.8	63.2	34.4	70.3	1.26	2.32	1.13
G1-T4.0-A0.5	148	0.56	254.3	295.8	334.0	269.6	0.86	0.76	0.94
G1-T4.0-A1.0	148	1.11	190.7	170.1	184.5	153.5	1.12	1.03	1.24
G1-T4.0-A2.0	148	2.22	157.3	121.7	114.2	115.5	1.29	1.38	1.36
G1-T4.0-A3.0	148	3.33	134.9	107.9	96.7	104.0	1.25	1.39	1.30
G1-T4.0-A4.0	148	4.44	124.0	100.9	90.2	97.8	1.23	1.38	1.27
G1-T6.0-A0.5	98	0.56	422.7	547.0	500.9	488.0	0.77	0.84	0.87
G1-T6.0-A1.0	98	1.11	323.4	317.7	481.7	280.3	1.02	0.67	1.15
G1-T6.0-A2.0	98	2.22	265.1	239.0	411.4	207.4	1.11	0.64	1.28
G1-T6.0-A3.0	98	3.33	202.0*	…	…	…	…	…	…
G1-T6.0-A4.0	98	4.44	152.7*	…	…	…	…	…	…
G1-T12.0-A0.5	49	0.56	637.4*	…	…	…	…	…	…
G1-T12.0-A1.0	49	1.11	586.0*	…	…	…	…	…	…
G1-T12.0-A2.0	49	2.22	372.3*	…	…	…	…	…	…
G1-T12.0-A3.0	49	3.33	349.7*	…	…	…	…	…	…
G1-T12.0-A4.0	49	4.44	239.9*	…	…	…	…	…	…
						Mean, U_m	1.20	3.26	1.13
						COV, U_p	0.204	0.790	0.148
						Reliability index, β_1	2.44	2.25	3.16
						Resistance factor, ϕ_{v1}	0.91	0.80	0.80
						Reliability index, β_2	2.98	2.25	3.16
						Resistance factor, ϕ_{v2}	0.80	0.80	0.80

Note: * Failed by bending, hence not compared with the shear design resistance.

Table 9. Comparison of Numerical Results with Design Strengths (Group 2)

Specimen	Measured		Test and FEA	Design			Comparison		
	h_w/t_w	a/b_w	V_{Exp} and V_{FEA} (kN)	V_{EC} (kN)	V_{AA} (kN)	V_p (kN)	V/V_{EC}	V/V_{AA}	V/V_p
G2-T1.5-F2-A1.0	398	1.10	40.2	24.7	6.5	31.4	1.63	6.21	1.28
G2-T1.5-F3-A1.0	397	1.10	47.4	30.9	6.5	37.6	1.54	7.32	1.26
G2-T1.5-F4-A1.0	396	1.10	55.4	36.4	6.5	43.1	1.52	8.55	1.29
G2-T1.5-F5-A1.0	395	1.11	63.8	40.9	6.5	47.5	1.56	9.83	1.34
G2-T2.0-F2-A1.0	298	1.10	60.7	42.9	15.3	50.1	1.42	3.96	1.21
G2-T2.0-F3-A1.0	297	1.10	71.5	52.2	15.4	59.3	1.37	4.65	1.21
G2-T2.0-F4-A1.0	296	1.11	83.5	59.8	15.4	66.9	1.40	5.43	1.25
G2-T2.0-F5-A1.0	295	1.11	89.6	65.6	15.4	72.6	1.37	5.82	1.23
G2-T2.5-F2-A1.0	238	1.10	84.8	65.6	30.0	70.9	1.29	2.83	1.20
G2-T2.5-F3-A1.0	237	1.11	99.1	78.0	30.0	83.3	1.27	3.30	1.19
G2-T2.5-F4-A1.0	236	1.11	113.3	87.5	30.1	92.7	1.29	3.77	1.22
G2-T2.5-F5-A1.0	235	1.12	122.0	94.3	30.1	99.4	1.29	4.05	1.23
G2-T3.0-F2-A1.0	198	1.10	112.5	92.4	51.9	93.1	1.22	2.17	1.21
G2-T3.0-F3-A1.0	197	1.11	129.6	108.1	52.0	108.6	1.20	2.49	1.19
G2-T3.0-F4-A1.0	196	1.12	141.7	119.6	52.1	119.9	1.19	2.72	1.18
G2-T3.0-F5-A1.0	195	1.12	149.7	127.1	52.2	127.4	1.18	2.87	1.18
G2-T6.0-F2-A1.0	98	1.12	327.8	335.1	481.0	297.7	0.98	0.68	1.10
G2-T6.0-F3-A1.0	97	1.13	337.7	372.3	479.0	335.0	0.91	0.70	1.01
G2-T6.0-F4-A1.0	96	1.14	352.9	391.4	477.0	354.2	0.90	0.74	1.00
G2-T6.0-F5-A1.0	95	1.15	373.3	400.4	474.9	363.4	0.93	0.79	1.03
G2-T1.5-F2-A2.0	398	2.19	32.9	18.0	4.7	24.9	1.83	7.02	1.32
G2-T1.5-F3-A2.0	397	2.20	37.1	21.1	4.7	28.0	1.76	7.90	1.33
G2-T1.5-F4-A2.0	396	2.21	41.9	23.9	4.7	30.7	1.76	8.90	1.36
G2-T1.5-F5-A2.0	395	2.21	46.9	26.1	4.7	33.0	1.80	9.94	1.42
G2-T2.0-F2-A2.0	298	2.20	50.9	31.2	11.1	39.6	1.63	4.58	1.28
G2-T2.0-F3-A2.0	297	2.21	57.6	35.9	11.2	44.3	1.60	5.16	1.30
G2-T2.0-F4-A2.0	296	2.21	64.7	39.8	11.2	48.2	1.63	5.78	1.34
G2-T2.0-F5-A2.0	295	2.22	71.9	42.7	11.2	51.0	1.68	6.41	1.41
G2-T2.5-F2-A2.0	238	2.20	71.6	47.7	21.8	55.9	1.50	3.29	1.28
G2-T2.5-F3-A2.0	237	2.21	81.0	54.1	21.8	62.3	1.50	3.71	1.30
G2-T2.5-F4-A2.0	236	2.22	90.1	59.1	21.9	67.2	1.52	4.11	1.34
G2-T2.5-F5-A2.0	235	2.23	96.8	62.7	22.0	70.8	1.54	4.40	1.37
G2-T3.0-F2-A2.0	198	2.21	94.7	67.2	37.6	73.2	1.41	2.52	1.29
G2-T3.0-F3-A2.0	197	2.22	106.9	75.5	37.8	81.3	1.42	2.83	1.31
G2-T3.0-F4-A2.0	196	2.23	115.7	81.8	38.0	87.4	1.42	3.04	1.32
G2-T3.0-F5-A2.0	195	2.24	121.7	86.1	38.2	91.6	1.41	3.19	1.33
G2-T6.0-F2-A2.0	98	2.23	277.7	243.2	411.6	211.5	1.14	0.67	1.31
G2-T6.0-F3-A2.0	97	2.26	295.9	268.2	412.0	236.6	1.10	0.72	1.25
G2-T6.0-F4-A2.0	96	2.28	306.9	283.2	412.3	251.6	1.08	0.74	1.22
G2-T6.0-F5-A2.0	95	2.31	319.6	291.1	412.6	259.5	1.10	0.77	1.23
Mean, U_m							1.38	4.11	1.25
COV, U_p							0.181	0.642	0.078
Reliability index, β_1							3.06	3.05	4.05
Resistance factor, ϕ_{v1}							0.91	0.80	0.80
Reliability index, β_2							3.62	3.05	4.05
Resistance factor, ϕ_{v2}							0.80	0.80	0.80

Table 10. Comparison of Numerical Results with Design Strengths (Group 3)

Specimen	Measured		Test and FEA	Design			Comparison		
	h_w/t_w	a/b_w	V_{Exp} and V_{FEA} (kN)	V_{EC} (kN)	V_{AA} (kN)	V_p (kN)	V/V_{EC}	V/V_{AA}	V/V_p
G3-T2.0-S2-A0.5	295	0.56	80.6	119.7	38.7	118.7	0.67	2.08	0.68
G3-T2.0-S3-A0.5	295	0.56	93.2	119.6	38.7	118.6	0.78	2.41	0.79
G3-T2.0-S4-A0.5	295	0.56	106.8	119.4	38.7	118.4	0.89	2.76	0.90
G3-T2.0-S5-A0.5	295	0.56	109.4	119.3	38.7	118.3	0.92	2.82	0.92
G3-T2.5-S2-A0.5	236	0.56	112.8	157.6	113.0	147.3	0.72	1.00	0.77
G3-T2.5-S3-A0.5	236	0.56	129.3	157.2	113.0	147.0	0.82	1.14	0.88
G3-T2.5-S4-A0.5	236	0.56	145.8	156.8	113.0	146.6	0.93	1.29	0.99
G3-T2.5-S5-A0.5	236	0.56	156.2	156.6	113.0	146.3	1.00	1.38	1.07
G3-T3.0-S2-A0.5	197	0.56	149.4	199.6	187.3	184.9	0.75	0.80	0.81
G3-T3.0-S3-A0.5	197	0.56	168.9	199.0	187.3	184.3	0.85	0.90	0.92
G3-T3.0-S4-A0.5	197	0.56	183.3	198.5	187.3	183.8	0.92	0.98	1.00
G3-T3.0-S5-A0.5	197	0.56	192.0	198.2	187.3	183.5	0.97	1.03	1.05
G3-T6.0-S2-A0.5	98	0.56	432.0	545.9	500.9	487.0	0.79	0.86	0.89
G3-T6.0-S3-A0.5	98	0.56	443.6	544.6	500.9	485.6	0.81	0.89	0.91
G3-T6.0-S4-A0.5	98	0.56	454.6	543.3	500.9	484.3	0.84	0.91	0.94
G3-T6.0-S5-A0.5	98	0.56	472.6	541.1	500.9	482.2	0.87	0.94	0.98
G3-T1.5-S2-A1.0	393	1.11	41.4	46.5	6.5	53.1	0.89	6.37	0.78
G3-T1.5-S3-A1.0	393	1.11	49.2	46.4	6.5	53.0	1.06	7.57	0.93
G3-T1.5-S4-A1.0	393	1.11	57.4	46.3	6.5	52.9	1.24	8.83	1.08
G3-T1.5-S5-A1.0	393	1.11	65.5	46.2	6.5	52.8	1.42	10.08	1.24
G3-T2.0-S2-A1.0	295	1.11	61.7	66.2	15.4	73.3	0.93	4.01	0.84
G3-T2.0-S3-A1.0	295	1.11	73.1	66.0	15.4	73.0	1.11	4.75	1.00
G3-T2.0-S4-A1.0	295	1.11	84.9	65.7	15.4	72.8	1.29	5.51	1.17
G3-T2.0-S5-A1.0	295	1.11	89.6	65.6	15.4	72.6	1.37	5.82	1.23
G3-T2.5-S2-A1.0	236	1.11	85.6	88.5	30.1	93.6	0.97	2.84	0.91
G3-T2.5-S3-A1.0	236	1.11	100.3	88.0	30.1	93.2	1.14	3.33	1.08
G3-T2.5-S4-A1.0	236	1.11	113.3	87.5	30.1	92.7	1.29	3.77	1.22
G3-T2.5-S5-A1.0	236	1.11	119.8	87.3	30.1	92.5	1.37	3.98	1.30
G3-T3.0-S2-A1.0	197	1.11	113.1	113.4	52.0	113.9	1.00	2.18	0.99
G3-T3.0-S3-A1.0	197	1.11	130.2	112.6	52.0	113.1	1.16	2.50	1.15
G3-T3.0-S4-A1.0	197	1.11	140.0	112.1	52.0	112.6	1.25	2.69	1.24
G3-T3.0-S5-A1.0	197	1.11	145.5	111.8	52.0	112.3	1.30	2.80	1.30
G3-T6.0-S2-A1.0	98	1.11	327.1	317.1	481.7	279.7	1.03	0.68	1.17
G3-T6.0-S3-A1.0	98	1.11	334.8	315.8	481.7	278.4	1.06	0.70	1.20
G3-T6.0-S4-A1.0	98	1.11	343.3	314.3	481.7	276.9	1.09	0.71	1.24
G3-T6.0-S5-A1.0	98	1.11	354.5	312.2	481.7	274.8	1.14	0.74	1.29
						Mean, U_m	0.99	2.96	1.02
						COV, U_p	0.210	0.791	0.169
						Reliability index, β_1	1.80	2.13	2.67
						Resistance factor, ϕ_{v1}	0.91	0.80	0.80
						Reliability index, β_2	2.47	2.13	2.67
						Resistance factor, ϕ_{v2}	0.80	0.80	0.80

Table 11. Comparison of Numerical Results with Design Strengths (Group 4)

Specimen	Measured		Test and FEA	Design			Comparison		
	h_w/t_w	a/b_w	V_{Exp} and V_{FEA} (kN)	V_{EC} (kN)	V_{AA} (kN)	V_p (kN)	V/V_{EC}	V/V_{AA}	V/V_p
G4-T1.5	393	1.11	62.5	46.2	6.5	52.8	1.35	9.62	1.18
G4-T2.0	295	1.11	82.5	65.8	15.4	72.9	1.25	5.36	1.13
G4-T2.5	236	1.11	102.4	88.1	30.1	93.3	1.16	3.40	1.10
G4-T3.0	197	1.11	121.5	113.2	52.0	113.6	1.07	2.34	1.07
G4-T4.0	148	1.11	168.2	171.6	184.5	145.9	0.98	0.91	1.15
G4-T6.0	98	1.11	280.6	321.1	481.7	263.3	0.86	0.58	1.07
G4-T12.0	49	1.11	556.4[*]	…	…	…	…	…	…
					Mean, U_m		1.11	3.70	1.12
					COV, U_p		0.161	0.914	0.042
					Reliability index, β_1		2.27	1.55	3.66
					Resistance factor, ϕ_{v1}		0.91	0.80	0.80
					Reliability index, β_2		2.67	1.55	3.66
					Resistance factor, ϕ_{v2}		0.80	0.80	0.80

Note: * Failed by bending, hence not compared with the shear design resistance.

11.   COMPARISON OF EXPERIMENTAL AND NUMERICAL RESULTS WITH PROPOSED DESIGN STRENGTHS

The unfactored shear design resistances (V_p) calculated using the modified design method were compared with the test results (V_{Exp}) and the shear strengths (V_{FEA}) predicted by the FEA. The proposed design strengths were calculated using the measured cross-section dimensions and measured material properties. The resistance facto $\phi_v = 0.8$ was obtained from the reliability analysis. The load combination of 1.2DL + 1.6LL was used to determine the reliability indices (β_1 and β_2).

The proposed design strengths are generally conservative and reliable. The maximum mean value of the load ratio is 1.25 with the corresponding COV of 0.078 and the value of $\beta_1 = \beta_2 = 4.05$ for the Group 2, as shown in Table 9. The minimum mean value of the load ratio is 1.02 with the corresponding COV of 0.169 and the value of $\beta_1 = \beta_2 = 2.67$ for the Group 3, as shown in Table 10. The reliability indices ((β_1 and β_2) are greater than the target value for all specimens. It is shown that the proposed design method provides more accurate and reliable predictions than the current design rules for aluminum alloy plate girders subjected to shear force.
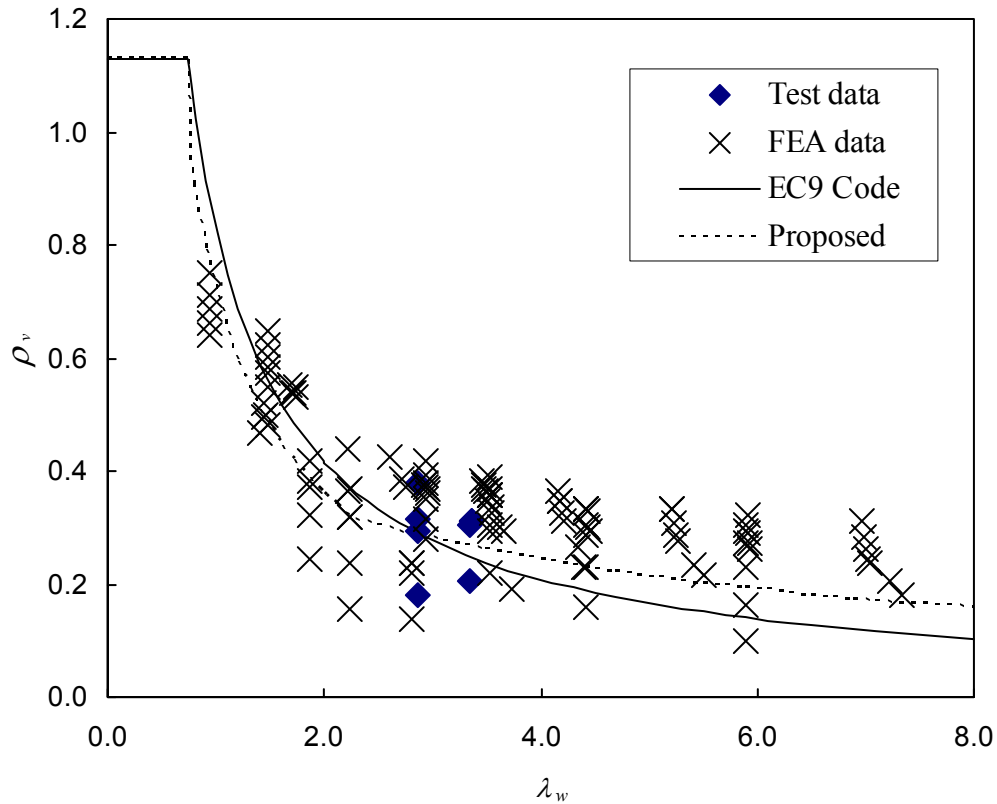
Figure 11. Factor ρ_v for Shear Buckling

12.   CONCLUSIONS

Numerical investigation of welded aluminum alloy plate girders with end posts having a single plate subjected to shear force has been presented in this paper. A finite element model including geometric and material non-linearities has been developed and verified against experimental results. The heat affected zone (HAZ) softening due to welding of the aluminum alloy is also considered in the finite element model. The finite element model closely predicted the shear behaviour of aluminum alloy plate girders compared with the test results. Hence, parametric study was carried out to study the effects of cross-section geometries on the shear resistance of aluminum alloy plate girders with non-rigid end post.

The appropriateness of the shear resistance design rules in the current European Code and American Specification for aluminum structures has been examined. The test results and the shear resistance predicted by the finite element analysis were compared with the design strengths obtained using the current European Code and American Specification for aluminum structures. It is shown that the design strengths predicted by the European Code are generally conservative but not reliable. The design strengths predicted by the American Specification are generally very conservative. Therefore, a design method for shear resistance of aluminum alloy plate girders has been proposed by small modifications to the design rules in the current European Code. It is shown that the proposed design strengths are generally conservative and reliable. It is also shown that the proposed design method provides more accurate and reliable predictions than the current design rules in the European Code and American Specification for welded aluminum alloy plate girders subjected to shear force.

ACKNOWLEDGEMENTS

NOTATION

The following symbols are used in this paper:

a	=	distance between transverse stiffener;
b_f	=	flange width;
b_s	=	stiffener width;
b_w	=	depth of straight portion of a web excluding welds;
COV	=	coefficient of variation;
d_c	=	web depth measured between the mid-lines of the flanges;
E	=	Young's modulus of the material;
f_{aw}	=	ultimate strength of the web material;
f_{ow}	=	strength for overall yielding;
f_f	=	0.2% proof stress of the flange material;
F_m	=	mean value of fabrication factor;
f_s	=	0.2% proof stress of the stiffener material;
$f_{v,AA}$	=	shear design stress obtained using the AA Specification;
f_w	=	0.2% proof stress of the web material;
h_w	=	web depth measured between the flanges;
M_{Ed}	=	design bending moment;
$M_{f,BS}$	=	design moment resistance of a cross section considering the flange only;
M_m	=	mean value of material factor;
t_f	=	flange thickness;
t_s	=	stiffener thickness;
t_w	=	web thickness;
U_m	=	mean value of load ratio;
U_p	=	coefficient of variation of load ratio;
V_{AA}	=	shear resistance obtained using the AA Specification;
V_{EC}	=	shear resistance obtained using the EC9 Code;
V_{Exp}	=	shear ultimate load obtained from the tests;
V_{FEA}	=	shear resistance predicted by the finite element analysis;
V_F	=	coefficient of variation of fabrication factor;
V_M	=	coefficient of variation of material factor;
V_p	=	shear resistance obtained using the proposed design rules;
β	=	reliability index;
ε^{pl}_{true}	=	plastic true strain;
ϕ_v	=	resistance factor;
v	=	Poisson ratio;
ρ_v	=	factor for shear buckling;
σ_{true}	=	true stress;
λ_w	=	slenderness parameter.

REFERENCES

[1]   Evans, H.R., "Longitudinally and Transversely Reinforced Plate Girders", In Plated Structures, Stability and Strength, Ch. 1, Applied Science Publishers, London, 1983.

[2]   Tang, K.H. and Evans, H.R., "Transverse Stiffeners for Plate Girder Webs – An Experimental Study", Journal of Constructional Steel Research, 1984, Vol. 4, No. 4, pp. 253-280.

[3]   Narayanan, R. and Der-Avanessian, N.G.V., "Analysis of Late Girders with Perforated Webs." Thin-walled Structures, 1986, Vol. 4, No. 5, pp. 363-380.

[4]   Sulyok, M. and Galambos, T.V., "Evaluation of web buckling test results on welded beams and plate girders subjected to shear." Engineering Structures, 1996, Vol. 18, No. 6, pp. 459-464.

[5]   Real, E., Mirambell, E. and Estrada, I., "Shear Response of Stainless Steel Plate Girders", Engineering Structures, 2007, Vol. 29, No. 7, pp. 1626-1640.

[6]   Alinia, M.M., Shakiba, M. and Habashi, H.R., "Shear Failure Characteristics of Steel Plate Girders", Thin-walled Structures, 2009, Vol. 47, No. 12, pp. 1498-1506.

[7]   Evans, H.R. and Hamoodi, M.J., "The Collapse of Welded Aluminum Plate Girders - An Experimental Study", Thin-walled Structures, 1987, Vol. 5, No. 4, pp. 247-275.

[8]   Cheng, M., Shi, Y.J. and Wang, Y.Q., "Shear Resistance of Aluminum Plate Girders", In : Proc., 6th International Conference on Steel and Aluminum Structures, Oxford Brookes University, 2007.

[9]   Kissell, J.R. and Ferry, R.L., "Aluminum Structures - A Guide to their Specifications and Design", 2nd ed. New York: Wiley, 2002.

[10] ABAQUS Standard User's Manual, Hibbitt, Karlsson and Sorensen, Inc. Vols. 1-3, Version 6.7, USA, 2007.

[11] Lam, H.C., "The Analysis of Aluminum Plate Girders", PhD Thesis, University of Wales, College of Cardiff, 1993.

[12] EC9, Eurocode 9 : Design of Aluminum Structures – Part 1.1 : General Structural Rules, BS EN 1999-1-1:2007, European Committee for Standardization, 2007.

[13] AA, Aluminum Design Manual, The Aluminum Association. Washington, D.C, 2005.

[14] ASCE, Minimum Design Loads for Buildings and Other Structures, ASCE Standard 7-05, American Society of Civil Engineers Standard, New York, 2005.

STUDY ON UNIFIED BEARING CAPACITY OF RECTANGULAR CONCRETE-FILLED STEEL TUBULAR COLUMN SUBJECTED TO AXIAL COMPRESSION

Feng Yu[1,*], Shuanhai He[2] and Ditao Niu[3]

[1]*Associate professor, School of Civil Engineering, Anhui University of Technology, China*
[2]*Institute of highway, Chang'an University, China*
[3]*College of Civil Engineering, Xi'an University of Architecture and Technology, China*
(Corresponding author: E-mail: yufeng2007@126.com)

ABSTRACT: This paper summarizes the calculating methods of the bearing capacity of rectangular concrete-filled steel tubular columns(CFT) subjected to axial compression, and then points out the deficiency of the existing calculation methods of the bearing capacity. Based on the analysis of the experimental data, the concept of the effective confinement of rectangular CFT columns are introduced. The effects of the cross-sectional aspect ratios, the strength of in-filled concrete, the thickness of steel tube, the equivalent confining coefficient and the longitudinal stiffener on the bearing capacity are carefully considered, and the unified model of the bearing capacity of rectangular CFT columns are presented. The model may be applicable to calculate the bearing capacity of the normal strength concrete filled steel tubular column, the high-strength concrete-filled steel tubular column, the concrete filled thin-walled steel tubular column and concrete-filled stiffened thin-walled steel tubular column. The predictions of the model agree well with large experimental results. Comparisons are also made with predicted column bearing capacity using the existing design codes.

Keywords: Concrete-filled steel tube, Bearing capacity, Effective confinement, Short column, Axial compression

1. INTRODUCTION

Concrete-filled steel tube is a new structure, which has developed on the basis of steel reinforced concrete structure and spiral hoop reinforced concrete structure. The earliest concrete filled steel tube structure was used as the pier of English Severn railway bridge built in 1879, at that time, the purpose of pouring concrete into the tube is to prevent the errosion of steel tube and carry axial compression. Subsequently, due to the high axial load capacity, good ductility, large engergy absorption of concrete filled steel tubes, it has been widely used in structural columns of multi-storey and tall buildings, bridges, barriers and so on(ACI318[1], CECS28:90[2], EC4[3], DL/T5085-1999[4]). The increment in structural properties of CFT columns is mainly determined by the composite action between the steel tube and core concrete. The core concrete confined by steel tube behaves in a triaxial stress state and also prevents the wall of steel tube from inward buckling.

According to the cross-sectional shapes, concrete filled steel tubular column may be divided into circular and rectangular CFT column. The behavior of rectangular CFT column differ from that of its circular counterpart, this is mainly because that the confinement action of circular steel tube to concrete is greater than its rectangular counterpart, and that the local buckling is more likely to occur for rectangular CFT column. Therefore, circular CFT columns have been widely used in civil engineering (Han[5], Zhong[6]). While rectangular CFT columns are not widely used, the main reason is that the study on the mechanical behavior of rectangular CFT is not systematic and perfect, and the related unified design codes are also lack for different kinds of rectangular CFT columns.

The determination of the bearing capacity is the key to study the performance of rectangular CFT columns. Scholars have done a lot of experimental study and theoretical analysis on the bearing capacity of rectangular CFT column, the plentiful and substantial achievements have been obtained, and the related design specifications and technical regulations are also established. But great difference also exists in the design specifications and technical regulations of different countries(ACI318[1], EC4[3], ASCCS[7], AIJ[8]), and even if the different standards in the same country such as China (DL/T5085-1999[4], JCJ01-89[9], CECS159-2004[10], GJB4142-2000[11], DBJ13-51-2003[12]). The existing calculating models have higher calculating precision only for rectangular CFT columns with normal concrete strength, but it will produce great errors by using the existing models to predict the bearing capacity of other types rectangular CFT columns such as high-strength concrete-filled steel tubular column, concrete filled thin-walled steel tubular column and concrete-filled stiffened thin-walled steel tubular column. Based on the analysis of many experimental data, this paper presents a unified bearing capacity for different types of rectangular CFT columns. The effects of the cross-sectional aspect ratios, the strength of in-filled concrete, the thickness of steel tube, the equivalent confinement coefficient and the longitudinal stiffener on the bearing capacity are carefully considered. The predictions of the proposed model agree well with large experimental data.

2.   LITERATURE REVIEW

Many studies have been carried out to investigate the behavior of rectangular CFT columns subjected to axial compression, it is well known that the bearing capacity and ductility can be certainly increased by the confinement of rectangular steel tube, The earliest study on the bearing capacity of rectangular CFT columns were widely carried out(Han[5], Zhong[6], Furlon[13], Yu and Niu[14], Uy.[15], Cai[16]), the calculating models of the bearing capacity of CFT columns mainly include the following types:

EC4[3] is the most recently completed international standard in composite construction. EC4 covers concrete-filled and partially filled steel tubes and concrete-filled steel tube with or without reinforcement. EC4 considers the confinement effects for circular sections when relative slenderness has value less than 0.5. EC4 uses the limit state concepts to acquire the aim of serviceability and safety by applying partial safety factors to load and material properties. It is the only code that treats the effects of long-term loading separately. Based on the superposition method of steel tube and core concrete, the ultimate axial bearing capacity of a rectangular column is that

$$N = A_s f_y + A_c f_{co}'$$ (1)

Where, A_s is the section area of steel tube, f_y is the tensile yield strength of steel tube, A_c is the section area of core concrete, f_{co}' is the compressive strength of unconfined concrete column. The ACI and Australian Standards (AS) use the same equation for calculating the bearing capacity. The confinement of steel tube to concrete are not well considered in both codes. The limiting thickness of steel tube to prevent local buckling is almost the same for both codes and is calculated in succeeding paragraphs. The equation of the bearing capacity is given by

$$N = A_s f_y + 0.85 A_c f_{co}'$$ (2)

Han[5] considered the effect of rectangular steel tube on the bearing capacity, taking the confinement effect coefficient as main parameter, the bearing capacity is determined by

$$N = f_{sc} A_{sc} \tag{3}$$

Where, A_{sc} is the section area of CFT columns, f_{sc} is the compound strength of CFT columns subjected to axial compression, whose expression is that

$$f_{sc} = \left(1.212 + B\xi + C\xi^2\right) f_{co}' \tag{4}$$

Where, $B = 0.138 f_y / 215 + 0.765$, $C = -0.072 f_c / 15 + 0.0216$, ξ is the confinement effect coefficient, the expression is that

$$\xi = \frac{A_s f_y}{A_c f_{co}'} \tag{5}$$

Also, the section should follow these limits: side/edge of steel columns should be greater than or equal to 20mm and thickness of the steel should be greater than or equal to 4mm.

In the code of AISC[17], the equivalent substitution principle is adopted, which converts the concrete strength to steel strength, the equation of concrete filled rectangular steel tube is that

$$N = A_s F_{cr} \tag{6}$$

Where, A_s is the section area of the steel tube, the expression of F_{cr} is that

$$F_{cr} = \begin{cases} \left(0.658^{\lambda_c^2}\right) F_{my} & \lambda_c \leq 1.5 \\ \left(0.877 / \lambda_c^2\right) F_{my} & \lambda_c > 1.5 \end{cases} \tag{7}$$

Where, $F_{my} = f_y + 0.85 f_{co}' \left(A_c / A_s\right)$, $\lambda_c = \dfrac{\sqrt{F_{my} / E_s}}{i_s \pi}$, E_s is the elastic modulus of steel tube, i_s is the radius of gyration of steel tube.

Considering the effect of concrete strength, Yu[18] proposed the bearing capacity of concrete filled square steel tube is that

$$N = A_s f_y + A_c f_c (1 + \phi) \tag{8}$$

Where, ϕ is the coefficient of concrete strength, the expression is that

$$\phi = 17(D/t)^{-2}\left(f_y / f_c\right) \tag{9}$$

Where, D is the length of square steel tube, t is the thickness of steel tube.

Based on the analysis of research results, we can conclude that some deficiency also exists in the calculating methods of the bearing capacity of rectangular CFT columns.

The existing models of the bearing capacity have higher calculating precision only for the limited experimental data, but for large experimental data, the calculating models have the bigger errors among different countries specifications, so the calculating accuracy of the existing models need to be further improved.

Scholars have studied the effect of length to width ratio of rectangular steel tube on the bearing capacity, but these studies have been limited to experimental research. The approximate law that the bearing capacity changes with the length to width ratio of rectangular steel tube can be obtained by experimental study, but the numerical and theoretical relations between the length to width ratio and the bearing capacity are not proposed.

The existing study mainly concerned on plain rectangular CFT columns, but for high strength rectangular CFT columns, the study is not only few, but also lack of systematic analysis. Meanwhile, the confinement effect of rectangular steel tube to concrete is also affected by the concrete strength, how to reflect the effect of concrete strength on the calculating models of the bearing capacity is urgent to be solved.

The bearing capacity of plain concrete filled steel tube is different from that of thin-walled concrete filled steel tube, the effect of the thickness of thin-walled steel tube, and the longitudinal stiffened rib on the bearing capacity are not reflected in existing calculation methods.

The behavior of rectangular CFT columns differs from that of circular CFT columns owing to the confinement of core concrete provided by steel tube. It is shown that the confinement of rectangular CFT columns is not as good as its circular counterpart. This is due to the fact that the confinement of rectangular steel tube to concrete may be divided into the effective and non-effective confining zone. In existing calculating methods of the bearing capacity, the influence of the effective confining zone on the bearing capacity of rectangular CFT columns is not reflected.

3.   THE PROPOSED UNIFIED MODELS OF THE BEARING CAPACITY

3.1   The Confining Action of Rectangular Steel Tube to Concrete

The confining action of rectangular CFT columns are much less than that of circular CFT columns. This is mainly because that the confining action of rectangular steel tube to concrete is uneven, and the local buckling is more likely to occur due to the stress concentration in the corner of rectangular steel tube. In addition, the effective confinement can not be fully provided in the middle of section side of rectangular CFT columns. It is considered that the confining stress of steel tube is applied to concrete by arch action, and the arch action occurs within the section of rectangular CFT columns, whose shape is quadratic parabola. The confining action of rectangular steel tube to concrete is shown in Fig.1, from the figure, we can conclude that the non-effective confining area is maximum at the top of arch, and the effective confining area is minimum at the same time. According to the analysis of large experimental data, this paper believes that the quadratic parabola of initial angle is about 10°. The effective confining area of core concrete by rectangular steel tube is that
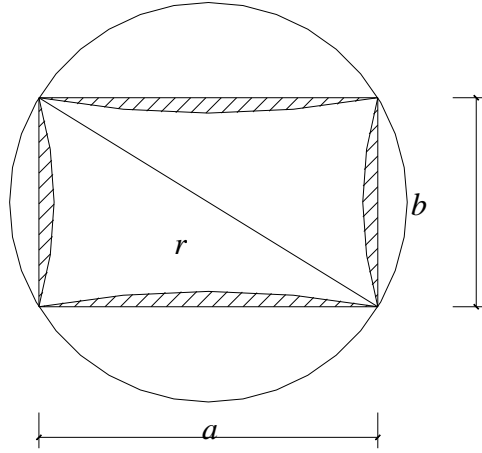
$$A_e = A - A_u$$

(9)

Figure 1. The Confining Action of Rectangular Steel Tube to Concrete

Where, A_e is the effective confining area, A is the area of rectangular CFT columns, A_u is the non-effective confining area, whose expression is that

$$A_u = \frac{a^2 + b^2}{12ab} \tag{10}$$

This paper defines the coefficient of the effective confining area of rectangular CFT columns k_s is that

$$k_s = \frac{A_e}{A} \tag{11}$$

Substituting Eq. 9 into Eq. 11, We can conclude that

$$k_s = 1 - \frac{a^2 + b^2}{12ab} \tag{12}$$

3.2   The Proposed Model of the Bearing Capacity

Based on the proposed calculating equation of the bearing capacity of circular CFT columns (Cai[16]), the effects of the section shape, the strength of in-filled concrete, the thickness of steel tube, the equivalent confinement effect coefficient and the longitudinal stiffener on the bearing capacity of rectangular CFT columns are well considered. According to the analysis of large experimental data, this paper presents a unfied calculating model for the bearing capacity of rectangular CFT columns. The expression of N is that

$$N = k_s k_e N_c + A_{ss} f_{ss} \tag{13}$$

Where, k_e is the area ratio of rectangular CFT to the circumcircle (shown in Figure 1), whose expression can be shown by Eq. 14; A_{ss} and f_{ss} are respectively the section area and yield strength of longitudinal stiffener; N_c is the bearing capacity of the corresponding circular CFT columns, whose diameter is the circumcircle of rectangular CFT columns. The expression of N_c can be shown by Eq. 15.

$$k_e = \frac{4ab}{\pi(a^2 + b^2)} \tag{14}$$

$$N_c = A_{ec} f_{co}^{'} \left(1 + k\xi_e\right) \tag{15}$$

Where, A_{ec} is the circumcircle area of rectangular CFT columns, the expression is given by Eq.16. $f_{co}^{'}$ is the axial compressive strength of unconfined concrete, the conversion relation between $f_{co}^{'}$ and the cubic compressive strength is shown in Table 1. ξ_e is the equivalent confinement effect coefficient, the expression is given by Eq. 17. k is the increasing coefficient of the concrete strength, when $\xi_e \leq 1.235$, $k = 2$; when $\xi_e \leq 0.40$ and the concrete strength grade $\leq$ C50, $k = 2.6$; when $\xi_e \geq 1.235$, $k = 1/\sqrt{\xi_e} + 1.1$.

$$A_{ec} = \pi(a^2 + b^2)/4 \tag{16}$$

$$\xi_e = A_{es} f_{ey} / A_{ec} f_{co}^{'} \tag{17}$$

Where, A_{es} and f_{ey} are respectively the thickness of circumcircle steel tube and yield strength, which is same as those of rectangular CFT columns.

Table 1. Conversion Relation between
Axial Compressive Strength and Cubic Compressive Strength

Concrete strength grade	C50	C55	C60	C65	C70	C75	C80	C85	C90	C95	C100
Conversion coefficient	0.67	0.693	0.716	0.739	0.762	0.785	0.808	0.831	0.854	0.877	0.900

3.3   The Test Verification of the Calculating Model

Using Eq.13, a large number of experimental data of rectangular CFT columns are analyzed and verified, the comparison between the calculating results and the experimental results are shown in Table 2. In Table 2, N_e is the experimental results, N_{c1} is the calculating results of the proposed equation in this paper, N_{c2} and N_{c3} are respectively the calculating results of China GB(2000) and EC4. The calculating results show that the average value of the ratio of N_e/N_c of the models in this paper is 0.99, and the mean square deviation is 0.01; while the average value of the ratio of N_e/N_c of China GB(2000) is 0.97, and the mean square deviation is 0.02; the average value of the ratio of N_e/N_c of EC4 is 1.18, and the mean square deviation is 0.03. Therefore, the calculating model in this paper not only has higher calculation precision, but also may be applicable to predict the bearing capacity of different kinds of rectangular CFT columns. While the calculation precision of China GB(2000) takes second place, and the calculating results of EC4 is conservative, which is low ratio 18% compared with experimental data.

Table 2. Comparison between Experimental Results and Calculating Values
of the Bearing Capacity of Rectangular CFT Columns

References	a / mm	b / mm	t / mm	f_y / Mpa	f_{co}' / Mpa	N_e / kN	N_{c1} / kN	$\dfrac{N_e}{N_{c1}}$	$\dfrac{N_e}{N_{c2}}$	$\dfrac{N_e}{N_{c3}}$
Shakir and Zeghiche [19]	120.0	80.0	5.00	386	28.0	950.0	976.4	0.97	0.97	0.99
	120.0	80.0	5.00	386	25.5	950.0	941.4	1.01	0.96	1.01
	120.0	80.0	5.00	384	25.5	900.0	938.4	0.96	0.96	0.96
	120.0	80.0	5.00	384	28.0	910.0	973.3	0.93	0.97	0.96
	120.0	80.0	5.00	343	27.4	900.0	902.1	1.00	0.97	1.04
	120.0	80.0	5.00	343	28.6	900.0	918.3	0.98	0.98	1.03
	120.0	80.0	5.00	357	28.0	920.0	931.9	0.99	0.97	1.03
Shakir and Mouli[20]	120.0	80.0	5.00	357	26.5	850.0	911.4	0.93	0.97	0.96
	120.0	80.0	5.00	341	27.0	900.0	893.6	1.01	0.97	1.05
	120.0	80.0	5.00	341	29.4	920.0	925.9	0.99	0.98	1.05
	120.0	80.0	5.00	362	27.0	950.0	925.9	1.03	0.97	1.05
	120.0	80.0	5.00	362	26.0	955.0	912.1	1.05	0.96	1.07
	150.0	100.0	5.00	346	29.3	1370.0	1285.4	1.07	0.97	1.16
	150.0	100.0	5.00	346	29.3	1210.0	1285.4	0.94	0.97	1.03
	150.0	100.0	5.00	346	29.3	1340.0	1285.4	1.04	0.97	1.14
	150.0	100.0	5.00	346	29.3	1200.0	1285.4	0.93	0.97	1.02
	150.0	100.0	5.00	340	29.7	1300.0	1281.2	1.01	0.97	1.11
	150.0	100.0	5.00	340	29.7	1190.0	1281.2	0.93	0.97	1.02
	150.0	100.0	5.00	340	30.0	1320.0	1287.2	1.03	0.97	1.13
	150.0	100.0	5.00	340	30.0	1200.0	1287.2	0.93	0.97	1.02
Schneider [21]	152.3	76.6	3.00	430	25.0	819.0	790.6	1.04	0.85	1.01
	152.3	76.6	4.47	383	21.6	1006.0	870.5	1.16	0.84	1.05
	152.4	101.8	4.32	413	21.6	1144.0	1175.4	0.97	0.92	0.99
	152.7	102.8	4.57	365	19.8	1224.0	1100.9	1.11	0.92	1.13
	151.4	101.3	5.72	324	19.8	1335.0	1153.1	1.16	0.93	1.16
	152.4	102.1	7.34	358	19.8	1691.0	1456.1	1.16	0.93	1.10
Jiang et al.[22]	200.0	150.0	4.00	284	22.1	1423.0	1961.7	0.73	1.27	1.09
	300.0	150.0	4.00	284	22.1	1993.0	2578.3	0.77	1.19	1.11
	300.0	200.0	4.00	284	22.1	2410.0	3224.3	0.75	1.21	1.10
Wang and Jiang [23]	150.0	150.0	4.00	308	36.4	1358.0	1378.3	0.99	0.82	1.00
	150.0	125.0	4.00	308	36.4	1092.0	1230.9	0.89	0.85	0.92
	150.0	110.0	4.00	308	36.4	988.0	1139.1	0.87	0.86	0.91
	150.0	100.0	4.00	308	36.4	920.0	1076.4	0.85	0.88	0.90
Han and Yang[24]	100.0	100.0	2.86	228	39.7	760.0	819.9	0.93	1.14	1.36
	100.0	100.0	2.86	228	39.7	800.0	819.9	0.98	1.14	1.43
	120.0	120.0	2.86	228	39.7	992.0	1051.6	0.94	1.08	1.32
	120.0	120.0	2.86	228	39.7	1050.0	1051.6	1.00	1.08	1.39
	110.0	100.0	2.86	228	39.7	844.0	873.8	0.97	1.12	1.39
	110.0	100.0	2.86	228	39.7	860.0	873.8	0.98	1.12	1.42
	150.0	135.0	2.86	228	39.7	1420.0	1341.0	1.06	1.02	1.42
	150.0	135.0	2.86	228	39.7	1340.0	1341.0	1.00	1.02	1.34
	90.0	70.0	2.86	228	39.7	554.0	609.0	0.91	1.24	1.42

	90.0	70.0	2.86	228	39.7	576.0	609.0	0.95	1.24	1.47
	100.0	75.0	2.86	228	39.7	640.0	679.2	0.94	1.20	1.43
	100.0	75.0	2.86	228	39.7	672.0	679.2	0.99	1.20	1.50
	120.0	90.0	2.86	228	39.7	800.0	861.9	0.93	1.12	1.34
	120.0	90.0	2.86	228	39.7	760.0	861.9	0.88	1.12	1.27
	140.0	105.0	2.86	228	39.7	1044.0	1064.6	0.98	1.07	1.36
	140.0	105.0	2.86	228	39.7	1086.0	1064.6	1.02	1.07	1.41
	150.0	115.0	2.86	228	39.7	1251.0	1192.3	1.05	1.04	1.43
	150.0	115.0	2.86	228	39.7	1218.0	1192.3	1.02	1.04	1.39
	160.0	120.0	7.20	228	39.7	1820.0	2527.2	0.72	1.45	1.27
	160.0	120.0	7.20	228	39.7	1770.0	2527.2	0.70	1.45	1.23
	130.0	85.0	2.86	228	39.7	760.0	873.4	0.87	1.11	1.24
	130.0	85.0	2.86	228	39.7	820.0	873.4	0.94	1.11	1.34
	140.0	80.0	2.86	228	39.7	880.0	878.3	1.00	1.10	1.41
	140.0	80.0	2.86	228	39.7	740.0	878.3	0.84	1.10	1.19
Han and Yang [25]	120.0	120.0	3.80	330	27.3	882.0	928.9	0.95	1.04	1.10
	120.0	120.0	3.80	330	31.2	921.7	960.2	0.96	1.02	1.12
	120.0	120.0	3.80	330	49.3	1080.0	1105.7	0.98	0.97	1.13
	120.0	120.0	3.80	330	52.5	1078.0	1131.5	0.95	0.96	1.10
	140.0	140.0	3.80	330	16.0	940.8	1002.7	0.94	1.05	1.09
	140.0	140.0	3.80	330	16.7	921.6	1010.4	0.91	1.05	1.06
	140.0	140.0	3.80	330	54.6	1499.0	1425.1	1.05	0.93	1.20
	120.0	120.0	5.90	321	30.0	1176.0	1312.6	0.90	1.10	1.06
	120.0	120.0	5.90	321	25.8	1195.0	1278.8	0.93	1.10	1.11
	120.0	120.0	5.90	321	52.5	1372.0	1493.5	0.92	1.05	1.09
	140.0	140.0	5.90	321	16.3	1342.0	1428.3	0.94	1.07	1.11
	140.0	140.0	5.90	321	54.6	2009.0	1847.4	1.09	1.01	1.28
	200.0	200.0	5.90	321	17.6	2058.0	2178.7	0.94	1.05	1.10
Tomii and Sakino [26]	100.0	100.0	2.29	298	32.6	508.0	503.7	1.01	0.96	1.15
	100.0	100.0	2.20	346	21.8	521.0	480.5	1.08	1.01	1.25
	100.0	100.0	2.99	294	21.0	539.0	531.6	1.01	1.04	1.18
	100.0	100.0	4.25	290	20.2	680.0	693.8	0.98	1.08	1.15
Tomii and Sakino [27]	150.0	150.0	2.00	348	29.0	1191.8	1035.1	1.15	1.11	1.55
	150.0	150.0	3.20	306	29.0	1322.1	1235.4	1.07	1.13	1.43
	150.0	150.0	4.30	300	29.0	1502.1	1455.2	1.03	1.15	1.36
	150.0	150.0	2.00	348	22.1	1010.7	906.3	1.12	1.12	1.47
	150.0	150.0	3.20	306	22.1	1139.2	1106.6	1.03	1.14	1.35
	150.0	150.0	4.30	300	22.1	1321.0	1326.4	1.00	1.15	1.29
	150.0	150.0	2.00	348	14.4	800.3	761.4	1.05	1.12	1.35
	150.0	150.0	3.20	306	14.4	937.6	961.6	0.97	1.14	1.24
	150.0	150.0	4.30	300	14.4	1125.9	1181.4	0.95	1.14	1.20
Kenji [28]	148.0	148.0	4.38	262	25.4	1153.0	1111.3	1.04	1.02	1.20
	148.0	148.0	4.38	262	40.5	1414.0	1295.9	1.09	0.96	1.26
	148.0	148.0	4.38	262	77.0	2108.0	2207.4	0.95	1.13	1.38
	215.0	215.0	4.38	262	25.4	1777.0	1818.6	0.98	0.97	1.11
	215.0	215.0	4.38	262	41.1	2424.0	2223.8	1.09	0.91	1.22
	215.0	215.0	4.38	262	80.3	3837.0	4203.1	0.91	1.08	1.31
	323.0	323.0	4.38	262	25.4	3367.0	3226.9	1.04	0.91	1.16

	323.0	323.0	4.38	262	41.1	4950.0	4665.6	1.06	0.96	1.30
	323.0	323.0	4.38	262	80.3	7481.0	8345.3	0.90	1.03	1.25
	144.0	144.0	6.36	618	25.4	2572.0	2962.2	0.87	1.12	1.02
	144.0	144.0	6.36	618	40.5	2808.0	3137.0	0.90	1.15	1.06
	144.0	144.0	6.36	618	77.0	3399.0	4572.9	0.74	1.62	1.13
Zhang et al.[29]	101.3	101.3	4.97	347	52.5	1310.0	1272.5	1.03	1.02	1.22
	103.6	103.6	4.90	347	52.5	1340.0	1300.0	1.03	1.00	1.22
	102.0	102.0	4.97	347	52.5	1370.0	1284.4	1.07	1.01	1.27
	142.0	142.0	5.11	347	52.5	2160.0	2069.1	1.04	0.94	1.21
	142.0	142.0	5.08	347	52.5	2250.0	2062.2	1.09	0.94	1.27
	142.0	142.0	5.07	347	52.5	2280.0	2059.8	1.11	0.94	1.28
	142.1	142.1	3.02	255	52.5	1360.0	1554.0	0.88	0.92	1.08
	142.1	142.1	3.02	255	52.5	1150.0	1554.0	0.74	0.92	0.91
	143.1	143.1	3.02	255	52.5	1328.0	1571.2	0.85	0.92	1.04
	142.1	142.1	2.01	305	38.3	1328.0	1178.3	1.13	0.93	1.37
	142.1	142.1	2.01	305	38.3	1364.0	1178.3	1.16	0.93	1.41
	140.9	140.9	2.01	305	38.3	1280.0	1163.0	1.10	0.93	1.34
	103.5	103.5	5.01	347	69.8	1500.0	1471.3	1.02	0.97	1.21
	102.1	102.1	4.97	347	69.8	1330.0	1436.4	0.93	0.97	1.10
	101.9	101.9	5.03	347	69.8	1440.0	1442.4	1.00	0.97	1.19
	142.3	142.3	5.09	347	69.8	2520.0	2362.6	1.07	0.90	1.23
	142.4	142.4	5.10	347	69.8	2610.0	2367.5	1.10	0.90	1.28
	139.1	139.1	5.06	347	69.8	1700.0	2276.8	0.75	0.91	0.87
	141.5	141.5	3.08	255	69.8	1920.0	1845.7	1.04	0.88	1.25
	142.4	142.4	3.05	255	69.8	2060.0	1858.2	1.11	0.88	1.33
	141.6	141.6	3.04	255	69.8	1960.0	1839.0	1.07	0.88	1.28
	143.2	143.2	2.03	305	69.8	1990.0	1736.1	1.15	0.84	1.32
	142.3	142.3	2.01	305	69.8	1855.0	1712.4	1.08	0.84	1.25
	140.5	140.5	2.00	305	69.8	1780.0	1673.4	1.06	0.84	1.23
Ye [30]	130.3	101.6	5.03	347	52.5	1580.0	1502.1	1.05	0.97	1.21
	130.3	102.3	5.14	347	52.5	1600.0	1530.9	1.05	0.97	1.21
	130.3	102.3	5.14	347	52.5	1640.0	1530.9	1.07	0.97	1.24
	162.9	101.5	2.00	305	52.5	1068.0	1151.9	0.93	0.85	1.05
	163.9	100.3	1.99	305	52.5	1080.0	1140.5	0.95	0.85	1.07
	160.8	102.7	2.04	305	52.5	1080.0	1164.9	0.93	0.86	1.06
	161.4	105.9	2.96	255	52.5	1420.0	1303.1	1.09	0.89	1.29
	158.2	105.7	2.93	255	52.5	1440.0	1279.2	1.13	0.90	1.34
	159.1	103.3	4.80	347	52.5	1875.0	1649.2	1.14	0.90	1.25
	156.7	102.4	4.80	347	52.5	1915.0	1623.5	1.18	0.90	1.30
	188.8	104.4	4.85	347	52.5	1820.0	1819.2	1.00	0.85	1.04
	166.3	120.2	2.94	255	52.5	1580.0	1491.5	1.06	0.90	1.27
	161.0	126.2	2.98	255	52.5	1580.0	1533.8	1.03	0.91	1.25
	160.3	126.0	2.92	255	52.5	1560.0	1514.0	1.03	0.90	1.24
	167.4	136.1	5.13	347	52.5	2510.0	2240.3	1.12	0.92	1.28
	170.8	135.3	5.07	347	52.5	2470.0	2242.6	1.10	0.91	1.25
	188.4	121.6	4.88	347	52.5	2260.0	2113.7	1.07	0.87	1.16
	190.9	120.4	4.83	347	52.5	2510.0	2097.1	1.20	0.87	1.29
	125.7	102.7	5.15	347	69.8	1840.0	1691.4	1.09	0.94	1.27

	130.0	120.4	5.03	347	69.8	1820.0	1937.2	0.94	0.92	1.10
	132.3	102.7	4.98	347	69.8	1725.0	1713.8	1.01	0.92	1.16
	160.2	102.1	2.00	305	69.8	1555.0	1377.6	1.13	0.82	1.27
	162.8	99.6	2.13	305	69.8	1460.0	1386.5	1.05	0.82	1.18
	162.3	98.5	2.00	305	69.8	1545.0	1340.0	1.15	0.81	1.28
	159.1	105.1	2.93	255	69.8	1610.0	1513.6	1.06	0.85	1.24
	163.8	102.2	2.93	255	69.8	1680.0	1500.4	1.12	0.84	1.29
	162.6	104.5	3.04	255	69.8	1640.0	1547.6	1.06	0.85	1.23
	156.9	103.4	4.71	347	69.8	2090.0	1851.1	1.13	1.00	1.25
	162.0	106.9	4.81	347	69.8	2320.0	1965.1	1.18	0.99	1.31
	158.9	102.6	4.74	347	69.8	2060.0	1856.6	1.11	0.99	1.22
	164.6	119.7	2.01	305	69.8	1800.0	1643.4	1.10	0.82	1.24
	157.1	122.5	2.01	305	69.8	1800.0	1622.5	1.11	0.83	1.27
	161.9	119.0	2.00	305	69.8	1740.0	1612.0	1.08	0.83	1.23
	160.4	125.1	2.85	255	69.8	1855.0	1777.4	1.04	0.86	1.23
	160.0	125.6	2.88	255	69.8	2030.0	1787.1	1.14	0.86	1.34
	161.1	125.0	2.81	255	69.8	2040.0	1773.1	1.15	0.85	1.35
	167.9	137.1	5.10	347	69.8	2600.0	2581.1	1.01	0.88	1.15
	172.7	133.2	5.08	347	69.8	2700.0	2560.1	1.05	0.88	1.19
	194.8	121.0	4.72	347	69.8	2700.0	2435.7	1.11	0.94	1.19
	189.6	121.7	4.81	347	69.8	2680.0	2432.2	1.10	0.95	1.20
	162.7	100.7	2.97	255	52.5	1080.0	1248.8	0.86	0.89	1.02
	160.2	122.7	2.03	305	52.5	1400.0	1372.8	1.02	0.87	1.19
	160.1	119.4	2.01	305	52.5	1420.0	1333.2	1.07	0.87	1.24
	161.5	124.3	2.00	305	52.5	1320.0	1389.4	0.95	0.87	1.11
Tao and Yu[31]	60.0	60.0	1.87	282	81.0	382.0	405.3	0.94	1.17	1.21
	60.0	60.0	1.87	282	81.0	350.0	405.3	0.86	1.17	1.11
	100.0	100.0	1.87	282	81.0	860.0	910.4	0.94	1.07	1.12
	100.0	100.0	1.87	282	81.0	840.0	910.4	0.92	1.07	1.10
	150.0	150.0	1.87	282	81.0	1662.0	1806.1	0.92	1.02	1.04
	150.0	150.0	1.87	282	81.0	1740.0	1806.1	0.96	1.02	1.09
	200.0	200.0	1.87	282	81.0	2890.0	2995.3	0.96	0.99	1.06
	200.0	200.0	1.87	282	81.0	2920.0	2995.3	0.97	0.99	1.07
	250.0	250.0	1.87	282	60.0	3304.0	3089.2	1.07	0.87	1.19
	250.0	250.0	1.87	282	60.0	3400.0	3089.2	1.10	0.87	1.22
	60.0	60.0	2.00	404	50.9	318.0	330.8	0.96	1.00	1.12
	60.0	60.0	2.00	404	50.9	322.0	330.8	0.97	1.00	1.13
	100.0	100.0	2.00	404	50.9	770.0	665.1	1.16	0.91	1.30
	100.0	100.0	2.00	404	50.9	772.0	665.1	1.16	0.91	1.31
	150.0	150.0	2.00	404	50.9	1300.0	1210.8	1.07	0.86	1.18
	150.0	150.0	2.00	404	50.9	1420.0	1210.8	1.17	0.86	1.29
	200.0	200.0	2.00	404	50.9	1990.0	2127.1	0.94	0.93	1.13
	200.0	200.0	2.00	404	50.9	2054.0	2127.1	0.97	0.93	1.17
	250.0	250.0	2.00	404	50.9	3100.0	3014.1	1.03	0.89	1.21
	250.0	250.0	2.00	404	50.9	2965.0	3014.1	0.98	0.89	1.16
	60.0	60.0	2.00	404	81.0	422.0	439.9	0.96	1.10	1.11
	60.0	60.0	2.00	404	81.0	406.0	439.9	0.92	1.10	1.06
	150.0	150.0	2.00	404	81.0	2060.0	2064.1	1.00	1.06	1.17

	150.0	150.0	2.00	404	81.0	1980.0	2064.1	0.96	1.07	1.12
Yu et al.[32]	100.0	100.0	1.90	404	121	1220.0	1352.0	0.90	1.06	1.07
	100.0	100.0	1.90	404	121	1209.0	1352.0	0.89	1.06	1.06
Tao et al.[33]	249.9	250.2	2.50	234	50.1	3700.0	3588.8	1.03	0.83	1.18
	248.0	251.0	2.50	234	50.1	3530.0	3580.3	0.99	0.83	1.13
	248.7	252.3	2.50	234	50.1	3500.0	3564.4	0.98	0.82	1.11
	248.6	252.6	2.50	234	50.1	3620.0	3601.9	1.01	0.83	1.15
	190.1	190.2	2.50	234	54.8	2250.0	2391.4	0.94	0.85	1.10
	189.1	190.3	2.50	234	54.8	2240.0	2385.6	0.94	0.85	1.10
	189.5	190.9	2.50	234	54.8	2195.0	2369.0	0.93	0.84	1.07
	129.7	130.5	2.50	234	54.8	1310.0	1286.1	1.02	0.92	1.27
	129.6	130.5	2.50	234	54.8	1300.0	1288.3	1.01	0.92	1.26
	129.7	130.2	2.50	234	54.8	1300.0	1272.1	1.02	0.91	1.26
	129.7	130.5	2.50	234	54.8	1270.0	1286.1	0.99	0.92	1.23
	128.2	129.1	2.50	234	54.8	1150.0	1217.0	0.94	0.89	1.14
	249.0	126.0	2.50	234	50.1	2010.0	1830.2	1.10	0.79	1.19
	129.6	65.8	2.50	234	54.8	695.0	677.5	1.03	0.88	1.20
Wang and Li [34]	553.0	180.0	1.49	222	37.2	1788.0	2103.2	0.85	0.61	0.50
	553.0	180.0	1.49	222	15.6	1082.5	1070.5	1.01	0.63	0.61
	463.0	150.0	1.45	222	37.2	1300.0	1502.0	0.87	0.61	0.51
	463.0	150.0	1.45	222	15.6	943.0	782.6	1.20	0.63	0.73
	418.0	135.0	1.44	222	37.2	1216.0	1240.6	0.98	0.61	0.58
	418.0	135.0	1.44	222	18.3	779.8	729.7	1.07	0.63	0.65
	372.0	120.0	1.49	222	37.2	916.0	1011.3	0.91	0.62	0.54
	372.0	120.0	1.49	222	18.3	536.0	607.2	0.88	0.63	0.54
He and Liu [35]	298.0	100.0	0.92	229	14.1	398.0	419.7	0.95	0.63	0.77
	299.0	100.0	0.92	229	14.1	377.0	420.4	0.90	0.63	0.73
	296.0	100.0	0.92	229	17.7	429.0	495.7	0.87	0.63	0.71
	302.0	100.0	0.92	229	17.7	434.0	500.6	0.87	0.62	0.71
	358.0	120.0	0.89	229	14.1	483.0	572.4	0.84	0.63	0.69
	357.0	120.0	0.89	229	17.7	533.0	683.3	0.78	0.62	0.65
	358.0	150.0	1.45	223	14.1	877.0	854.3	1.03	0.70	0.92
	446.0	150.0	1.45	223	14.1	893.0	949.5	0.94	0.64	0.77
	453.0	150.0	1.45	223	17.7	958.0	1132.3	0.85	0.63	0.69
	447.0	150.0	1.45	223	17.7	976.0	1125.1	0.87	0.63	0.71
Zhang and Chen [36]	200.0	200.0	1.25	373	29.7	1590.0	1561.5	1.02	0.86	1.17
	200.0	200.0	1.25	373	29.7	1826.0	1748.0	1.04	0.97	1.34
	200.0	200.0	1.25	373	29.7	2002.0	1934.5	1.03	1.07	1.47
	300.0	300.0	1.25	373	32.9	4195.0	3324.7	1.26	0.80	1.38
	300.0	300.0	1.25	373	32.9	4240.0	3511.2	1.21	0.85	1.40
	300.0	300.0	1.25	373	32.9	4140.0	3697.7	1.12	0.89	1.36
Lv et al.[37]	200.0	200.0	5.00	227	24.7	2061.0	1893.4	1.09	0.93	1.24
	200.0	200.0	5.00	227	28.3	2530.0	2334.4	1.08	1.06	1.42
	200.0	200.0	5.00	227	32.5	2468.0	2474.4	1.00	1.03	1.30
	300.0	300.0	5.00	227	24.7	3621.0	3457.6	1.05	0.88	1.16
	300.0	300.0	5.00	227	28.3	4603.0	4209.2	1.09	0.97	1.36
	300.0	300.0	5.00	227	32.5	4872.0	4524.2	1.08	0.95	1.32
	100.0	100.0	2.29	198	32.6	507.0	549.5	0.92	0.98	1.17

	100.0	100.0	2.29	198	32.6	508.0	549.5	0.92	0.98	1.17
	100.0	100.0	2.20	346	21.8	521.0	540.5	0.96	0.97	1.10
	100.0	100.0	2.20	346	21.8	520.0	540.5	0.96	0.97	1.10
	100.0	100.0	2.99	294	21.0	539.0	589.4	0.91	1.01	1.06
	100.0	100.0	2.99	294	21.0	538.0	589.4	0.91	1.01	1.06
	100.0	100.0	4.25	290	20.2	680.0	702.1	0.97	0.99	1.07
	100.0	100.0	4.25	290	20.2	679.0	702.1	0.97	0.99	1.07
Zhang [38]	120.0	120.0	3.50	330	27.3	882.0	981.0	0.90	0.98	1.04
	120.0	120.0	3.50	330	31.2	882.0	1027.8	0.86	0.97	0.99
	120.0	120.0	3.50	330	31.2	921.0	1027.8	0.90	0.97	1.03
	120.0	120.0	3.50	330	49.3	1080.0	1245.0	0.87	0.91	0.99
	140.0	140.0	3.50	330	16.0	941.0	989.6	0.95	0.98	1.06
	140.0	140.0	3.50	330	16.7	922.0	1008.6	0.91	0.99	1.03
	140.0	140.0	3.50	330	54.6	1499.0	1654.1	0.91	0.87	1.02
	140.0	140.0	3.50	330	54.6	1470.0	1654.1	0.89	0.87	1.00
Fan [39]	199.9	199.9	5.78	365	32.1	3193.0	3055.9	1.04	0.97	1.20
	200.1	200.1	5.78	365	44.1	3551.0	3461.5	1.03	0.93	1.18
	200.0	200.0	5.78	365	44.1	3593.0	3459.0	1.04	0.93	1.19
	250.1	250.1	5.78	375	32.1	4376.0	4228.7	1.03	0.94	1.18
	250.1	250.1	5.78	375	44.1	4824.0	4854.2	0.99	0.90	1.12
	250.2	250.2	5.78	375	44.1	4851.0	4857.0	1.00	0.90	1.13
	250.1	250.1	5.78	377	32.1	3747.0	4242.3	0.88	0.94	1.00
	250.1	250.1	5.78	377	44.1	4870.0	4867.8	1.00	0.90	1.13
	250.1	250.1	5.78	377	44.1	4467.0	4867.8	0.92	0.90	1.04
Xu [40]	120.0	120.0	5.60	321	30.0	1176.0	1339.1	0.88	1.03	1.01
	120.0	120.0	5.60	321	30.0	1117.0	1339.1	0.83	1.03	0.96
	120.0	120.0	5.60	321	25.8	1195.0	1254.5	0.95	1.01	1.06
	120.0	120.0	5.60	321	52.5	1460.0	1646.9	0.89	0.99	1.05
	120.0	120.0	5.60	321	52.5	1372.0	1646.9	0.83	0.99	0.99
	140.0	140.0	5.60	321	16.3	1342.0	1296.5	1.04	0.96	1.09
	140.0	140.0	5.60	321	16.2	1292.0	1293.6	1.00	0.96	1.05
	140.0	140.0	5.60	321	54.6	2009.0	2078.2	0.97	0.95	1.13
	140.0	140.0	5.60	321	54.6	1906.0	2078.2	0.92	0.95	1.07
	200.0	200.0	5.60	321	17.6	2058.0	2281.5	0.90	1.02	1.04
	200.0	200.0	5.60	321	17.6	1960.0	2281.5	0.86	1.02	0.99
Tao and Han[41]	250.0	250.0	4.60	377	29.7	2796.0	3078.6	0.91	0.96	1.03
	151.0	151.0	2.00	217	32.8	800.0	726.5	1.10	0.86	1.20
	148.0	148.0	2.00	217	24.7	600.0	604.9	0.99	0.90	1.09
	250.0	250.0	5.80	375	29.7	3289.0	3599.7	0.91	0.99	1.05
	199.9	199.9	5.80	365	29.2	2471.0	2646.4	0.93	1.02	1.08
	76.2	76.2	3.38	324	40.9	522.0	526.0	0.99	1.06	1.17
	199.9	199.9	5.80	365	37.8	3193.0	2838.3	1.12	1.00	1.30
	151.0	151.0	6.92	246	24.7	1640.0	1526.2	1.07	1.07	1.27
	250.0	250.0	5.80	375	51.9	4824.0	4374.4	1.10	0.93	1.25
	76.2	76.2	3.38	324	40.9	516.0	526.0	0.98	1.06	1.16
	250.0	250.0	5.80	375	51.9	4851.0	4374.4	1.11	0.93	1.26
	250.0	250.0	4.60	376	37.8	3747.0	3357.4	1.12	0.93	1.26
	149.0	149.0	4.30	246	38.7	1405.0	1222.7	1.15	0.96	1.32

	127.0	127.0	4.30	485	44.9	1634.0	1652.9	0.99	1.03	1.15
	151.0	151.0	6.90	292	24.7	1735.0	1748.6	0.99	1.08	1.17
	114.0	114.0	4.39	254	32.1	915.0	832.2	1.10	1.09	1.29
	149.0	149.0	4.30	246	38.7	1425.0	1222.7	1.17	0.99	1.34
	250.0	250.0	5.80	375	37.8	4376.0	3882.3	1.13	0.97	1.29
Wang and Shang [42]	125.0	125.0	3.20	299	28.8	865.0	938.8	0.92	0.95	1.05
	125.0	125.0	4.50	296	28.8	1164.0	1159.9	1.00	1.00	1.17
	125.0	125.0	6.00	285	28.8	1444.0	1382.6	1.04	1.05	1.24
	125.0	125.0	3.20	299	38.3	1115.0	1062.5	1.05	0.91	1.19
	125.0	125.0	4.50	296	38.3	1312.0	1283.6	1.02	0.96	1.19
	125.0	125.0	6.00	285	38.3	1512.0	1506.3	1.00	1.01	1.19
He et al.[43]	273.0	273.0	3.00	380	42.8	3675.0	4565.4	0.80	0.90	0.96
	273.0	273.0	3.00	380	42.8	3689.0	4565.4	0.81	0.90	0.96
	203.0	203.0	3.00	380	42.8	3408.0	2888.0	1.18	0.95	1.46
	203.0	203.0	3.00	380	42.8	3361.0	2888.0	1.16	0.95	1.44
	233.0	233.0	3.00	318	42.8	2640.0	3298.5	0.80	0.90	0.96
	233.0	233.0	3.00	318	42.8	2603.0	3298.5	0.79	0.90	0.94
	203.0	203.0	3.00	318	42.8	2190.0	2656.6	0.82	0.93	1.00
	203.0	203.0	3.00	318	42.8	2240.0	2656.6	0.84	0.93	1.02
	183.0	183.0	3.00	380	42.8	2010.0	2177.9	0.92	0.86	1.02
	183.0	183.0	3.00	380	42.8	2070.0	2177.9	0.95	0.86	1.05
	153.0	153.0	3.00	380	42.8	1580.0	1657.1	0.95	0.88	1.06
	153.0	153.0	3.00	380	42.8	1490.0	1657.1	0.90	0.88	1.00
	153.0	153.0	4.50	340	42.8	1920.0	1938.4	0.99	0.93	1.14
	203.0	203.0	3.00	318	53.6	2405.0	3027.5	0.79	0.89	0.95
	153.0	153.0	3.00	380	53.6	1710.0	1867.8	0.92	0.85	1.02
	153.0	153.0	3.00	380	53.6	1680.0	1867.8	0.90	0.85	1.00
	153.0	153.0	3.00	318	53.6	1580.0	1940.1	0.81	0.94	1.01
	150.0	150.0	4.50	340	53.6	2010.0	2086.9	0.96	0.90	1.10
	203.0	203.0	3.00	318	25.7	2090.0	1795.5	1.16	0.89	1.29
	153.0	153.0	3.00	318	25.7	1470.0	1189.4	1.24	0.93	1.39
	150.0	150.0	4.50	340	25.7	1820.0	1563.7	1.16	1.00	1.35
Kenji et al.[44]	178.0	178.0	9.00	283	36.7	2671.0	3106.2	0.86	1.03	1.02
	179.0	179.0	5.50	248	36.6	2034.0	2128.2	0.96	0.92	1.10
	174.0	174.0	3.00	266	34.6	1642.0	1723.9	0.95	0.97	1.19
Han [45]	159.8	159.8	6.30	483	53.4	2350.0	3426.2	0.69	1.01	0.80
	115.9	115.9	4.90	309	53.4	1174.0	1425.0	0.82	0.95	0.97
	141.8	141.8	4.30	433	53.4	1618.0	2139.4	0.76	0.93	0.87
	141.8	141.8	3.90	357	53.4	1150.0	1825.5	0.63	0.90	0.72
	165.7	165.7	5.10	373	53.4	2309.0	2707.7	0.85	0.92	0.98
	133.1	133.1	4.50	324	53.4	1145.0	1703.2	0.67	0.92	0.78
	111.3	111.3	2.00	354	53.4	894.0	1034.2	0.86	0.94	1.07
	130.6	130.6	2.30	243	53.4	1250.0	1206.3	1.04	0.88	1.23
Tan et al.[46]	125.0	125.0	1.00	232	84.7	1275.0	1280.6	1.00	0.75	1.06
	125.0	125.0	1.00	232	84.7	1239.0	1280.6	0.97	0.75	1.03
	127.0	127.0	2.00	258	84.7	1491.0	1540.0	0.97	0.81	1.10
	127.0	127.0	2.00	258	84.7	1339.0	1540.0	0.87	0.81	0.99
	133.0	133.0	3.50	352	84.7	1995.0	2252.7	0.89	0.93	1.11

	133.0	133.0	3.50	352	84.7	1991.0	2252.7	0.88	0.93	1.11
	133.0	133.0	3.50	352	84.7	1962.0	2252.7	0.87	0.93	1.09
	133.0	133.0	4.70	352	84.7	2273.0	2285.8	0.99	0.88	1.15
	133.0	133.0	4.70	352	84.7	2158.0	2285.8	0.94	0.88	1.09
	133.0	133.0	4.70	352	84.7	2253.0	2285.8	0.99	0.88	1.14
	127.0	127.0	7.00	429	84.7	3404.0	2936.3	1.16	1.04	1.39
	127.0	127.0	7.00	429	84.7	3370.0	2936.3	1.15	1.04	1.38
	127.0	127.0	7.00	429	84.7	3364.0	2936.3	1.15	1.04	1.38
Liu et al.[47]	142.0	142.0	3.00	255	60.0	1952.0	1673.9	1.17	0.90	1.42
	141.8	141.8	3.00	255	60.0	1834.0	1670.1	1.10	0.90	1.33
	143.4	143.4	3.00	255	60.0	2010.0	1700.5	1.18	0.90	1.43
	143.0	143.0	3.00	255	70.0	2030.0	1863.3	1.09	0.87	1.31
	141.6	141.6	3.00	255	70.0	1773.0	1833.5	0.97	0.87	1.16
	140.9	140.9	3.00	255	70.0	1754.0	1818.6	0.96	0.88	1.16
	142.3	142.3	2.00	305	60.0	1762.0	1544.4	1.14	0.86	1.33
	139.7	139.7	2.00	305	60.0	1868.0	1498.0	1.25	0.86	1.46
	142.5	142.5	2.00	305	60.0	1909.0	1548.0	1.23	0.86	1.44
	140.7	140.7	2.00	305	70.0	1914.0	1680.8	1.14	0.84	1.32
	142.1	142.1	2.00	305	70.0	1932.0	1709.1	1.13	0.84	1.30
	142.6	142.6	2.00	305	70.0	2030.0	1719.3	1.18	0.84	1.36

4.   CONCLUSIONS

According to the analysis of this paper, we can obtain the following conclusions:

The calculating precision of existing calculation models of bearing capacity are not high, the calculating results appears the bigger error among different countries specifications. Moreover, the cross-sectional aspect ratios, the effects of the thickness of thin-walled steel tube, the longitudinal stiffened rib and the concrete strength on the bearing capacity are not reflected in existing models, the calculating precision needs to be further enhanced.

Due to the confinement of rectangular steel tube to core concrete, the bearing capacity and ductility can be increased, but the increasing effect of rectangular CFT column is not as good as its circular counterpart. This is mainly because the confinement of rectangular steel tube to concrete may be divided into the effective and non-effective confining zone, so this paper firstly presents a calculating method for the coefficient of the effective confining area of rectangular CFT columns.

Based on the proposed coefficient of the effective confining area, considering the effect of the cross-sectional aspect ratios, the concrete strength, the thickness of thin-walled steel tube, the longitudinal stiffened rib on the bearing capacity, a calculating model for the bearing capacity of rectangular CFT columns are proposed, the model can be used to calculate the bearing capacity of common concrete filled steel tubular column, high strength concrete filled steel tubular column, concrete filled thin-walled steel tubular column and stiffened concrete filled steel tubular column.

The characteristic of rectangular CFT columns are reflected in the proposed model, the effects of the effective confining zone and other factors on the bearing capacity are well considered. The proposed model is not only simple, but agrees well with large experimental data.

ACKNOWLEDGEMENTS

REFERENCES

[1]   ACI Committee 318, "Building Code Requirement for Structural Concrete and Commentary", American Concrete Institute, Detroit, USA, 2005.
[2]   China Engineering Construction Standardization Institute Standard, "Design and Construction Rules of Concrete Filled Steel Tube Structure (CECS28:90)", China Planning Press, Beijing, 1990.
[3]   European Committee for Standardization, "Design of Composite Steel and Concrete Structures-Part1.1: General Rules and Rules for Buildings", Eurocode, 2004.
[4]   China Power Industry Standard, "Design Rules of Steel-concrete Composite Structure (DL/T5085-1999)", China Power Press, Beijing, 1999.
[5]   Han, L.H., "Concrete Filled Steel Tube Structure-theory and Practice". Science Press, Beijing, 2007.
[6]   Zhong, S.T., "Concrete Filled Steel Tube Structure", Tsinghua University Press, Beijing, 2002.
[7]   ASCCS, "Concrete Filled Steel Tubes-A Comparison of International Codes and Practices", ASCCS, Seminar, Innsbruck, Austria, 1997.
[8]   AIJ, "Recommendations for Design and Construction of Concrete Filled Steel Tubular Structures", Architecture Institute of Japan, Tokyo, Japan, 1997.
[9]   China Building Materials and Industry Bureau Standard, "Design and Construction Rules of Concrete Filled Steel Tube Structure (JCJ 01-89)", Tongji University Press, Shanghai, 1989.
[10]   China Engineering Construction Standardization Institute Standard, "Technical Rules of Rectangular Concrete Filled Steel Tube Structure (CECS159-2004)", China planning Press, Beijing, 2004.
[11]   China Military Standard, "Technical Specifications for Early-strength Model Composite Structure Used for Navy Port Emergency Repair in Wartime (GBJ 4142-2000)", Chinese pla General Logistics, Beijing, 2000.
[12]   Fujian Engineering Construction Standard, "Technical Rules of Concrete Filled Steel Tube Structure (DBJ13-51-2003)", 2003.
[13]   Furlon R.W., "Strength of Steel-Encased Concrete Beam Columns", Journal of the Structural Division, 1967, Vol. 93, No. 5, pp. 113-124.
[14]   Yu, F. and Niu, D.T., "Analysis on Bearing Capacity of FRP-confined Concrete Filled Steel Tubes", Journal of Harbin Institute of Technology, 2007, Vol. 39, No. 2, pp. 44-46.
[15]   Uy. B., "Strength of Short Concrete Filled High Strength Steel Box Columns", Journal of Constructional Steel Research, 2001, Vol. 57, No. 2, pp. 113-134.
[16]   Cai, S.H., "Modern Concrete Filled Steel Tube Structures", China Communication Press, Beijing, 2003.
[17]   AISC, Load and Resistance Factor Design (LRFD), "Specification for Structural Steel Buildings", American Institute of Steel Construction, Inc., Chicago, 1994.
[18]   Yu, Y., "Study on Behavior of Concrete-filled Rectangular Tubular Columns", Doctor Dissertation of Tongji University, 2002.
[19]   Shakir Khalil, H. and Zeghiche, J., "Experimental Behavior of Concrete Filled Rolled Rectangular Hollow-Section Columns", Structural Engineer, 1989, Vol. 67, No. 19, pp. 346-353.

[20]   Shakir Khalil, H. and Mouli, M., "Further Tests on Concrete-Filled Rectangular Hollow-Section Columns", Structural Engineer, 1990, Vol. 68, No. 20, pp. 405-413.

[21]   Schneider, S.P., "Axially Loaded Concrete-Filled Steel Tubes", Journal of Structural Engineering, 1998, Vol. 124, No. 10, pp. 1125-1138.

[22]   Jiang, T., Shen, Z.O. and Yu,, Z.W., "Calculation of Load Capacity of Concrete Filled Rectangular Steel Tube under Axial Load", Special Structures, 2002, Vol. 19, No. 2, pp. 4-6.

[23]   Wang, L. and Jiang, X., "Calculation of Load Capacities for Short Concrete- Filled Steed Tube Columns with Rectangular Section", Journal of Guilin Institute of Technology, 2003, Vol. 23, No. 4, pp. 441-444.

[24]   Han, L.H. and Yang, Y.F., "Study on Axial Bearing Capacity of Concrete-filled Steel Tube Columns with Rectangular Section", China Civil Engineering Journal, 2001, Vol. 34, No. 4, pp. 21-31.

[25]   Han, L.H. and Yang, Y.F., "Study on Behavior of Concrete Filled Square Steel Tubes under Axial Load", China Civil Engineering Journal, 2001, Vol. 34, No. 2, pp. 17-25.

[26]   Tomii, M. and Sakino, K., "Experimental Studies on the Ultimate Moment of Concrete Filled Square Steel Tubular Beam-Columns", Journal of Structural and Construction Engineering, 1979, No. 275, pp. 55-63.

[27]   Tomii, M. and Sakino, K., "Experimental Studies of Concrete Filled Steel Tubular Columns under Concentric Loading", In: Proceedings of the International Colloquium on Stability of Structures under Static and Dynamic Loads, SSRC/ASCE/Washington, D.C./March, 1977, pp. 17-19.

[28]   Sakiuo, K., "Behaviors of Concrete Filled Steel Tubular Columns under Concentric Loadings", The Third International Conference on Steel-Concrete Composite Structures, Fukuoka, 1991, pp. 295-309.

[29]   Zhang, S.M., Guo, L.H., Ye, Z. and Wang, Y.Y., "Experimental Research on High Strength Concrete Filled SHS Stub Columns Subjected to Axial Compressive Load", Journal of Harbin Institute of Technology, 2004, Vol. 36, No. 12, pp. 1610-1614.

[30]   Ye, Z.L, "Study on Behavior of High-strength Concrete Filled Square and Rectangular Steel Tubes", Master Dissertation of Harbin Institute of Technology, 2001.

[31]   Tao, Z. and Yu, Q., "Experiment, Theory and Method of New Hybrid Structural Columns", Beijing, Science Press, 2006.

[32]   Yu, Q. and Tao, Z. and Wu, Y.X., "Experimental Behavior of High Performance Concrete-filled Steel Tubular Columns", Thin-Walled Structures, 2008, No. 46, pp. 362-370.

[33]   Tao, Z., Han, L.H. and Wang, Z.B., "Experimental Behavior of Stiffened Concrete-filled Thin-walled Hollow Steel Structural (HSS) Stub Columns", Journal of Constructional Steel Research, 2005, No. 61, pp. 962-983.

[34]   Wang, Q.P. and Li, H.W., "Experimental Study on the Concrete Filled Square Thin-walled Steel Tubes Subjected to Axial Compression", Low Temperature Architecture Technology, 2005, No. 3, pp. 51-52.

[35]   He, M.S. and Liu, X.Y., "Study on Behavior of Lightweight Aggregate Concrete Filled Square Thin-walled Steel Tubes under Axial Load", Sichuan Building Science, 2008, Vol. 34, No. 2, pp. 18-21.

[36]   Zhang, Y.C. and Chen, Y., "Experimental Study and Finite Element Analysis of Square Stub Columns with Straight Ribs of Concrete-filled Thin-walled Steel Tube", Journal of Building Structures, 2006, Vol. 27, No. 5, pp. 16-22.

[37]   Lv, X.L., Yu, Y. and Chen, Y.Y., "Behavior of Axially Loaded Concrete-filled Rectangular Tubular Columns", Experiment, Building Structures, 1999, No. 10, pp. 41-43.

[38]   Zhang, Z.G., "Mechanism and Capacity Analysis of Concrete Filled Square Steel Tubular Columns", Industrial Construction, 1989, No. 11, pp. 2-7.

[39]   Fan, Z., "Analysis of Ultimate Axial Loads of Concrete-filled Steel Columns with Rectangular Section", Engineering Mechanics, 1994, Vol. 11, No. 3, pp. 80-86.

[40]   Xu, M., "Study on Experiment, Theory and Application of the Confined Steel Reinforced Concrete Columns", Doctoral Dissertation of Southeast University, 2000.

[41]   Tao, Z. and Han, L.H., "Design of Concrete Filled Square Steel Tubular Members", Journal of Harbin University of Civil Engineering and Architecture, 2001, Vol. 34, No. 3, pp. 16-22.

[42]   Wang, H.J. and Shang, Z.Q., "Experimental Research on the Behavior of Square Concrete Filled Steel Tubes under Axial Compression", Journal of Shenyang University of Technology, 2005, Vol. 27, No. 1, pp. 98-102.

[43]   He, F., Zhou, X.H. and Tang, C.H., "Experimental Research on the Bearing Behavior of High-strength-concrete-filled Steel Tube under Axial Compression", Engineering Mechanics, 2000, Vol. 17, No.4, pp. 61-66.

[44]   Kenji, S., Hiroyuki, N. and Shosuke, M., "Behavior of Centrally Loaded Concrete Filled Steel Tube Short Columns", Journal of Structural Engineering, 2004, Vol. 130, No. 2, pp. 180-188.

[45]   Han, L.H., "Theoretical Analysis and Experimental Researches for the Behaviors of High Strength Concrete Filled Steel Tubes Subjected to Axial Compression", Industrial Construction, 1997, Vol. 27, No. 11, pp. 39-44.

[46]   Tan, K.F., Pu, X.C. and Cai, S.H., "Study on the Mechanical Properties of Steel Extra-high Strength Concrete Encased in Steel Tubes", Journal of Building Structure, 1999, Vol. 20, No. 1, pp.10-16.

[47]   Liu, J.P., Zhang, S.M. and Guo, L.H., "Axial Compression of Behavior Square Tube Confined High Strength Concrete (HSC) Short Columns", Journal of Harbin Institute of Technology, 2008, Vol. 40, No. 10, pp. 1542-1545.